

MEASURING PROXIMITY INDUCED EFFECTS IN TOPOLOGICAL
INSULATORS USING SCANNING PROBE MICROSCOPY TECHNIQUES

By

Ian Matthew Dayton

A DISSERTATION

Submitted to
Michigan State University
in partial fulfillment of the requirements
for the degree of

Physics — Doctor of Philosophy

2016

ABSTRACT

MEASURING PROXIMITY INDUCED EFFECTS IN TOPOLOGICAL INSULATORS USING SCANNING PROBE MICROSCOPY TECHNIQUES

By

Ian Matthew Dayton

Scanning probe methods such as scanning tunneling microscopy (STM) and subsurface charge accumulation imaging (SCAI) are very powerful and important tools to investigate the electronic effects near the interfaces of exotic materials. For this dissertation, the primary material studied is a three-dimensional topological insulator, which has been discovered in recent years to harbor a great deal of novel physical phenomenon. The primary feature of note with these materials is their intrinsic spin-orbit coupling, which gives rise to the surface states where the spin and momentum of the conducting electrons are locked in surprising ways to one another. Specifically, the dispersion diagram shows two branches with linear energy versus wave number crossing the semiconductor gap to form a Dirac cone feature; these conducting states reside on the surface and are known as topological surface states (TSS). This state is topologically protected by time-reversal symmetry in that these conducting surface states are robust against scattering from non-magnetic defects.

In this dissertation, I will present STM results for superconductor/topological insulator interfaces, in which the superconductor induces superconductivity into the topological surface states. Superconductivity is caused by the pairing of electrons into bosons which are known as Cooper pairs, and is yet another phenomenon that involves rather intricate spin and momentum interactions. In these measurements, we observed oscillatory behavior near the interfaces as well as a surprising reverse proximity effect, in which the topological surface states appear to leak into the superconducting material as well. In the Appendix, I will also

present STM and SCAI results taken at conventional insulator/topological insulator interfaces, where the TSS is predicted to change locations based on the conventional insulator material deposited on the surface in an effect known as the “dual” proximity effect. In particular, we investigate the interface of ZnSe and Bi₂Te₃. While there has been no theoretical prediction for this specific interface, our results show that the TSS remains at the interface and does not change location as a function of bias voltage. Even though these results are preliminary, they set the stage for interesting and important measurements in the future.

This dissertation is dedicated to my wife Christina Dayton and to my parents Timothy and Daryl Dayton. Without their endless love and support, none of this would have been possible.

ACKNOWLEDGMENTS

I would like to first thank my advisor Dr. Stuart Tessmer for his exceptional mentoring and teaching during my time in graduate school. Your kind and steady guidance was and is crucial to my success, and I have learned more than I could ever have imagined under your tutelage. I truly could not imagine a more perfect fit for an advisor and teacher, and I am very proud to have been given the opportunity to work for you.

Next I would like to thank Dr. Reza Loloee for all of his hard work and help that he has given me throughout the years. There is always a great deal to learn in this field, especially in terms of different experimental skillsets, and you taught me an incredible amount.

Of course, I also would like to thank Dr. Norman Birge, Dr. Alex Levchenko, Dr. Scott Pratt, and Dr. Joey Huston for their immeasurable help and support while serving on my graduate committee during my time at MSU.

Dr. Alex Levchenko and Dr. Nicholas Sedlmayr played a very significant role in the theoretical discussions and calculations that provided interpretation and detailed modeling of my data. I owe them a great deal of gratitude for their hard work and helpful discussions on the material presented in this dissertation.

During my time in graduate school, I made many friends who helped me along the way, not only with technical discussions, but also by bringing no small measure of levity to working in BPS. Dr. Eric Gingrich, Dr. Bill Martinez, Dr. Sean Wagner, Bethany Niedzielski, Victor Aguilar, Matthias Muenks, Connor Glosser, Sam Lipschutz, Matt Mondragon, Jared Doster, and Chris Willis; thank you so much for your friendship and help throughout the years. You made working here a much more enjoyable experience.

Thank you to Eric Goodwin, Victor Ramirez, and Michael Gottschalk for your compan-

ionship and help in the lab. I hope that I was able to teach you all something along the way and I look forward to hearing about the great things that you will accomplish in your lives.

I would like to thank my parents, Timothy and Daryl Dayton, for all of their love and support. At the end of the day, everything I have and will accomplish is because of you, and I truly have an immeasurable amount of gratitude for everything you have done for me.

Last but not least, I would like to thank my loving wife Christina Dayton. You seemingly appeared out of nowhere in the middle of my graduate studies and have made my already bright world more brilliant than it has ever been. We take this next step together, and I cannot wait to see what life has in store for us.

Thank you, one and all, for making this possible.

The work in this dissertation was completed with support from the Department of Education through GAANN Award No. USDE P200A140215 and from the Peter Schroeder Endowment.

TABLE OF CONTENTS

LIST OF TABLES	ix
LIST OF FIGURES	x
Chapter 1 Introduction	1
Chapter 2 Experimental Techniques	4
2.1 Scanning Tunneling Microscopy	4
2.1.1 Tunneling Theory	4
2.1.2 Scanning Tunneling Spectroscopy	6
2.1.3 Experimental Setup	9
2.1.3.1 Besocke Design STM	9
2.1.3.2 Cryogenic STM System	10
2.2 Scanning Charge Accumulation Imaging	12
2.3 Tip Preparation	19
Chapter 3 The Theories of Topological Insulators and Superconductivity 22	22
3.1 Topological Insulators	22
3.1.1 Quantum Hall Effect and Quantum Spin Hall Effect	24
3.1.2 3D Topological Insulators and Bi_2Se_3	27
3.2 Superconductivity	31
3.2.1 BCS Theory	32
3.2.2 P-Wave Superconductors	37
3.2.3 Superconducting Proximity Effect	39
Chapter 4 Probing Superconductor/TI Interfaces	43
4.1 Superconducting Proximity Effect of PbBi on Bi_2Se_3	43
4.1.1 Motivation	43
4.1.2 Introduction	46
4.1.3 Experiment	49
4.1.4 Theory and Calculations	58
4.1.5 Conclusions	60
4.2 Superconducting Proximity Effect of Pure Nb on Bi_2Se_3	62
4.2.1 Introduction	62
4.2.2 Results	63
4.2.3 Conclusion	74
Chapter 5 Conclusions	77
5.1 Summary of Results	77
5.2 Future Goals	77

APPENDICES	80
Appendix A Superconducting Proximity Effect of Pb on Bi ₂ Se ₃	81
Appendix B Topological Insulator/Conventional Insulator “Dual” Proximity Effect	85
Appendix C Kelvin Probe	98
 BIBLIOGRAPHY	 102

LIST OF TABLES

Table 4.0a:	Table presenting the calculated values of Δ and other fitting parameters for the best fit DOS curves at various distances from the superconducting island. The algorithm utilized both thermal and energetic smearing. Here Γ is the characteristic energy smearing of the material and L is the related mean free path, and the two values are related by the equation $L = \hbar v_f / 2\Gamma$. All calculations were done using a temperature of 4.2 K. The p-wave calculations were done via a sum of separate s-wave superconducting curves weighed accordingly by a p-wave orbital function.	55
Table 4.0b:	A comparison of the gap widths taken from the best fit DOS curves with the widths extracted using our linear-subtraction method.	55
Table B.1:	Table summarizing the results of the Wu et. al. paper and labeling the characteristic properties of the materials used in the calculations. V_g is the band gap width, Φ is the work function, a is the bulk lattice constant, Δa is the lattice mismatch, E_b is the binding energy between the CI and TI layers, and Z is the location of the TSS for the specific geometry calculated.[2]	88

LIST OF FIGURES

Figure 2.1:	Vacuum barrier between a tip and sample, with the electron wave function shown in red. This demonstrates that a propagating electron has the ability to tunnel from the sample to the tip when a voltage is applied between them. Here, eV is the contribution from the bias voltage. . . .	5
Figure 2.2:	By sweeping the bias voltage, we are able to fill (empty) the empty (occupied) states of the sample. As the tunneling current depends on the number of accessible states, this allows us to extract its LDOS.	7
Figure 2.3:	(a) Schematic showing the layout of a Besocke design STM. (b) Actual house-built STM in the Tessmer lab.	9
Figure 2.4:	The full measurement setup with STM dipper fully submerged in the blue liquid Helium dewar.	11
Figure 2.5:	Diagram of cryostat used in our lab, showing all of the important chambers and features. Here, the sorption pump (Sorb) is in the shape of a torus and is found inside of the vacuum chamber, which allows the STM to pass through it and reach the bottom.	13
Figure 2.6:	A highly simplified diagram demonstrating the relationship of geometric capacitance C_G on the distance between the tip and the sample.	15
Figure 2.7:	(a) Circuit diagram of our SCAI measurement chip. The HEMT acts as a highly sensitive charge detector that is directly connected to the scanning probe tip, which allows us to see charge fluctuations in the sample due to image charges formed in the tip. (b) Simplified diagram demonstrating the existence of a voltage divider for the AC excitation voltage going through two capacitors.	16
Figure 2.8:	The left image shows a fully assembled SCAI measurement chip complete with protection loops. The method of assembly utilizes fine tweezer work with conductive epoxy to fasten the primary circuit elements and connection wires to the GaAs chip. In order to connect the gold pads to the correct elements, we utilize a gold wire bonder. The right image shows a HEMT with no connections. The HEMT as a whole is approximately $600 \mu\text{m}$ wide and the gate pad itself is only $80 \mu\text{m}$ wide.	18

Figure 2.9:	SEM images demonstrating the tip geometry after the rough etching step. The bulb at the end will ideally drop off due to gravity assistance during the fine etching process. (a) Initial scan where the bulb is clearly visible and (b) Closer look at the same tip.	20
Figure 2.10:	SEM images demonstrating what happens to an STM tip when it is dropped. What was once an ideal candidate for use as a scanning probe is now rendered unusable due to the large radius of curvature at the bend in the wire. (a) Initial scan where the bend is clearly visible. (b) Closer look at the same tip.	20
Figure 2.11:	SEM images showing the profile of a single cut tip. (a) While the cut tip looks to have multiple points, there is one clear point that is more than $50 \mu m$ further out from the others. (b) Close up of the apex showing that the radius of curvature is less than 40 nm	21
Figure 3.1:	A diagram of the quantum Hall system with integer Landau levels filling in the interior in the classical picture (a) and the resulting quantum behavior (b). The edge of the two-dimensional system conducts while the center remains insulating due to the localized states of the electrons. Figure adapted from [6].	25
Figure 3.2:	This diagram demonstrates the two spin polarized conducting states on the edge of the two-dimensional system, where the red line can be considered to be spin-up electrons and the blue can be considered to be spin-down electrons. Figure adapted from [6].	26
Figure 3.3:	The Dirac cone is a consequence of the spin-orbit coupling from in TI's. The red and blue crossing channels correspond to the spin-up and spin-down channels respectively. The crossing point in the center is known as the Dirac point, and is typically not found at the Fermi level E_F of the material. Figure adapted from [6].	27
Figure 3.4:	(a) Schematic of the structure for Bi_2Se_3 . Bi_2Se_3 is a layered material consisting of stacked quintuple layers made from 3 Se atoms and 2 Bi atoms. The layers are attracted to one another through van der Waals forces and are therefore easy to separate by exfoliation. (b) Schematic showing the p-orbital splitting of Bi and Se near the Fermi level, which is denoted by the dotted blue line. Region (I) takes the chemical bonding of Bi and Se into account, while region (II) further demonstrates the effects on the energy levels from the crystal field. Finally, region (III) shows the effect of strong spin orbit coupling, in which band inversion occurs and the topological phase is created. (a) is adapted from Romanowich et. al. and (b) is adapted from Qi and Zhang. [18, 17]	30

Figure 3.5:	(a) Diagram of the Dirac cone with spin polarized conical sections in k -space. At energies above the crossing point of the Dirac cone, the electrons will be polarized in one direction when traveling around the cone, whereas at energies below the point, electrons will be polarized in the opposite direction. (b) Basic calculation demonstrating the expected behavior of the Dirac cone when looking at the density of states. To calculate the expected DOS curve, we need to integrate over the Fermi surface in two-dimensions. The resulting integral gives a linear dispersion relation in k , which yields a linear DOS versus energy curve. This is what we theoretically expect to see when taking scanning tunneling spectroscopy over a bare TI.	31
Figure 3.6:	As the first electron moves to the right, it causes a distortion in the lattice, creating a region with higher positive charge. This region attracts a second electron into the newly formed potential well, and the two electrons become a pair known as a Cooper pair.	34
Figure 3.7:	A calculated superconducting energy gap demonstrating what the expected density of states would look like on a BCS superconductor. The width of the gap is $2\Delta_0$. A small amount of thermal broadening was applied in the calculation to prevent the coherence peaks from going to infinity.	36
Figure 3.8:	(a) A plot of the superconducting pairing potential $\Delta(\mathbf{k})$ for a p-wave pairing symmetry in the $k_x - k_y$ plane. (b) The density of states of a pure p-wave superconductor. The DOS is not fully gapped like in the s-wave case, which results in a “v” shape inside of the superconducting gap.	39
Figure 3.9:	An image demonstrating the behavior of $\Delta(\mathbf{r})$ as a function of the pair correlation amplitude $F(\mathbf{r})$ and the interaction parameter $g(\mathbf{r})$	42
Figure 4.1:	Proposed anti-dot geometry where a continuous superconducting film is deposited on the surface of a TI with anti-dots spaced evenly throughout the film, which would go all the way to the TI surface. By applying a magnetic field normal to the S/TI surface, Majorana bound states are theoretically predicted to form around the boundary of the anti-dot, which could be probed using STS. Figure adapted from the Hasan and Kane colloquium on topological insulators. [16]	44
Figure 4.2:	LDOS taken 40 nm from a superconducting island at 4.2 K with s-wave and p-wave DOS calculated curves. At this temperature, it is difficult to see much difference between the two calculated curves as broadening effects cause them to appear very similar. Fitting parameters are shown later in Table 4.0a.	45

Figure 4.3:	(a) A schematic of the standard proximity effect picture showing the induced superconducting energy gap[61], Δ , at an interface as a function of position x , where F is the superconducting condensate amplitude. The pairing interaction constant, g , is generally taken to have the form of a clear step function, but at small scales, the step actually has a finite slope due to electronic screening [62]. (b) A schematic illustration for the geometry of the STM probe scanning over the surface of TI Bi_2Se_3 in proximity to a PbBi island. In this experiment, we are interested in measuring the superconducting coherence length in the plane parallel to the TI surface, not in the normal direction to the surface as done in many other experiments.	48
Figure 4.4:	(a) STS taken on a 250 nm thick film of $\text{Pb}_{0.3}\text{Bi}_{0.7}$ deposited on Bi_2Se_3 and fit with a calculated s-wave DOS that has been appropriately broadened to account for thermal and scattering effects. (b) Four-probe measurement taken on a 400 nm thick film of $\text{Pb}_{0.3}\text{Bi}_{0.7}$ taken by Dr. Reza Loloee. The transition temperature of 8.3 K closely matches the nominal value of 8.2 K. [64] Both measurements taken at 4.2 K.	50
Figure 4.5:	EDS measurements taken on our 250 nm thick PbBi film showing the actual atomic composition of our alloy. EDS showed that the actual film composition was 36% Pb and 64% Bi, which is well within the expected composition range for our superconducting islands.	51
Figure 4.6:	Image taken under optical microscope showing the superconducting array pattern after thermal evaporation. This sample was exposed to air and was therefore not measured under STM.	52
Figure 4.7:	(a) and (b) Atomic force microscopy (AFM) topographs of a thermally deposited PbBi dot. We can clearly see a very grainy appearance to the overall dot, but upon closer inspection it is clear that the dot is comprised of many small superconducting droplets. (c) STM topograph of a PbBi droplet with its respective height profile trace shown in (d). The radius of curvature at the base of the droplet is an artifact due to the radius of the STM tip. The actual interface between the droplet and the TI is very sharp, which is ideal for our measurement. Scale bars: (a) 500 nm (b) 100 nm (c) 40 nm.	53

Figure 4.8: The left panel represents dI/dV curves measured at 4.2 K taken at various distances from a PbBi island. The LDOS displays clear signature of the induced superconducting gap, with the arrows denoting the location of the coherence peaks. The only feature at distances far from the superconducting island is the Dirac cone. Another notable feature of the presented data is visible oscillations outside of the superconducting gap. The right panel represents dI/dV curves measured on different islands at nominally the same conditions. The data shown here demonstrates an increasing DOS for both positive and negative voltages outside of the gap, as opposed to the flat DOS predicted by BCS. This is indicative of Dirac cone states in the superconductor. All data are normalized so that $dI/dV|_{-20\text{mV}} = 1$ 56

Figure 4.9: Total energy gap width measured by STM at 4.2 K with the expected exponential decay fit, described by the function $\text{Gap Width} = 2\Delta_0 e^{-x/\xi}$, demonstrating that as the probe moves further from the PbBi droplet, the superconducting gap decreases in width. Here the best fit gives a pairing potential of $\Delta_0 = 3.64 \pm 0.40$ meV and a coherence length of $\xi = 540 \pm 200$ nm. In order to extract Δ for each data point, we first took linear fits from $-6 - -1$ mV and $1 - 6$ mV of the dI/dV curve and subtracted them from the full data in order to enhance the coherence peaks on both sides of the Fermi level. The inset shows the data and fitting curve over an expanded distance range. 57

Figure 4.10: (a,b) The local density of states in the diffusive limit as a function of energy (a) at different distances from the boundary of $0.5R, 1R, 1.5R$, shown by the red, black, and blue curves respectively, and as a function of position (b) at energies $0.1E_{\text{Th}}, 0.8E_{\text{Th}}, 1.5E_{\text{Th}}$, once again shown by the red, black, and blue curves respectively, with lines representing the linearized analytical result, and symbols the numerical result of full nonlinear Eq. (4.1). The inset show a comparison between the gap found experimentally (blue diamonds) and the analytical result (solid line). (c) The local density of states as a function of energy for the topological insulator surface states to the left of the TI/S boundary at 0, which is treated as bulk superconductor. (d) The local density of states as a function of energy for the topological insulator surface states to the right of the TI/S boundary at 0, which is treated as bare topological insulator. A phenomenological damping has been included, and the bulk density of states are included as a comparison. 61

Figure 4.11:	(a) A schematic illustration for the geometry of the STM probe scanning over the surface of TI Bi_2Se_3 in proximity to a Nb island. (b) A schematic of the standard proximity effect picture showing the induced superconducting energy gap[61], Δ , at an interface as a function of position x , where F is the superconducting condensate amplitude. The pairing interaction constant, g , is generally taken to have the form of a clear step function, but at small scales, the step actually has a finite slope due to electronic screening [62].	63
Figure 4.12:	SEM image taken by collaborator Can Zhang showing a region of Nb arrays. In this sample we are primarily given square and hexagonal arrays with differing distance in between islands. The sample also contains anti-square arrays, circular arrays (like those used previously in our PbBi and Pb measurements), tri-junctions, and loops junctions. The loop junctions would allow us to thread a magnetic field through a superconducting loop and measure the result from the induced phase difference in the Nb junction. The arrays are necessary in order to eliminate the needle in the haystack problem inherent in STM measurements.	64
Figure 4.13:	AFM topograph taken by collaborator Can Zhang showing an array of hexagonal Nb islands. This demonstrates smooth Nb islands with a clean TI substrate.	65
Figure 4.14:	Measurement of the Dirac cone taken far from the Nb arrays. This spectrum was taken at 1.78 K. We believe that the cone is not perfectly sharp due to the small amount of thermal broadening at this temperature.	66
Figure 4.15:	Proximity effect measurement taken near $1 \mu\text{m}$ of a Nb array; the distances from the edge of a Nb island are indicated in the plot, where the red arrows note the location of the coherence peaks. We can clearly see the gap decrease in width as we move away from the island, then begin to increase again as we are most likely getting closer to another array. Measurement taken at 1.6 K.	68
Figure 4.16:	Two spectra taken at different points demonstrating Tomasch/Friedel-like oscillations outside of the superconducting gap. Interestingly, the top curve looks like the oscillations are simply superposed on a normal Dirac cone, but since superconductivity must be present in order for the effects to be observed, it is possible that this measurement was taken near a weak Nb island. Measurements were taken at 1.6 K.	69

Figure 4.17:	Various spectra taken on different Nb islands demonstrating the inverse proximity effect of the TSS on the superconductor. In two curves, we applied fits using calculated s-wave DOS curves that been thermally broadened and had scattering effects applied, where the values of these fitting parameters are shown in the plot. The calculated curves had a temperature of 1.6 K, a coherence length of 38 nm, and a thickness of 60 nm. Surprisingly, we cannot see clear coherence peaks in the superconducting gaps potentially due to the induced TSS forming p-wave superconductivity in the Nb islands. All measurements were taken at temperatures between 1.5-1.8 K, where the superconducting gap is expected to be both very deep and to have sharp coherence peaks. The top curve is a Dirac cone measured in a region of the sample where no Nb islands had been deposited.	70
Figure 4.18:	Room-temperature spectra taken on and off Nb islands. The 3 curves on the left were taken on Nb islands found in the same array while the curves on the right were taken at 3 separate locations on bare Bi ₂ Se ₃ . We believe that this is the signature of the Dirac cone on Nb at room temperature, which indicates that this inverse proximity effect is likely not dependent on the superconducting state of the Nb and therefore must stem from some other mechanism.	71
Figure 4.19:	LDOS data with theoretical curves based on a model that includes native metallic states and proximity coupled TI surface states. Model 1 (blue) has no BCS pairing. Model 2 (purple) has BCS pairing in the native metallic states only. Model 3 (red) has pairing in both the native and the proximity-coupled TI states.	74
Figure 4.20:	Experimental data of the DOS taken on 3 separate islands with calculated fits demonstrating the leakage of the TSS into the superconducting Nb islands. (a-c) all utilize v_F , γ , and a broadening term Γ as free parameters while (d-f) allow Δ to be a free parameter in the calculation as well. In general, (d-f) have better fits as it is expected that Δ will be influence by both the proximity to the TI material as well as the TSS states leaking into the superconductor.	75
Figure 5.1:	Schematics of the proposed measurement which will utilize SCAI measurements to measure the path of the Josephson current in a biased S/TI/S junction.	79
Figure A.1:	STS taken on a 400 nm thick layer of Pb deposited on the surface of Bi ₂ Se ₃ . Here we can see a very clear superconducting gap as well as signatures of phonon oscillation modes outside of the superconducting gap. This measurement was taken at 4.2 K.	82

Figure A.2:	AFM topograph of Pb islands deposited on the surface of Bi_2Se_3 . The islands are grainy, much like the PbBi samples, but also are heavily oxidized due to the intrinsic nature of Pb exposed to air.	83
Figure A.3:	STM data taken on a sample made with Pb/ Bi_2Se_3 . While we can see a pretty clean interface, the STS data show induced gaps that are far too wide to be superconducting. We believe that these gaps stem from charge density waves caused by lattice misalignment of the TI crystal. We exclude data from position 4 in the image due to very high mechanical instability at the interface.	84
Figure B.1:	Figure taken from Wu et. al. demonstrating the possible behavior of the TSS when a CI is put in contact with a TI. The TI will either “topologize” the CI, causing the TSS to float to the surface, become trivialized by the CI, pushing the TSS down one QL, or the materials will not affect one another in any meaningful way, leaving the TSS at the interface.[2] . . .	86
Figure B.2:	DFT calculation taken from Wu et. al. showing the band structures of differing TI/CI interfaces, specifically $\text{ZnS}/\text{Bi}_2\text{Se}_3$ (a-d) and $\text{ZnSe}/\text{Bi}_2\text{Se}_3$ (e-h). The dots indicate the spectral weights and contributions from differing atoms, denoted by the size and color respectively. DP_U and DP_L denote the Dirac points of the upper and lower surfaces respectively.[2]	87
Figure B.3:	(a) AFM phase retrace demonstrating different materials on the surface of a baked sample. (b) STM topograph of the sample, demonstrating the same features seen in the AFM scan shown in (a).	90
Figure B.4:	Diagram showing sample after baking and assembly. The sample itself is usually around 3 mm in size in order to allow for a large area to scan using our surface probes.	90
Figure B.5:	(a) The electric field between the tip and the TSS in the ZnSe terrace has a set capacitance C_{ZnSe} . (b) The electric field between the tip and the TSS in the Bi_2Te_3 layer with a capacitance of $C_{\text{Bi}_2\text{Te}_3}$. Here we would see a smaller capacitance because of the larger distance between the two capacitive “plates”.	91
Figure B.6:	Compressibility measurement taken over various bare Bi_2Te_3 at 77 K. While there is a notable slope present in these measurements, we see what we believe to be the Dirac cone near 1–1.5 V in these curves. This would be the key signature of the topological surface state and is expected when over a bare TI. All curves shown are averages of thousands of individual curves in order to suppress noise and enhance the signal. The black curves are the raw data while the red curves are the results of smoothing the raw data.	93

Figure B.7:	Compressibility measurement taken over various ZnSe terraces at 77 K. Aside from the apparent slope, there are no notable features in these measurements. The lack of a step in the capacitance or appearance of the Dirac cone indicates that there is no induced topological surface state in this specific interface. All curves shown are averages of thousands of individual curves in order to suppress noise and enhance the signal.	94
Figure B.8:	(a) STM topograph showing the clear different regions of ZnSe and Bi ₂ Te ₃ . (b) STM spectroscopy measurement taken on bare Bi ₂ Te ₃ showing the usual density of states for a Dirac cone at room temperature.	95
Figure B.9:	(a) Kelvin probe topograph showing regions with differing surface potentials. Please refer to Appendix C for a discussion on how the nulling voltage V_N is acquired. (b) Kelvin probe spectrum taken in the dark region at the bottom of (a). The resulting nulling voltage V_N is -1.035 V. (c) Kelvin probe spectrum taken in the bright region of (a). Here, V_N is -1.132 V. While it would have been interesting to take STM spectroscopy in these regions to see if the Dirac cone shifted, it was not possible with this sample due to poor conductivity at 77 K.	96
Figure C.1:	A plot simulating three dC/dz measurements taken at the same point at different values of z_0 . Here we can see the crossing point occurs at a voltage of .5 V and at a measured value of 4 for dC/dz . This tells us that the nulling voltage would then be .5 V and the arbitrary offset from the measurement electronics has a value of 4.	100

Chapter 1

Introduction

Scanning tunneling microscopy (STM) has become a staple for measuring the electronic states in conducting materials in condensed matter physics. By utilizing one of the many unique phenomena of quantum mechanics, known as quantum tunneling, a conducting tip can be brought into close proximity with a voltage-biased conducting material and an electrical current will flow. This occurs because individual electrons tunnel through the vacuum barrier between the tip and the sample. This measurement technique allows us to not only map out the topography of a sample, but also to probe the local density of states of the material as well. By fixing the point over a location of interest and sweeping the bias voltage, we can measure the current response and extract the density of states. This is an exceptionally powerful and flexible tool when it comes to observing the details of the electronic states near interfaces with different materials placed in proximity to one another. In this dissertation, I will focus on the interfacial interactions of superconductors and topological insulators as well as conventional insulators and topological insulators.

Three-dimensional topological insulators are a recently discovered class of semiconductor for which intrinsic electron spin-orbit coupling gives rise to spin polarized channels; these channels cross the semiconducting gap with a linear dispersion relation, which is commonly known as the Dirac cone. States found in the Dirac cone reside on surfaces and have their spin and momentum coupled in very unusual ways. These states are known as topological

surface states (TSS), and will be one of the central focuses of the electronic measurements presented in this dissertation.

Another central focus will be in the phenomenon known as superconductivity. Superconductivity was initially discovered as a phase of matter in which there is zero resistance below some critical temperature. In 1957, Bardeen, Cooper, and Schrieffer provided the microscopic theory to describe this phenomenon, which is now known as BCS theory. Superconductivity arises from completely different physics than topological insulators: a spontaneously-broken gauge symmetry results in Cooper pairing, which is an intricate dance of electron charge and spin. [1] This is crucial to superconductivity as bosons are capable of inhabiting the same quantum state, unlike fermions. Furthermore, Cooper pairs are capable of moving from one material to another. When a superconductor is placed in contact with a normal metal, the Cooper pairs do just that, and the normal metal experiences induced superconductivity out to a finite distance. This is known as the superconducting proximity effect and is one of the primary focuses of this dissertation: specifically the superconducting proximity effect in the topological surface state of a topological insulator. The induced superconductivity in the topological surface state is predicted to form a two-dimensional p-wave superconductor, and is of great interest to the scientific community because this specific form of superconductivity is believed to house Majorana fermions, which are particles that are also their own antiparticles.

A great deal of work went into studying the interfacial effects of conventional insulators on topological insulators, which is presented in the Appendix B. It has been predicted that the location of the topological surface state can be tuned by placing a very thin conventional insulator (CI) on top of a topological insulator. [2] The topological insulator can either “topologize” the CI, causing the TSS to float to the surface of the CI and away from the top layer of the TI. Likewise, the CI could trivialize the top layer of the TI, pushing the TSS

down one layer into the TI. The third option is the traditionally expected behavior in which the TSS remains at the TI/CI interface. These three possible effects are known as the “dual” proximity effect. For these measurements we utilize a special scanning probe method known as subsurface charge accumulation imaging (SCAI).

This dissertation will present all of the above material as follows: first, I will introduce the relevant scanning probe methods used in this work in Chapter 2. Next, in Chapter 3, I present the relevant theories necessary to have a basic understanding of the results presented, namely the theories of topological insulators and superconductivity. In Chapter 4, I show the results of STM measurements taken on topological insulators with superconducting islands deposited on the surface, which demonstrate some striking behaviors in the density of states. Finally, I conclude this dissertation with a discussion of my results and the future experiments that my work has laid the path for in Chapter 5. A discussion on preliminary work in the superconducting proximity effect and the dual proximity effect of conventional insulator/topological insulator interfaces can be found in the appendices.

Chapter 2

Experimental Techniques

2.1 Scanning Tunneling Microscopy

Scanning Tunneling Microscopy (STM) is a very powerful and well established measurement technique in the world of surface physics. By placing a nanoscale conducting tip in very close proximity to a conducting sample (on the order of 1 nm away) and applying a voltage between the two, we can image structures on the scale of angstroms through the use of the quantum mechanical phenomenon known as tunneling. But the truly powerful capabilities of STM come from the ability to take spectra, which allow us to measure the local density of states (LDOS) of the conducting sample. While STM may appear to be a very simple measurement method, the underlying physical mechanisms and executions are actually very complex.

2.1.1 Tunneling Theory

STM is directly dependent on quantum mechanics, more specifically on electron tunneling. This mechanism can be simplified down to a one-dimensional, trapezoidal barrier of width l in between two regions of differing Fermi energy. The barrier is formed by the different work functions of the materials. Taking the left side of Fig.2.1 to be the sample and the right side to be the tip, it can be seen that an incoming electron from the sample's side can actually

tunnel across this gap into the tip. This is governed by the behavior of the electron wave function, $\Psi(z)$, and its interaction with the barrier. The wave function is well understood to undergo exponential decay inside the barrier, taking the form $\Psi(z) = Ae^{-\kappa z}$, where A is a normalization factor. Assuming the bias energy, eV, is small compared to the work functions of the sample and tip ϕ_S and ϕ_T , we can approximate the barrier as rectangular and the barrier height would be $\phi_{avg} = (\phi_S + \phi_T)/2$, and the exponential damping factor is $\kappa = \sqrt{2m\phi_{avg}}/\hbar$. After tunneling through the barrier, the wavefunction resumes its

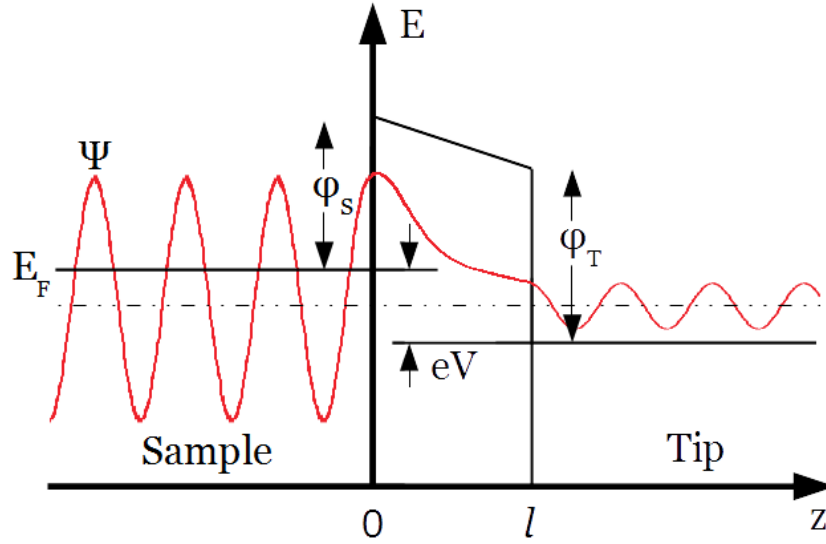


Figure 2.1: Vacuum barrier between a tip and sample, with the electron wave function shown in red. This demonstrates that a propagating electron has the ability to tunnel from the sample to the tip when a voltage is applied between them. Here, eV is the contribution from the bias voltage.

oscillatory form $\Phi(z) = \Gamma e^{ik_F z}$, where Γ is the transmission coefficient and k_F is the Fermi wave number. Because the wave function must be continuous at the barrier interface, we can clearly see that $\Psi(l) = Ae^{-\kappa l} = |\Gamma|$ when the slope of Ψ inside the barrier is small; the wavefunction inside the barrier must equal the amplitude inside the tip at the interface. Due to the fact that the tunneling current is proportional to the to transmission probability $|\Gamma|^2$,

we arrive at the important relation

$$I \propto e^{-2\kappa l} \tag{2.1}$$

This relation is highly oversimplified due to other factors such as the three-dimensional tip geometry and thermally excited electronic states in the tip and sample, but the crucial point is that the tunneling current has an exponential dependence on the distance between the tip and sample. Since the work function of regular metals is around 5 eV, $\kappa \approx 1 \text{ \AA}^{-1}$, implying that if the tip moves only 1 \AA further from the sample the tunneling current would drop 1 order of magnitude. It is due to this exceptional sensitivity that STM is such an effective and sensitive tool when scanning in the xy-plane.

2.1.2 Scanning Tunneling Spectroscopy

Arguably the most powerful aspect of STM, Scanning Tunneling Spectroscopy (STS) allows for the measurement of the sample's LDOS. By fixing the tip over a designated location and sweeping the bias voltage (see Fig. 2.2), we are able to acquire the sample's I-V characteristics, and more importantly its differential conductance dI/dV . This quantity is related to the LDOS, but it is affected by thermal excitations (on the order of 25 meV at room temperature); STS is exceptionally effective at temperatures near 0 K, where thermal energy is nearly gone.

To fully understand the significance of STS, we will now discuss qualitatively how dI/dV relates to the sample's LDOS. We first must assume that the tunneling transition occurs at constant energy once the bias voltage has been applied. We can then sum all of the contributions from each energy level to calculate the total tunneling current. Since we are working at a finite temperature $T > 0$, the number of occupied states for a sample is simply

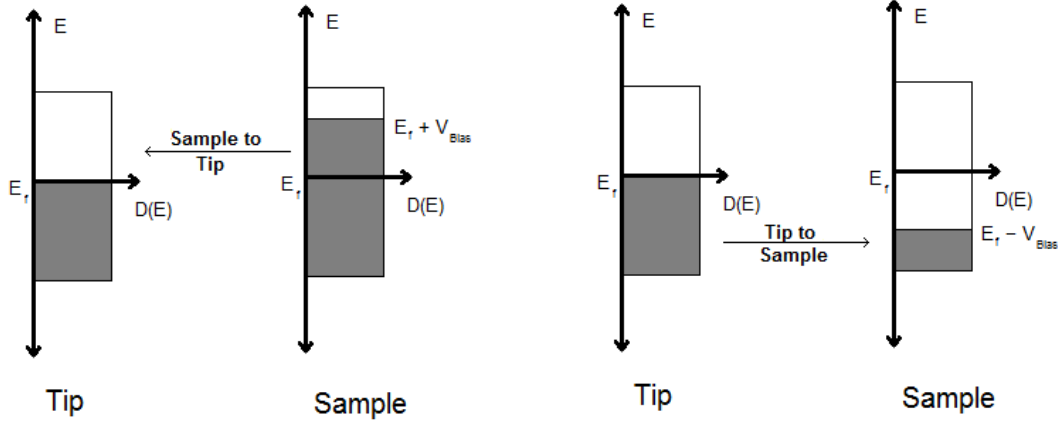


Figure 2.2: By sweeping the bias voltage, we are able to fill (empty) the empty (occupied) states of the sample. As the tunneling current depends on the number of accessible states, this allows us to extract its LDOS.

the sample's density of states, $N_s(E)$ convolved with the Fermi function $f(E)$. Here, the Fermi function is defined as $f(E) = 1/(1 + e^{E/(k_B T)})$, and the occupied number of states is simply defined as $N_s(E)f(E)$. Electrons found in these states can only tunnel into the empty states found in the tip. This value is given by $N_t(E - eV)(1 - f(E - eV))$. Putting it all together, we can see that the tunneling current from sample to tip takes the form

$$I_{s \rightarrow t} \propto \int_{-\infty}^{+\infty} |\Gamma|^2 N_s(E) f(E) N_t(E - eV) [1 - f(E - eV)] dE \quad (2.2)$$

where $|\Gamma|^2$ is the tunneling probability.

Assuming the transmission probability is independent of E for energies close to the Fermi level, it can be pulled out of the integral and factored into a prefactor in our proportionality equation. To obtain the net tunneling current, we simply need to subtract the current going

from the tip to the sample, $I_{t \rightarrow s}$. This results in the equation

$$I \propto \int_{-\infty}^{+\infty} N_s(E) N_t(E - eV) [f(E) - f(E - eV)] dE. \quad (2.3)$$

To simplify Eq. 2.3 further, the fact that our STM tips are usually made from noble metals and alloys, we can assume $N_t(E)$ is approximately constant near the Fermi level, so N_t is independent of E . If we differentiate the tunneling current in Eq. 2.3 with respect to voltage, eV , we get

$$\frac{dI}{dV}(V) \propto \int_{-\infty}^{+\infty} N_s(E) \left[-\frac{\partial f(E - eV)}{\partial(eV)} \right] dE \quad (2.4)$$

Equation 2.4 can be simplified even further due to the fact that $-\partial f(E - eV)/\partial(eV)$ is a bell-curve centered at $E = eV$ with a width on the order of $k_B T$ and unitary area beneath the curve. Thus, as $k_B T \rightarrow 0$, equation 2.4 simplifies down to

$$\left. \frac{dI}{dV}(V) \right|_{T=0} \propto N_s(eV) \quad (2.5)$$

and it is directly evident that at low temperatures, the differential conductance dI/dV is directly proportional to the sample's density of states. STS is an exceptionally powerful tool due to the fact that all of this can be done on a mobile tip, allowing us to measure the IDOS anywhere we wish on the sample surface.

2.1.3 Experimental Setup

2.1.3.1 Besocke Design STM

The microscopes used in our lab are house-built Besocke design STM's. The Besocke design consists of four piezoelectric tubes: three of which hold and manipulate the sample and one to raster the STM tip over the surface.[3] A schematic of this setup can be seen in Fig. 2.3(a), and the real microscope can be seen in Fig.2.3(b). Besocke design STM's utilize an

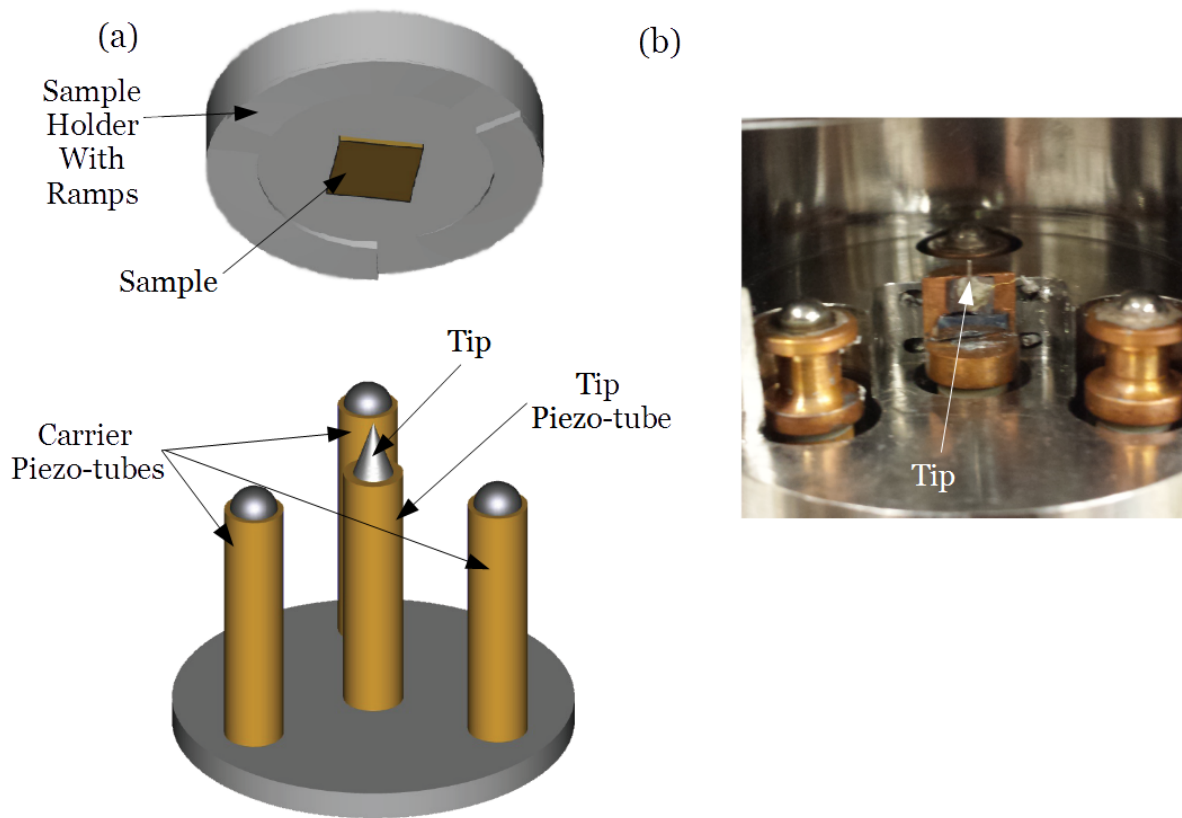


Figure 2.3: (a) Schematic showing the layout of a Besocke design STM. (b) Actual house-built STM in the Tessmer lab.

inertial approach method for bring the sample into tunneling range with the tip. With the conducting hemispheres on top of the carrier piezo tubes supplying the voltage to the sample,

the carrier piezo tubes first bend in a such a manner to bring the sample holder closer to the tip then abruptly snap back. Due to the large inertia of the sample holder and low friction between the conducting hemispheres and the sample holder, the sample does not move back to its initial position. While this is happening, the tip piezo tube extends in an attempt to find a tunneling current. If tunneling current is not produced, the tip retracts and the entire process is repeated until the sample is in tunneling range.[3]

This design is ideal for cryogenic STM measurements due to the rigidity of the setup. Because all of the piezoelectric tubes are soldered to the same base plate and are identical dimensionally, thermal expansion and contraction are no longer major issues when scanning at low temperature.

2.1.3.2 Cryogenic STM System

Our STMs are placed on the end of a long dipping stick in order for us to be able to lower the tip-sample system into a cryogenic dewar. In our lab we use two liquid helium cryostats capable of reaching a temperature of 300 mK, which utilize suspension methods in order to isolate the whole system from vibrations. The complete system with microscope fully loaded into the dewar is shown in Fig. 2.4.

The cryostat consists of a central sample tube into which the microscope is lowered from the top. This sample tube is typically kept at a vacuum of around 5×10^{-6} torr, and is ideal for keeping the sample surface clean and free of contaminants. This sample tube also contains a carbon based sorption pump (sorb) to absorb any excess gases in the chamber. Outside of this central chamber is an inner vacuum chamber (IVC) which serves to isolate the walls of the sample chamber from the walls of the helium bath. In order to cool the microscope more effectively, we typically have a small amount of helium exchange gas in the

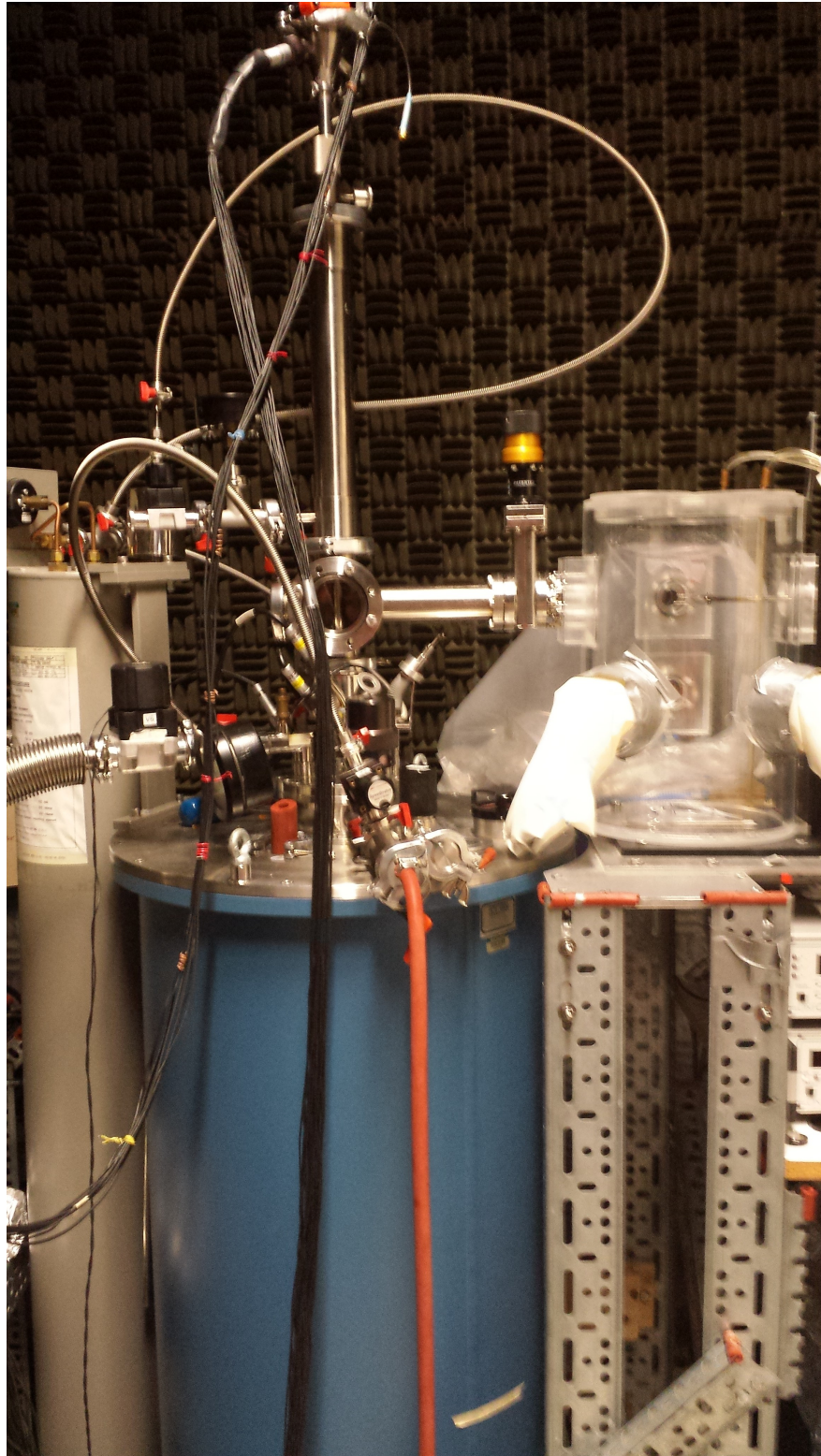


Figure 2.4: The full measurement setup with STM dipper fully submerged in the blue liquid Helium dewar.

IVC to equilibrate the walls. Outside of the IVC, we have the helium/nitrogen bath, where the cryogenic liquid is stored for the duration of our cryogenic experiments. Finally, we have the outer vacuum chamber (OVC), which serves to isolate the cryogenic bath from outermost walls of the cryostat which are at room temperature. The OVC also houses multiple layers of mylar, which shield the microscope from outside radiation sources. A simple diagram of the cryostat can be seen in Fig. 2.5.

Inside of this cryostat are two more important devices. First, we have a superconducting magnet that can supply 5 or 10 T depending on which system we use. The other important device in the dewar is the 1 K pot, which allows us to cool the microscope down to 300 mK when using ^3He . This is also crucial because some signals that we measure are strongly suppressed due to thermal excitations. When the 1 K pot is not in use, the system is usually operating at a temperature of 4.2 K from the ^4He bath.

2.2 Scanning Charge Accumulation Imaging

While STM may be an excellent probe of conducting materials, it still has one major drawback. Many times there is a great deal of electronic structure occurring many nanometers beneath the surface. It is in this regime that STM falls short. Fortunately, another scanning probe method was developed by Dr. Stuart Tessmer and Dr. Ray Ashoori that allows for probing these subsurface states, known as scanning charge accumulation imaging (SCAI). Aside from STM, SCAI is the Tessmer lab's main area of expertise.[4, 5] This measurement method is especially relevant for the data presented in Appendix B.

SCAI is highly sensitive to charges, with a noise level of $.03 e/\sqrt{Hz}$ at 0.3 K. Because this method is such a fantastic detector of changes in charge, it is primarily used to measure

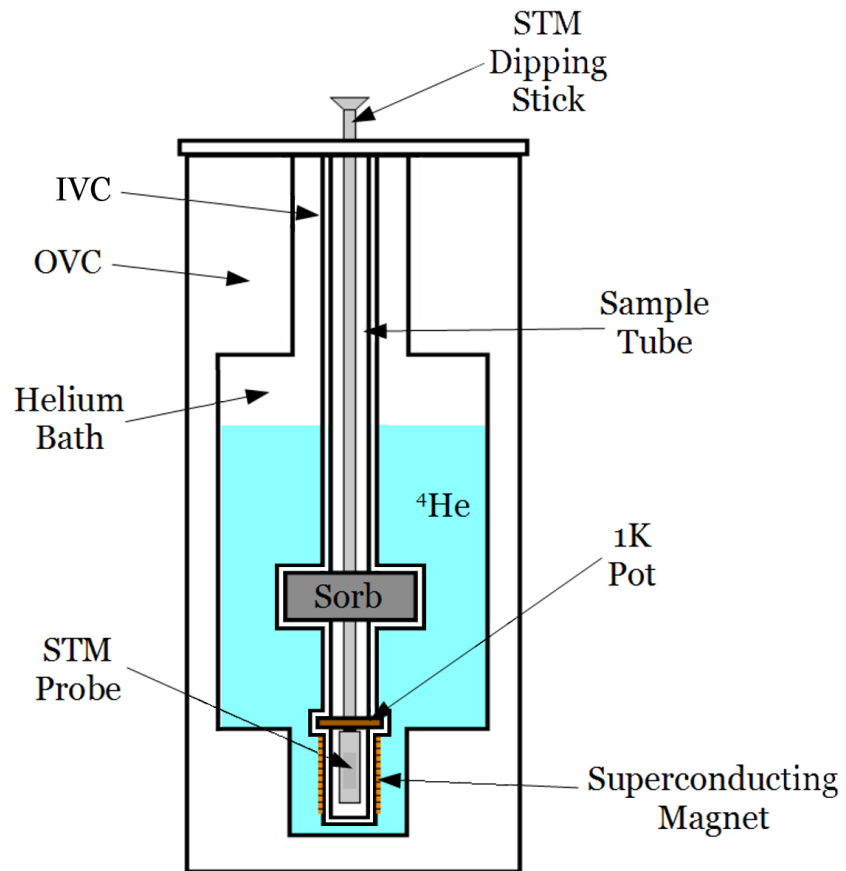


Figure 2.5: Diagram of cryostat used in our lab, showing all of the important chambers and features. Here, the sorption pump (Sorb) is in the shape of a torus and is found inside of the vacuum chamber, which allows the STM to pass through it and reach the bottom.

capacitance between the tip and the sample. This can be done by sweeping the bias-voltage between the tip and the sample while measuring the charge accumulation on the tip, which under ideal conditions perfectly mirrors the charge accumulation in the sample. The capacitance is then extracted from these quantities by the equation

$$C = \frac{dq}{dV} \approx \frac{\Delta q}{\Delta V} \quad (2.6)$$

where Δq is the oscillating charge signal detected by the lock-in amplifier, and ΔV is the AC excitation voltage. From here on out we shall label this quantity as the measured capacitance C_m .

Like STM, SCAI is capable of measuring the density of states of the sample, but instead of the local density of states, SCAI measures the thermodynamic density of states (DOS_{Th}). In these measurements, DOS_{Th} can be extracted C_m using the following relation:

$$\frac{A}{C_m} = \frac{A}{C_G} + \frac{1}{e \frac{dn}{d\mu}} \quad (2.7)$$

Here, we estimate the geometry of the measurement as a parallel plate capacitor of area A , where C_G is the geometric capacitance between the tip and sample and $dn/d\mu$ is the DOS_{Th} . The general definition of C_G is shown in Fig. 2.6. Because we use the same material for our tip in SCAI as we do for STM, we can assume that the density of states for the tip is constant, as we did before in Section 2.1.2. Since C_m is always measured with a stationary tip, C_G will remain constant and any changes as a function of DC bias voltage seen in the capacitance signal will stem from the DOS_{Th} . While this measurement may seem straightforward, an intricate circuit is required in order to full resolve these capacitive changes, which are normally

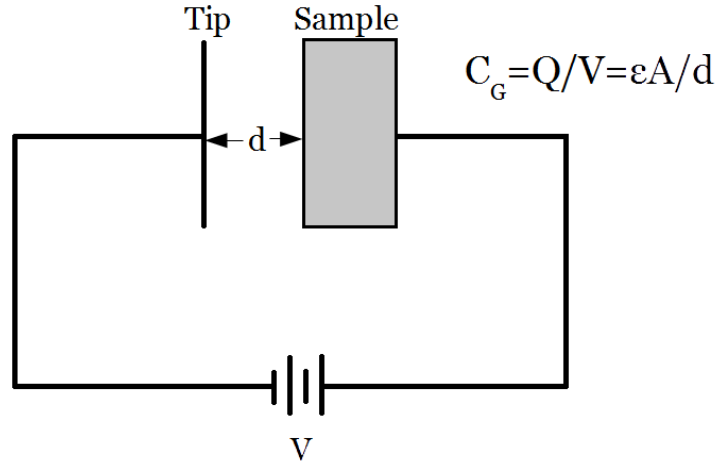


Figure 2.6: A highly simplified diagram demonstrating the relationship of geometric capacitance C_G on the distance between the tip and the sample.

on the scale of 1 aF, or attoFarad (10^{-18} F).

The most important component in our SCAI circuit (aside from the scanning probe tip) is the high-electron-mobility transistor (HEMT), which is what gives us such incredible charge sensitivity. The scanning probe tip is connected directly to the gate of the HEMT, which allows us to measure voltage change in the tip. The HEMT circuit gives us excellent charge sensitivity due to the small capacitance between the gate and the source/drain channels, as discussed below. A diagram of the HEMT circuit used in these measurements is shown in Fig. 2.7(a).

In order to get the maximum sensitivity to the signal of interest to the lock-in amplifier, we have placed a standard capacitor (C_s) in the circuit. C_s subtracts away the background capacitance, stemming from electric fields that do not terminate on the tip apex. This is accomplished by supplying C_s with an AC voltage that is of equal amplitude, V_{exc} , but 180° out of phase with the AC voltage supplied to the sample. From here, we can model the remainder of the circuit as a simple voltage divider, as shown in Fig. 2.7(b). In doing so, we

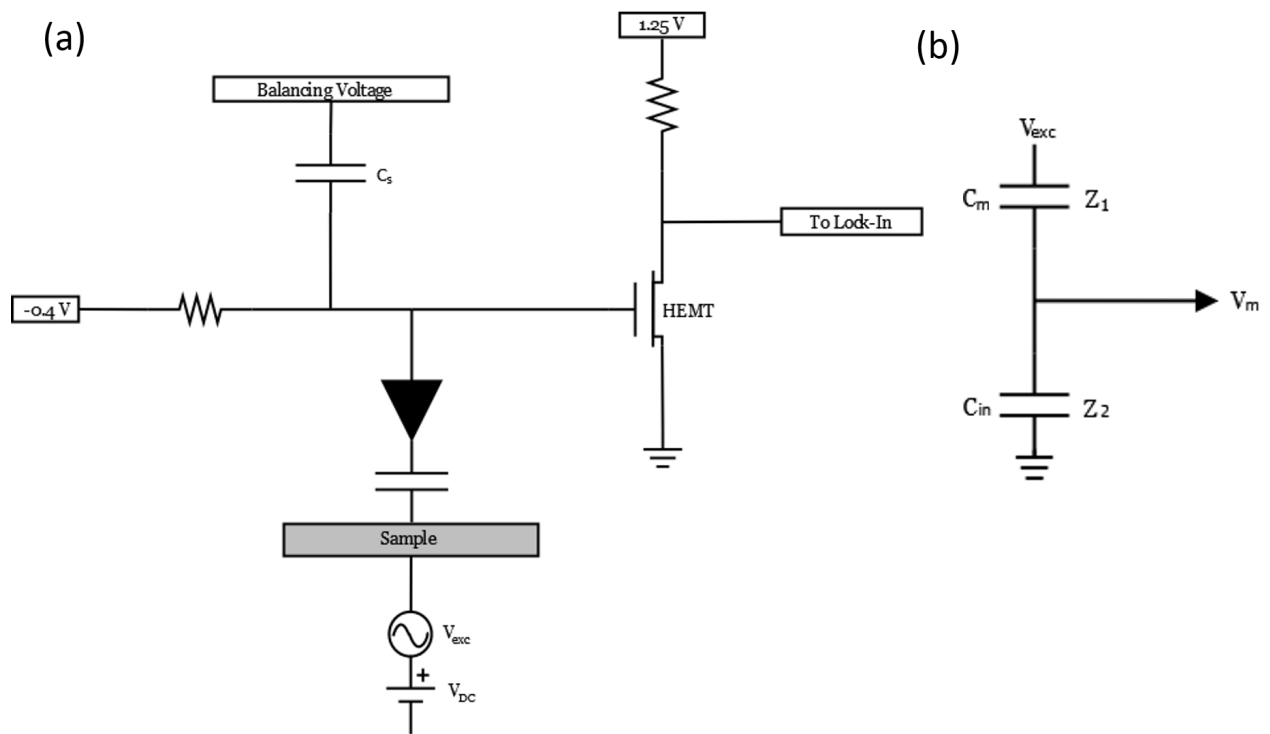


Figure 2.7: (a) Circuit diagram of our SCAI measurement chip. The HEMT acts as a highly sensitive charge detector that is directly connected to the scanning probe tip, which allows us to see charge fluctuations in the sample due to image charges formed in the tip. (b) Simplified diagram demonstrating the existence of a voltage divider for the AC excitation voltage going through two capacitors.

must consider V_{in} and V_{out} , which pertain to V_{exc} and V_m/G respectively, where G is the gain factor for the circuit of order unity.

In order to construct this voltage divider equation, we must first define the intrinsic capacitances that must be accounted for in the assembly of the circuit. C_{in} is the input capacitance, which is the capacitance between the gate and the source/drain channel of the HEMT. C_{in} is typically 0.3 pF (picofarads or 10^{-15} F), around three orders of magnitude lower than C_m . Again, C_m is the tip-sample capacitance, which is proportional to the charge on the tip. This results in the voltage divider equation

$$V_m = GV_{exc} \frac{Z_2}{Z_1 + Z_2} \quad (2.8)$$

where $Z_1 = 1/i\omega C_{meas}$ and $Z_2 = 1/i\omega C_{in}$. Because C_{in} is 3 orders of magnitude larger than C_m , we can eliminate Z_2 in the denominator of Eq. 2.8. Thus, the resulting voltage measured by the lock-in, V_m , is

$$V_m = GV_{exc} \frac{C_m}{C_{in}} \quad (2.9)$$

From Eq. 2.9, it is clear that the smaller C_{in} is, the larger V_m will be. Because stray capacitance from the circuit also contributes to C_{in} , we must be very careful to make the measurement circuit as physically small as possible, usually placing the HEMT within 1 mm of the tip. A fully assembled measurement chip and a picture of the HEMT can be seen in Fig. 2.8.

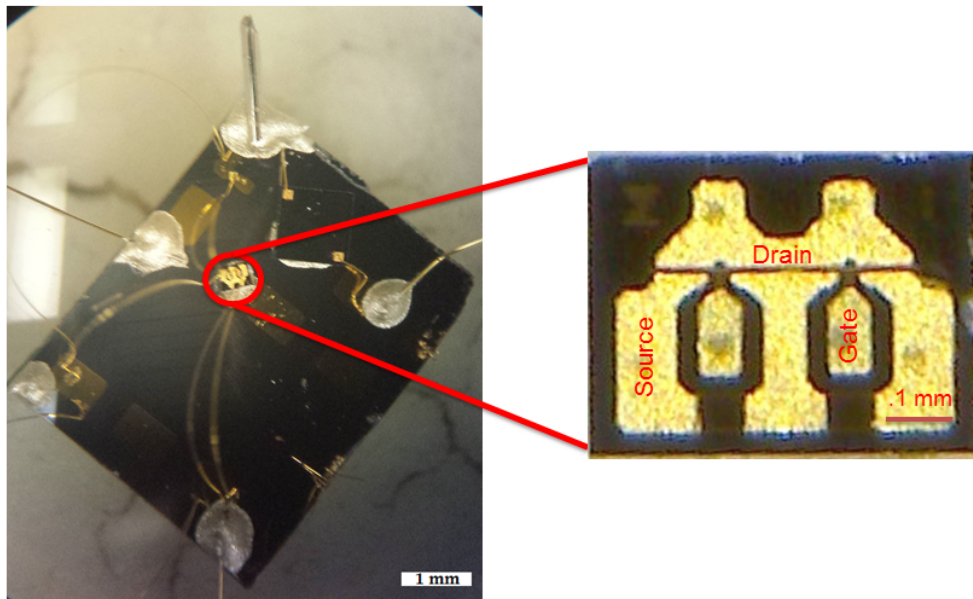


Figure 2.8: The left image shows a fully assembled SCAI measurement chip complete with protection loops. The method of assembly utilizes fine tweezer work with conductive epoxy to fasten the primary circuit elements and connection wires to the GaAs chip. In order to connect the gold pads to the correct elements, we utilize a gold wire bonder. The right image shows a HEMT with no connections. The HEMT as a whole is approximately $600\ \mu\text{m}$ wide and the gate pad itself is only $80\ \mu\text{m}$ wide.

2.3 Tip Preparation

For our scanning probe measurements, we use PtIr tips due to their highly inert characteristics and ideal conductivity. In order to obtain atomic resolution images and high quality spectra, it is important that the tip have a stable, atomically sharp point on the end, or at the very least have a very sharp radius of curvature that is nominally less than a 30 nm.

Typically, the way we form these sharp tips is through mechanical cutting, but there is usually only a 50% success rate of getting sufficiently stable tips using this method. The usual geometry of cut tips can be seen in Fig. 2.11. In order to improve the success rate of tip fabrication, we have investigated a few methods of tip etching, in which the tip is submerged in a CaCl salt solution and a voltage is applied between the tip and a cathode. The initial steps of this etching process typically form tips with a shape shown in Fig. 2.9, where a large bulb of material is left on the end of the tip. This bulb is typically not ideal for scanning probe measurements, so the next stage of etching is known as fine etching. Here, the tip is put in a thin film of the CaCl solution captured in a small tungsten hoop. A smaller voltage is applied between the tip and the hoop, and the neck of the etched tip is gradually etched away until the bulb drops off. When the bulb drops off, a sharp, symmetrical point remains on the end of the tip, usually with a radius of around 20 nm. This gives us an ideal tip for all of our measurement methods, from STM to SCAI.

Unfortunately, when tips have a radius of curvature this small, they become very fragile and sensitive to any physical contact. In Fig. 2.10, we show an etched tip that was dropped when being mounted into the SEM for characterization. This tip is no longer usable in the scanning probe due to the major radius of curvature at the bending point. This just goes to show that any minor contact on the end of the tip can greatly jeopardize the integrity of the

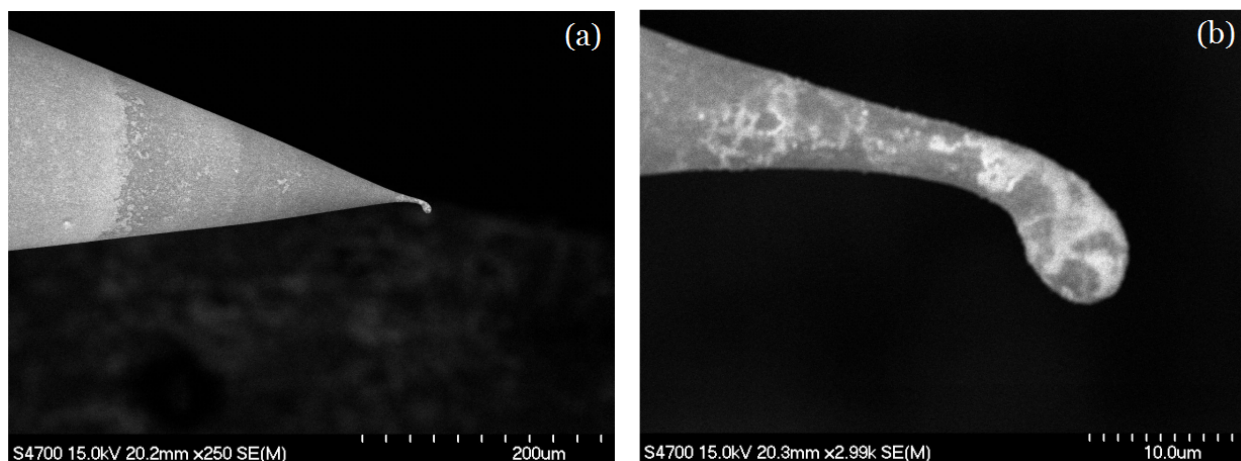


Figure 2.9: SEM images demonstrating the tip geometry after the rough etching step. The bulb at the end will ideally drop off due to gravity assistance during the fine etching process. (a) Initial scan where the bulb is clearly visible and (b) Closer look at the same tip.

experiment, especially if the tip comes in contact with the sample in-situ.

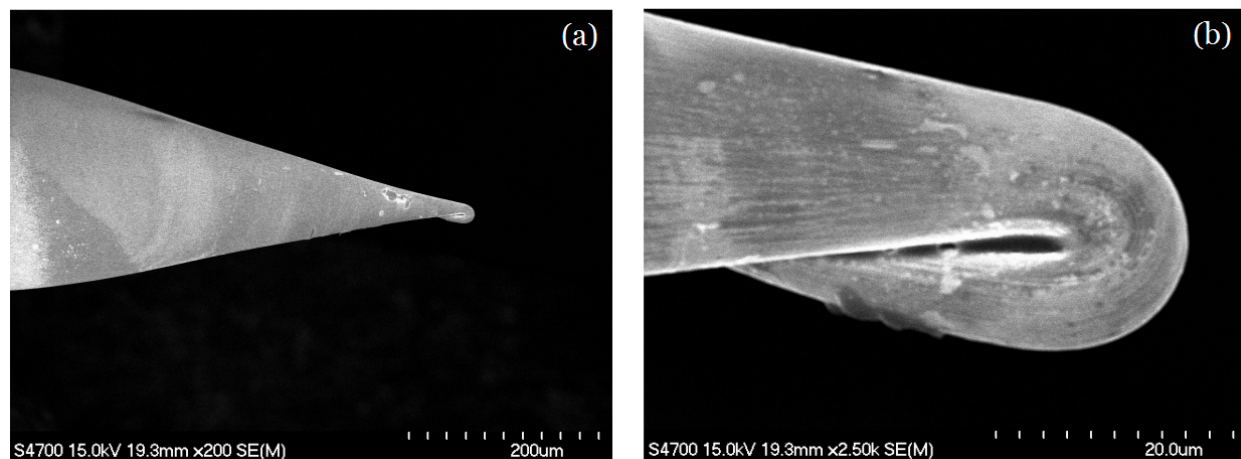


Figure 2.10: SEM images demonstrating what happens to an STM tip when it is dropped. What was once an ideal candidate for use as a scanning probe is now rendered unusable due to the large radius of curvature at the bend in the wire. (a) Initial scan where the bend is clearly visible. (b) Closer look at the same tip.

After a great deal of effort trying to find a repeatable method for tip etching, we eventually found that the most productive way to make tips is to cut 8-10 tips mechanically and image the under SEM for characterization. Using this method, we not only have a chance of producing tips that are in fact sharper than those made by chemical etching, but also know

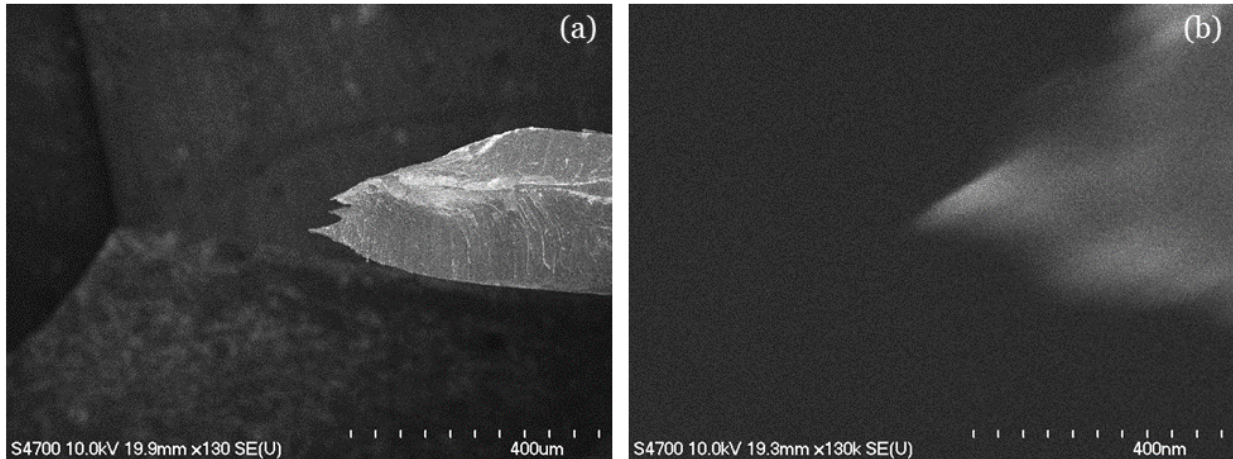


Figure 2.11: SEM images showing the profile of a single cut tip. (a) While the cut tip looks to have multiple points, there is one clear point that is more than $50 \mu m$ further out from the others. (b) Close up of the apex showing that the radius of curvature is less than 40 nm.

the tip geometry, which can be very important for some of the experiments done in this dissertation. An example of an ideal STM/SCAI tip is shown in Fig. 2.11. Here the tip has a very sharp radius of curvature, which is both ideal for tunneling and capacitance measurements. While mechanically cut tips often have multiple points at the end, all that matters is that a single point sticks out sufficiently further than the others. This ensures that we know which part of the tip will be used for the measurements. In the case of the tip shown in Fig. 2.11, it is clear to see that there is a prominent point that sticks out further than the others, which when loaded into the scanning probe system, would be the tunneling/“capacitive plate” point in the measurements.

Chapter 3

The Theories of Topological Insulators and Superconductivity

There are two primary theories at the heart of this thesis: superconductivity and topological insulators. In this chapter, we will briefly discuss the main features of these two generally complicated theories in order to give a basic understanding of the important physics observed in this dissertation.

3.1 Topological Insulators

Topological Insulators (TI) are a relatively recent discovery in the world of condensed matter physics. Topological insulators are materials that are insulating in the interior (as the name implies). This means that the Fermi level lies between electronic bands; the filled band below cannot conduct electricity as every state that is occupied that would carry charge in one direction has a twin state corresponding to the opposite direction, ensuring that the net momentum is zero. To understand the basic principles of TIs, I will introduce some more basic principles which will help clarify the underlying mechanics that are important to topological insulators. First, we will discuss a quantity called the Chern invariant, which can be used to describe the topological nature of a material. Then, we will briefly discuss the quantum Hall effect and quantum spin Hall effect in Sec. 3.1.1 It is important to note

that while the topic of this dissertation is not on quantum Hall physics, these quantum Hall systems display physics which is analogous to the three-dimensional materials I studied, and are useful to introduce the nature of topological insulators. Sec. 3.1.2 presents a more rigorous introduction to three-dimensional TIs.

The Chern number is an important quantity in TI systems. It can be calculated by investigating the Berry phase, which is a geometric phase that a system acquires when it undergoes a closed, adiabatic cycle. The Berry phase can be physically understood by looking at the behavior of Bloch wave functions $|u_m(\mathbf{k})\rangle$ when transporting \mathbf{k} around a closed loop. The Berry phase is given by the line integral of the Berry connection $A_m = i \langle u_m | \nabla_k | u_m \rangle$. The Berry phase can also be expressed as the surface integral of the Berry flux $F_m = \nabla \times A_m$. The Chern invariant is simply the total Berry flux in the Brillouin zone, calculated by the equation

$$\nu_m = \frac{1}{2\pi} \int d^2k F_m \quad (3.1)$$

where k is the electron wave number. The total Chern number is the sum over all occupied bands, $\nu = \sum_{m=1}^N \nu_m$, which turns out to be an integer. [6]

This Chern number can be used to denote the topological nature of a material. Vacuum and other trivial insulators have a Chern number $\nu = 0$. No topologically interesting physics occurs across the interface of two materials with $\nu = 0$. The Chern number is topological in the sense that it is invariant under small deformations of the Hamiltonian. In other words, because the Chern number must be an integer, it cannot be changed at all under deformations that have energies less than the energy between adjacent ν_m 's. However, large deformations of the Hamiltonian can cause the ground state to cross over other bands. This must occur at interfaces where the Chern number changes from one integer to another, giving rise to

partially filled conducting states near the boundary. Nothing interesting happens at the interface of trivial insulators as the Chern number does not change crossing into the vacuum. The materials of interest have Chern numbers other than zero so that interfaces with the vacuum where the Chern number must change produce very interesting effects. To give a concrete example, below we will now discuss the quantum Hall effect (Sec. 3.1.2 presents a rigorous introduction to three-dimensional topological insulators).

3.1.1 Quantum Hall Effect and Quantum Spin Hall Effect

In order to fully understand the driving physics in TIs, it helps to first investigate the quantum Hall effect. If we look at a two-dimensional electron system and apply a large enough magnetic field normal to the plane of this system, the Hall conductance of the material can be explained by the equation

$$\sigma_H = \nu e^2/h \tag{3.2}$$

where σ_H is the Hall conductance, e is the electron charge, h is Planck's constant, and ν is an integer known as the filling factor. [7] The Hall conductance is quantized in units of e^2/h . The B-field applied to this two-dimensional system causes the electronic states to form into Landau levels. The filling factor ν is the number of filled Landau levels and is defined by $\nu = nhc/eB$. [8] It turns out that the filling factor ν actually is the Chern number for this case. Lets suppose that $\nu = 1$ in the interior; as the Landau level represents a filled band, the interior is then an insulator. At the edge, as we consider crossing the boundary to vacuum, the density has to go to zero. This necessarily means that the Landau level cannot be completely filled at the edge. Hence a conducting state must occur. Generally speaking, when the Chern number changes from one integer to another, there must be a partially filled

conducting states near the boundary.

The general behavior for the example above can be seen in Fig. 3.1. The electrons on the edge of the two-dimensional electron plane travel along the edge of the material, while the electrons in the center are confined to orbits. These two differing electron states represent conducting and insulating states respectively. Moreover, these edge states are actually impervious to non-magnetic defects in the material due to this quantization, and have allowed for the discovery of a standard value for electrical resistance known as the von Klitzing constant, $R_K = h/e^2 = 25,812.807557 \Omega$. The quantum Hall system can also be used to calculate the fine structure constant α to very high precision. [9]

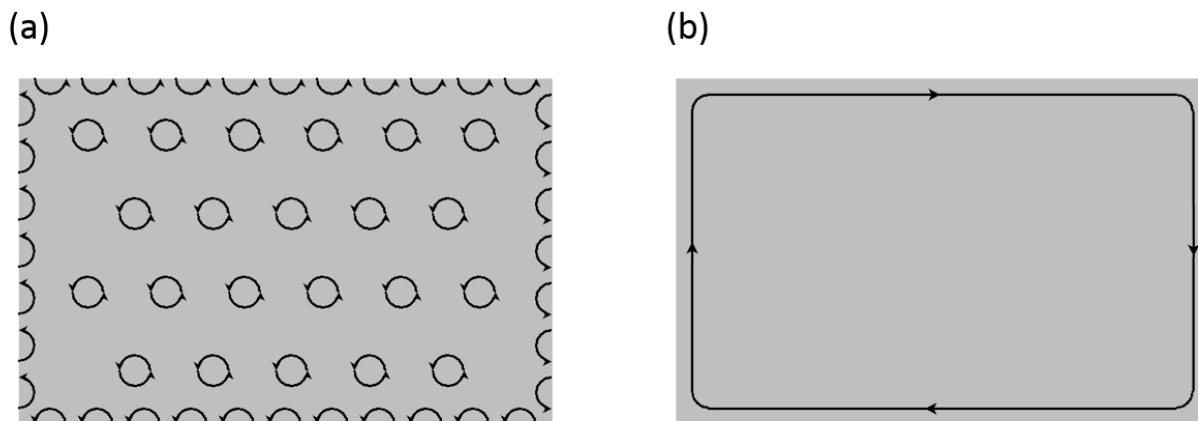


Figure 3.1: A diagram of the quantum Hall system with integer Landau levels filling in the interior in the classical picture (a) and the resulting quantum behavior (b). The edge of the two-dimensional system conducts while the center remains insulating due to the localized states of the electrons. Figure adapted from [6].

More recently, interest was taken in a possible way to create these edge states without having an applied magnetic flux through the two-dimensional system. This resulted in the discovery of the quantum spin Hall effect (QSHE) by Kane and Mele. [10] The quantum spin Hall effect does not need an external magnetic field due to the fact that there is an intrinsic trait known as spin orbit coupling, which does not break time reversal invariance.[10, 11]

This results in two spin polarized edge states in our two-dimensional system, as shown in Fig. 3.2. The resulting effect of this spin orbit coupling creates what is known as the Dirac cone, as shown in Fig. 3.3. The Dirac cone states connect the conduction band to the valence band through these two crossing channels. The novel topological surface states of topological insulators exist solely in the Dirac cone, which is found inside the band gap. Otherwise, the remaining bulk of the material is ideally insulating. In this case, the total edge current ends up being 0, but the individual spin polarized currents at the edge have unitary conductance $\sigma^s = e^2/2h$. [11] The first material found to exhibit the intrinsic behavior was two-dimensional graphene, where Kane and Mele were able to demonstrate the existence of the QSHE using the tight binding model. [12] Many researchers now consider the quantum Hall materials to be the first topological insulators, although only two-dimensional. In order to move forward, we must expand our thinking from two-dimensions to three, as the topological insulators used in this dissertation are three-dimensional.

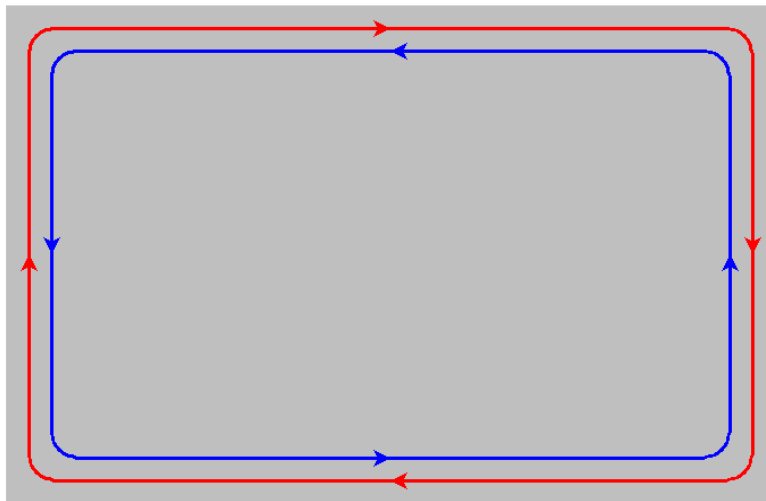


Figure 3.2: This diagram demonstrates the two spin polarized conducting states on the edge of the two-dimensional system, where the red line can be considered to be spin-up electrons and the blue can be considered to be spin-down electrons. Figure adapted from [6].

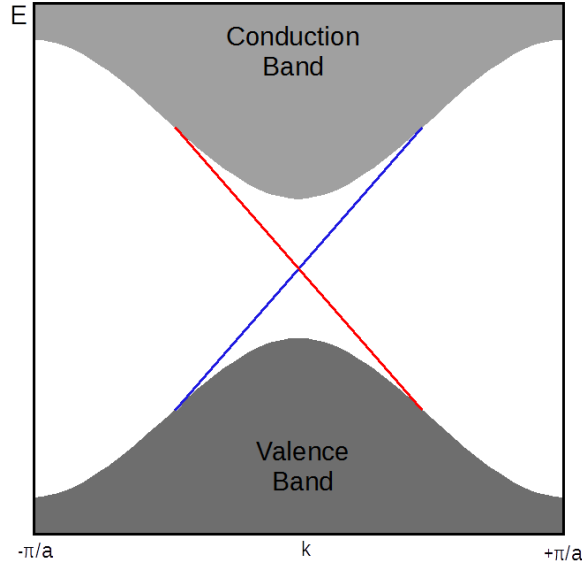


Figure 3.3: The Dirac cone is a consequence of the spin-orbit coupling from in TI's. The red and blue crossing channels correspond to the spin-up and spin-down channels respectively. The crossing point in the center is known as the Dirac point, and is typically not found at the Fermi level E_F of the material. Figure adapted from [6].

3.1.2 3D Topological Insulators and Bi_2Se_3

Three-dimensional topological insulators are a special set of materials in which a boundary with a trivial insulator, such as vacuum, allows for the creation of topologically protected surface states. This topological protection can be described by the notion that time-reversal invariant perturbations cannot open a gap in the topological surface states, but perturbations that break TR symmetry, such as an external magnetic field, can open a gap in these surface states. These materials can be described by what is known as the Chern parity ν . A three-dimensional TI has four Chern parities, defined by ν_0 , ν_1 , ν_2 , and ν_3 , which can all be calculated from the band structure of the material. The Chern parities ν_{1-3} pertain to the xy, xz, and yz planes of the material, while ν_0 defines whether or not the material is a strong topological insulator, a weak topological insulator, or a trivial insulator.[13] If there are an even number of Dirac points enclosed by the Fermi surface, the Chern parity $\nu = 0$,

which is a characteristic of a trivial insulator or a TI with weak spin orbit coupling. For an odd number of enclosed Dirac points, $\nu = 1$, and the material is a TI with strong spin orbit coupling. [14] It is only at interfaces where the Chern parity goes from $\nu = 1$ to $\nu = 0$ (much like the Chern number for a quantum Hall system) that the topological surface state exists.

Since the theoretical formulation and discovery of topological insulators, many materials have been discovered that can be defined as topological insulators. The first true three-dimensional topological insulator found was BiSb. [15] Following in the footsteps of BiSb, more commonly used materials were shown to be TIs, such as Bi₂Se₃, Bi₂Te₃, and Sb₂Te₃. [16] For the three-dimensional TI Bi₂Se₃, the crystal can be described by layers consisting of 2 Bi atoms and 3 Se atoms, known as quintuple layers (QL), as shown in Fig 3.4(a). The chemical bond of the Bi and Se atoms in these QLs is very strong, while the bonding strength between individual QLs is weak and can be described by van der Waals attractions. This conveniently allows us to cleave the crystals by using scotch tape and peeling the top few quintuple layers from the crystal, leaving a clean, atomically flat surface.

For Bi₂Se₃, the existence of the topological surface states can be described by a model which incorporates the effects stemming from the chemical bonding of Bi and Se in the quintuple layers of the crystal, the crystal field of the material, and the basic spin orbit coupling intrinsic to these materials.[17] The states nearest to the Fermi energy exist in the electron p-orbitals of the Bi and Se, so we only need to investigate those orbitals to successfully describe the creation of the topological surface state. The energy states of these p-orbitals are labeled as $|P1_{x,y,z}^{\pm}\rangle$, $|P2_{x,y,z}^{\pm}\rangle$, and $|P0_{x,y,z}^{-}\rangle$, where \pm denotes the parity of the energy state; the behavior of the energy states is shown in Fig. 3.4(b). The chemical bond between the Bi and Se atoms hybridizes their energy states, distancing them from the Fermi level, as shown in Fig. 3.4(b) region (I). Fig. 3.4(b) region (II) demonstrates the

effects of the crystal field splitting of the material. The p_z states for both the Bi and Se atoms are both split from their respective $p_{x,y}$ components, and it turns out that the $|P1_z^+\rangle$ and $|P2_z^-\rangle$ states become the closest energy levels to the Fermi level while their respective $p_{x,y}$ states remain degenerate further from the Fermi level. Finally, we can incorporate the spin orbit coupling of the material by considering the Hamiltonian $H = \lambda L \cdot S$, where λ is the strength of the spin orbit coupling, L is the orbital angular moment, and S is the spin angular momentum. By doing this, we must now take spin into consideration as the spin and orbital angular momenta are mixed. This effect causes a repulsion between the $|P1_z^+, \uparrow\rangle$ and $|P1_{x+iy}^+, \downarrow\rangle$ energy levels (as well as other combinations thereof). This means that the $|P1_z^+, \uparrow\rangle$, $|P1_z^+, \downarrow\rangle$, $|P2_z^-, \uparrow\rangle$, and $|P2_z^-, \downarrow\rangle$ energy levels are pushed closer to the Fermi level. If the spin orbit coupling is strong enough, these energy levels end up crossing the Fermi level, as shown in Fig. 3.4(b) region (III). This results in a band inversion of these two energy levels, and since the $|P1_z^+\rangle$ and $|P2_z^-\rangle$ states have opposite parity, the end result is the topological insulator phase.[17] For Bi_2Se_3 and Bi_2Te_3 , this band inversion occurs only at the Γ point, meaning that the Chern parity for these materials is $\nu = 1$ and that a singular Dirac cone will form at the exposed surface.

An important detail to note is that the Fermi surface taken inside the bulk band gap is no longer degenerate due to the intrinsic spin-polarization of the material. This means that energies above or below the Dirac point will harbor opposite spin polarizations, as shown in Fig. 3.5(a). This spin polarization also protects the TSS from back-scattering from non-magnetic defects because non-magnetic defects cannot flip spin, and thus cannot cause the quasiparticles to flow in the opposite direction.[19] The expected theoretical behavior of the density of states for a topological insulator inside of the band gap is shown in Fig. 3.5(b) when shown from the perspective presented by scanning tunneling spectroscopy. This is the

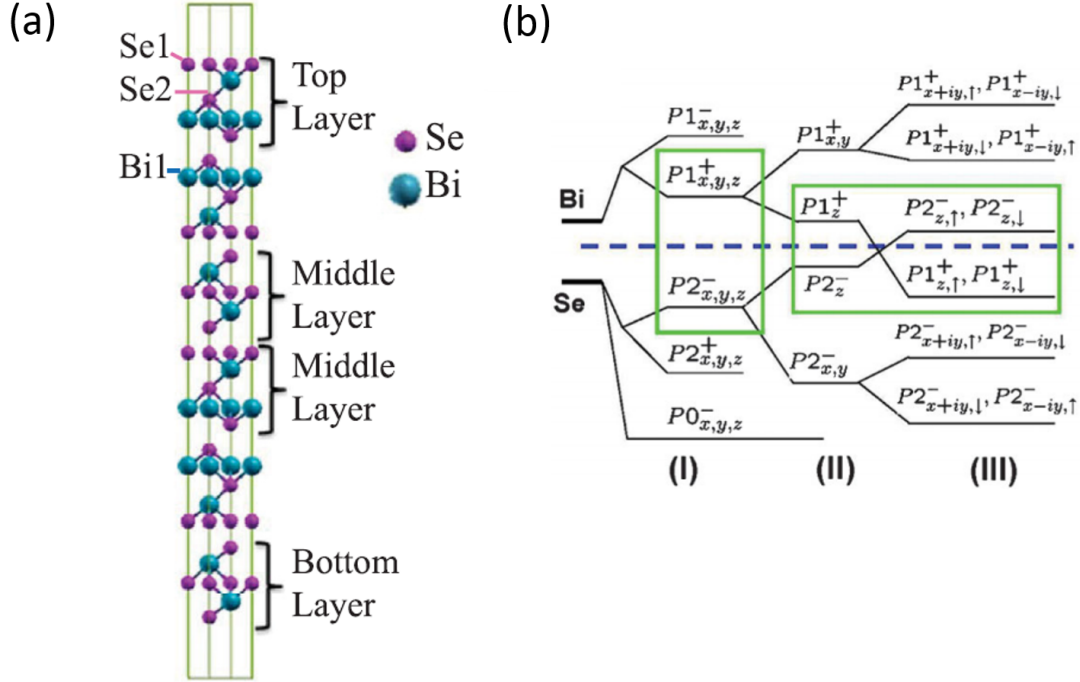


Figure 3.4: (a) Schematic of the structure for Bi_2Se_3 . Bi_2Se_3 is a layered material consisting of stacked quintuple layers made from 3 Se atoms and 2 Bi atoms. The layers are attracted to one another through van der Waals forces and are therefore easy to separate by exfoliation. (b) Schematic showing the p-orbital splitting of Bi and Se near the Fermi level, which is denoted by the dotted blue line. Region (I) takes the chemical bonding of Bi and Se into account, while region (II) further demonstrates the effects on the energy levels from the crystal field. Finally, region (III) shows the effect of strong spin orbit coupling, in which band inversion occurs and the topological phase is created. (a) is adapted from Romanowich et. al. and (b) is adapted from Qi and Zhang. [18, 17]

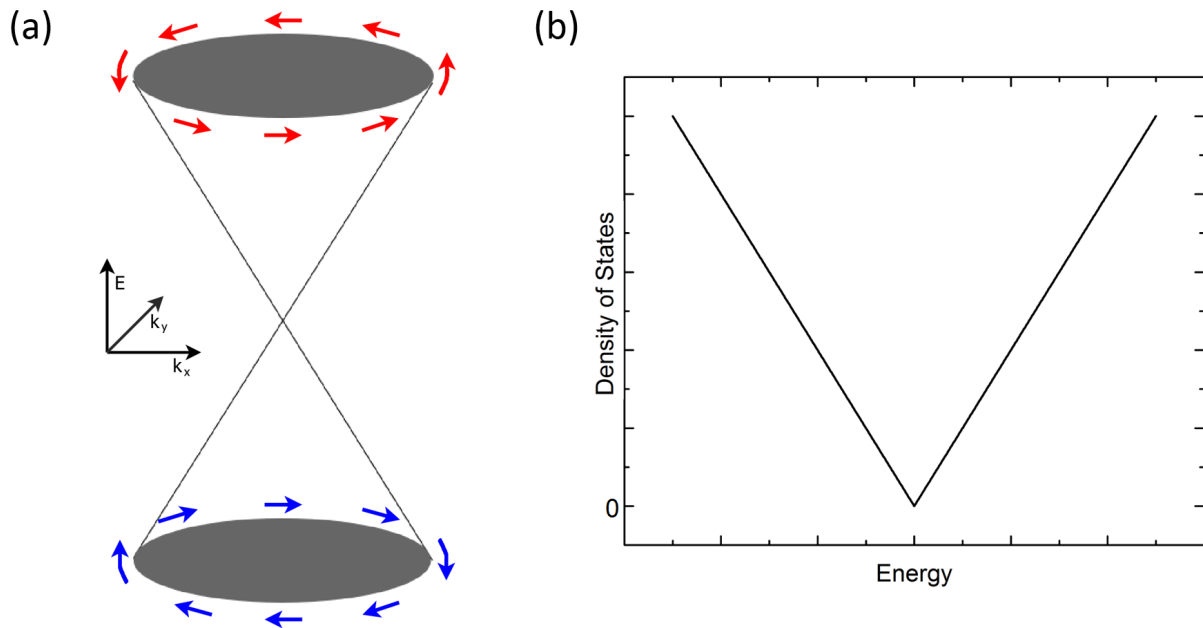


Figure 3.5: (a) Diagram of the Dirac cone with spin polarized conical sections in k -space. At energies above the crossing point of the Dirac cone, the electrons will be polarized in one direction when traveling around the cone, whereas at energies below the point, electrons will be polarized in the opposite direction. (b) Basic calculation demonstrating the expected behavior of the Dirac cone when looking at the density of states. To calculate the expected DOS curve, we need to integrate over the Fermi surface in two-dimensions. The resulting integral gives a linear dispersion relation in k , which yields a linear DOS versus energy curve. This is what we theoretically expect to see when taking scanning tunneling spectroscopy over a bare TI.

primary signature of topological surface states for the scope of scanning tunneling microscopy measurements.

3.2 Superconductivity

In 1908, Heike Kamerlingh Onnes successfully liquified helium, which would allow for the cooling of samples down to 4.2 K. Three years after this discovery, Onnes made another striking discovery. When measuring the electrical conductivity of mercury, he saw that the resistance of the metal went to zero. The temperature at which this happens is known as the critical temperature, T_C , and is an intrinsic property of the material. For many years,

no theory was developed to explain this very significant find, neither of the macroscopic nor microscopic scale. In 1935, the London brothers developed a phenomenological theory to help explain the behavior of electric and magnetic fields in a superconductor. More importantly for this dissertation, in 1957 Bardeen, Cooper, and Schrieffer (BCS) developed the cornerstone theory to explain superconductivity on a microscopic level, known, of course, as BCS theory. [1]

3.2.1 BCS Theory

A key idea of BCS theory is that some electrons in a superconductor cease to behave as single electrons and form into pairs known as Cooper pairs. While single electrons are forbidden from occupying the same quantum level due to the Pauli exclusion principle, Cooper pairs are not because they behave as bosons and can therefore all occupy a single quantum state. It is important to understand not only the behavior of these Cooper pairs in our materials, but also how they form.

Let us consider the model where two electrons are added to the Fermi sea at $T=0$ K. The electrons are allowed to interact only with each other. We can then write a two-particle wavefunction as

$$\psi_0(\mathbf{r}_1, \mathbf{r}_2) = \sum_{\mathbf{k}} g_{\mathbf{k}} e^{i\mathbf{k}\cdot\mathbf{r}_1} e^{-i\mathbf{k}\cdot\mathbf{r}_2} \quad (3.3)$$

where the two electrons have equal and opposite momentum \mathbf{k} due to the expectation that the lowest energy state of the two-particle system will have zero total momentum.[20] Since we expect an attractive potential between the two electrons and considering the antisymmetry

of the wave function with respect to particle exchange, we can rewrite the wave function as

$$\psi_0(\mathbf{r}_1 - \mathbf{r}_2) = \left[\sum_{\mathbf{k} > \mathbf{k}_F} \mathbf{g}_{\mathbf{k}} \cos(\mathbf{k} \cdot (\mathbf{r}_1 - \mathbf{r}_2)) \right] (\uparrow\downarrow - \downarrow\uparrow) \quad (3.4)$$

because the singlet state will have the lowest energy and the cosine term will give the highest probability for the electrons to be near one another. Plugging Eq. 3.4 into the Schroedinger equation, it can be shown that the energy eigenvalues and weighting coefficients $\mathbf{g}_{\mathbf{k}}$ can be solved for with

$$(E - 2\epsilon_{\mathbf{k}})\mathbf{g}_{\mathbf{k}} = \sum_{\mathbf{k}' > \mathbf{k}_F} V_{\mathbf{k}\mathbf{k}'}\mathbf{g}_{\mathbf{k}'} \quad (3.5)$$

where $\epsilon_{\mathbf{k}}$ are the plane wave energies and $V_{\mathbf{k}\mathbf{k}'}$ are the matrix elements of the interaction potential between the two electrons. In order for superconductivity to exist, the interaction potential must be negative or else there can be no bound state in which the electrons can form a Cooper pair.

This negative interaction potential stems from lattice vibrations in the material. Roughly speaking, as one electron moves through the lattice, it attracts multiple positive ions, which in turn attract another electron. The second electron pulled into the positive potential pairs with the initial electron, forming a Cooper pair, as shown in Fig. 3.6. In order to fully understand what is happening, we must investigate the formation of Cooper pairs and the effect that has on the Fermi sea, since when taking electronic measurements, that is what we are truly measuring.

Because the Fermi sea is comprised of so many particles, it is convenient to approach the formation of Cooper pairs using creation and annihilation operators. In this nomenclature, the operator $c_{\mathbf{k}\uparrow}^\dagger$ would create a spin up electron with momentum $\hbar\mathbf{k}$ and $c_{\mathbf{k}\uparrow}$ would annihilate

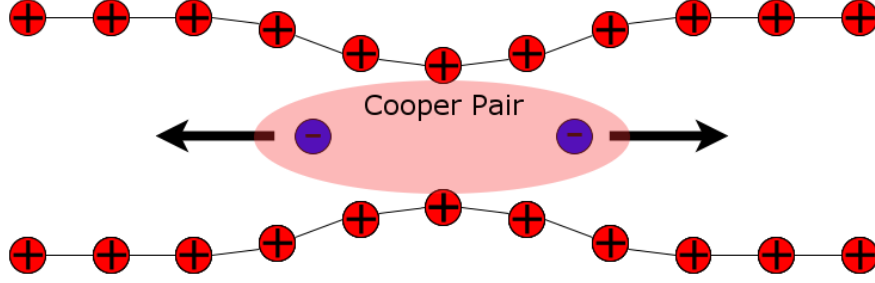


Figure 3.6: As the first electron moves to the right, it causes a distortion in the lattice, creating a region with higher positive charge. This region attracts a second electron into the newly formed potential well, and the two electrons become a pair known as a Cooper pair.

that same electron. Furthermore, a Cooper pair can then be represented by the term $c_{\mathbf{k}\uparrow}^\dagger c_{-\mathbf{k}\downarrow}^\dagger$ formed by a spin up electron with momentum $\hbar\mathbf{k}$ and a spin down electron with momentum $-\hbar\mathbf{k}$. Using this, we can proceed to the BCS ground state wave function, which is

$$|\Psi_G\rangle = \prod_{\mathbf{k}} (u_{\mathbf{k}} + v_{\mathbf{k}} c_{\mathbf{k}\uparrow}^\dagger c_{-\mathbf{k}\downarrow}^\dagger) |\psi_0\rangle \quad (3.6)$$

where $|\psi_0\rangle$ is the vacuum state of the Fermi sea and $|u_{\mathbf{k}}|^2 + |v_{\mathbf{k}}|^2 = 1$. The latter is defined such that $|v_{\mathbf{k}}|^2$ is the probability that the pair $(\mathbf{k}_\uparrow, -\mathbf{k}_\downarrow)$ is occupied while $|u_{\mathbf{k}}|^2 = 1 - |v_{\mathbf{k}}|^2$ is the probability that it is not occupied.

Having defined this nomenclature, we can now introduce the most notable characteristic of superconductors in this dissertation; the superconducting pair potential $\Delta_{\mathbf{k}}$. BCS theory demonstrates that there is a reduction of energy with respect to the Fermi sea ground state caused by the condensation of Cooper pairs. In turn, the spectrum of single-electron states, also called quasiparticles, is given by

$$E_{\mathbf{k}} = \sqrt{\Delta_{\mathbf{k}}^2 + \xi_{\mathbf{k}}^2} \quad (3.7)$$

where $\xi_{\mathbf{k}} = (\hbar^2 \mathbf{k}^2 / 2m) - E_F$. Here, the superconducting pairing potential $\Delta_{\mathbf{k}}$ is defined as

$$\Delta_{\mathbf{k}} = - \sum_{\mathbf{k}'} V_{\mathbf{k}\mathbf{k}'} u_{\mathbf{k}'} v_{\mathbf{k}'} \quad (3.8)$$

where $V_{\mathbf{k}\mathbf{k}'}$ is once again the matrix element of the interaction potential. Eq. 3.8 is known as the self consistency equation and emphasizes the fact that the pairing potential stems from the quasi-particle electrons and holes.[20]

Finally, we can define a few more relevant equations for this dissertation. Considering that STM measures the quasi-particle density of states, it would be most convenient to see the expected form of the density of states in terms of $\Delta_{\mathbf{k}}$. In the simplest scenario, we can investigate the form for the density of states where the superconductor is near 0 K, or $T \ll T_C$, is not in a magnetic field, and is homogeneous throughout. $\Delta_{\mathbf{k}}$ can then be defined as a positive, real constant which we will define as the bulk energy gap Δ_0 . We can then write the BCS density of states as

$$\frac{N_{BCS}}{N_0} = \begin{cases} \frac{E}{\sqrt{E^2 - \Delta_0^2}} & \text{when } E > \Delta_0 \\ 0 & \text{when } E < \Delta_0 \end{cases} \quad (3.9)$$

At very low temperature we can expect the density of states to look like Fig. 3.7. The width of the superconducting gap is $2\Delta_0$ and the sharp cusps on both sides of the gap are known as coherence peaks, which are found at the energies where the Cooper pairs begin breaking into separate quasi-particles once again. The coherence length, or length scale of a Cooper

pair, can be defined in terms of Δ_0 in the equation

$$\xi_0 = \frac{\hbar v_F}{\pi \Delta_0} \quad (3.10)$$

where v_F is the Fermi velocity of the superconducting material. We can also relate the superconducting transition temperature T_C to the energy gap with the equations $\Delta_0 = 1.76 k_B T_C$ in the weak coupling limit.[20, 21]

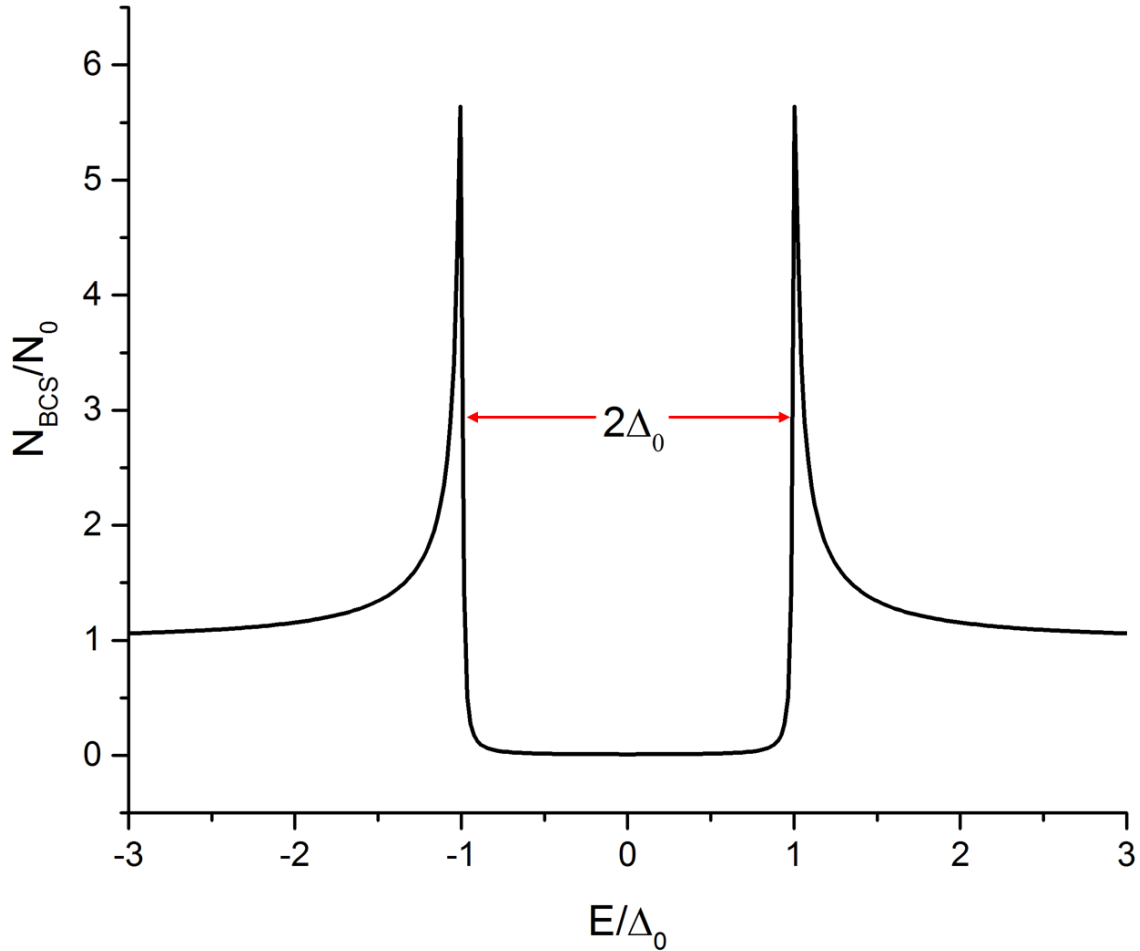


Figure 3.7: A calculated superconducting energy gap demonstrating what the expected density of states would look like on a BCS superconductor. The width of the gap is $2\Delta_0$. A small amount of thermal broadening was applied in the calculation to prevent the coherence peaks from going to infinity.

3.2.2 P-Wave Superconductors

While Sec. 3.2.1 gives a solid understanding of the causes of superconductivity, it is not quite enough to explain all of the forms of superconductivity. Many superconductors are known as “s-wave” for which the Cooper pairs are assembled from electrons with anti-parallel spin, also known as the spin singlet state. The spin states of the Cooper pairs can be expressed as

$$\text{Singlet} = |\uparrow\downarrow\rangle - |\downarrow\uparrow\rangle \quad \text{Triplet} = \begin{cases} |\uparrow\uparrow\rangle \\ |\uparrow\downarrow\rangle + |\downarrow\uparrow\rangle \\ |\downarrow\downarrow\rangle \end{cases} \quad (3.11)$$

The s-wave superconductors also feature a pairing potential Δ_0 that is independent of momentum and is spherically symmetric, much like the s-orbital of an electron in an atom. As our understanding of superconductivity continues to grow, we continue to find more exotic superconductors that have differing pairing symmetries. The most relevant form of exotic superconductivity for this dissertation is p-wave superconductivity, which is predicted to be induced in the topological surface state of a topological insulator when it is put in contact with a s-wave superconductor, due to the spin polarization of the topological surface state itself.

In order to further discuss p-wave superconductivity, let us first discuss the spherical harmonic Y_l^m that relates directly to the form of the pairing potential $\Delta(\mathbf{k})$. For the spin triplet superconductivity, we should investigate the spherical harmonics $Y_1^{\pm 1}$ and Y_1^0 . Condensing these spherical harmonics down to the x-y plane, as the topological surface state is itself two-dimensional, we see that the pairing potential takes the form of a clover leaf in

plane, as shown in Fig. 3.8(a). This demonstrates that the pairing symmetry is not uniform for all directions in \mathbf{k} -space and is zero for certain values of \mathbf{k} . This will result in the density of states not being fully gapped like that of an s-wave superconductor, as shown in Fig. 3.8(b).

The mechanism behind the induced p-wave pairing can be explicitly seen by looking at the Hamiltonian of a topological insulator with s-wave (spin singlet) superconducting pairing, denoted by the equation

$$H = H_{\text{3D TI}} + H_{\text{s-wave}} \quad (3.12)$$

where

$$H_{\text{3D TI}} = \int d^2\mathbf{r} \psi^\dagger [-iv(\partial_x \sigma^y - \partial_y \sigma^x) - \mu] \psi. \quad (3.13)$$

Equation 3.13 gives us the band energies $\epsilon_\pm(k) = \pm v|\mathbf{k}| - \mu$, which describes the upper and lower branches of the Dirac cone. By definition, $H_{\text{s-wave}} = \int d^2r \Delta(\psi_\uparrow \psi_\downarrow + h.c.)$ describes the singlet superconductivity discussed in Sec. 3.2.1, and results in a fully gapped quasiparticle system given by $E_\pm = \sqrt{\epsilon_\pm(k)^2 + \Delta^2}$. By performing a unitary transformation that diagonalizes the kinetic energy in H , we can then write this Hamiltonian in terms of the creation operators, ψ_\pm^\dagger , which create electrons in the positive and negative energy regions of the Dirac cone. This results in the expression

$$H = \sum_{s=\pm} \int \frac{d^2\mathbf{k}}{(2\pi)^2} \left\{ \epsilon_s(\mathbf{k}) \psi_s^\dagger(\mathbf{k}) \psi_s(\mathbf{k}) + \left[\frac{\Delta}{2} \left(\frac{\mathbf{k}_x + i\mathbf{k}_y}{|\mathbf{k}|} \right) \psi_s(\mathbf{k}) \psi_s(-\mathbf{k}) + \text{h.c.} \right] \right\} \quad (3.14)$$

where we can see that the induced superconductivity in the TSS produces a form of $p_x + ip_y$ superconductivity. [22, 23, 24] This can be qualitatively understood by the fact that the induced superconductivity pairs electrons with opposite momenta \mathbf{k} and $-\mathbf{k}$ because they

carry opposite spins as imposed by the spin orbit coupling of the TSS. The Cooper pair also picks up an angular momentum because the electron spin rotates by 2π when encircling the Dirac cone, and thus we have TR-invariant $p_x + ip_y$ superconductivity. [22] This specific form of superconductivity is predicted to harbor Majorana fermions, which are quasiparticles that are their own antiparticles. It can be shown that by applying a magnetic field normal to the surface, the Cooper pairs will be bound to a vortex, breaking TR-symmetry and allowing for the existence of chiral Majorana bound states. [23, 24, 25]

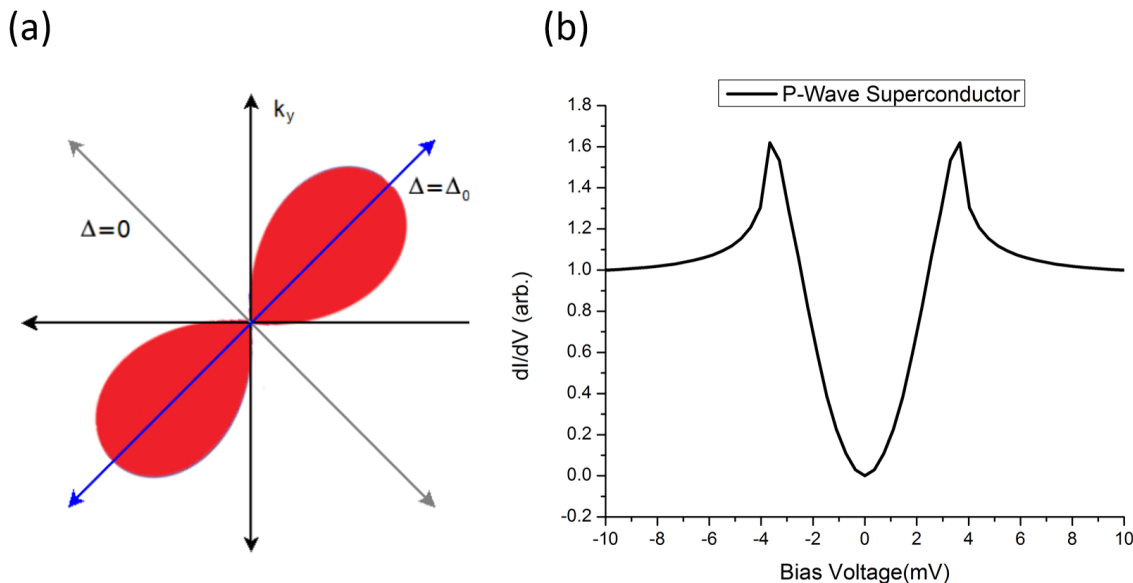


Figure 3.8: (a) A plot of the superconducting pairing potential $\Delta(\mathbf{k})$ for a p-wave pairing symmetry in the $k_x - k_y$ plane. (b) The density of states of a pure p-wave superconductor. The DOS is not fully gapped like in the s-wave case, which results in a “v” shape inside of the superconducting gap.

3.2.3 Superconducting Proximity Effect

The final theory from superconductivity that we must understand for this dissertation is the effect that a superconductor has on a normal metal when placed in direct contact. As mentioned in Sec. 3.2.2, an s-wave superconductor placed in contact with a TI will induce

p-wave superconductivity in the topological surface state. The goal of this section is not to discuss the complex physics behind that phenomenon, but to introduce the basic mechanics that drive induced superconductivity. This can be done by utilizing the Bogoliobov-de Gennes (BdG) equations.

Remembering the discussion from Sec 3.2.1, the superconducting pairing potential $\Delta_{\mathbf{k}}$ arises from the quasiparticle excitations $u_{\mathbf{k}}$ and $v_{\mathbf{k}}$ from the Fermi sea. In the case of induced superconductivity, we can translate these functions from momentum space to position space due to the spacial dependence on the superconducting pairing potential Δ , which we now define as $\Delta(\mathbf{r})$. We can also redefine $u_{\mathbf{k}}$ and $v_{\mathbf{k}}$ as $u(\mathbf{r})$ and $v(\mathbf{r})$, which are the wavefunctions for electrons and holes respectively. The BdG equations are two coupled Schroedinger equations written as

$$\mathcal{E}u(\mathbf{r}) = \mathcal{H}_0 u(\mathbf{r}) + \Delta(\mathbf{r})v(\mathbf{r}) \quad (3.15)$$

$$\mathcal{E}v(\mathbf{r}) = -\mathcal{H}_0^* v(\mathbf{r}) + \Delta^*(\mathbf{r})u(\mathbf{r})$$

where \mathcal{E} is the energy eigenvalue and \mathcal{H}_0 is the Hamiltonian for the Fermi sea in the absence of the pairing potential with respect to E_F . [21, 26] Referencing once again back to Sec. 3.2.1, we have an analog to the self consistency equation 3.8 in position space

$$\Delta(\mathbf{r}) = \mathbf{g}(\mathbf{r}) \sum_{\mathbf{n}} \mathbf{v}_{\mathbf{n}}^*(\mathbf{r}) \mathbf{u}_{\mathbf{n}}(\mathbf{r}) (1 - 2\mathbf{f}(\mathcal{E}_{\mathbf{n}})) \equiv \mathbf{g}(\mathbf{r}) \mathbf{F}(\mathbf{r}) \quad (3.16)$$

where $g(\mathbf{r})$ is the interaction parameter and $F(\mathbf{r})$ is the Cooper pair condensate amplitude.

From here it is directly evident that $\Delta(\mathbf{r})$ is constrained by these two functions. With the superconductor/normal metal interface, it is important to note the behaviors of $g(\mathbf{r})$ and $F(\mathbf{r})$. Because $F(\mathbf{r})$ is the measure of the local Cooper pair density, it must smoothly

transition from the superconducting region into the normal metal region, of course becoming weaker as the Cooper pairs move further from the superconductor. This smooth transition results in a weakening of superconductivity in the superconductor near the interface. $F(\mathbf{r})$ contains two important length scales; ξ_S , which is the superconducting coherence length mentioned in Sec. 3.2.1, and ξ_N , which is the coherence length of the Cooper pairs in the normal metal. The interaction parameter $g(\mathbf{r})$ behaves somewhat discontinuously at the interface however. There is still some small scale electron screening at the interface, so $g(\mathbf{r})$ does not quite behave like a perfect step function, but for the purposes of this discussion we will treat it as such. Fig. 3.9 demonstrates the behavior of $\Delta(\mathbf{r})$ as a function of the pair correlation amplitude $F(\mathbf{r})$ and the interaction parameter $g(\mathbf{r})$ across the S/N interface. In the superconductor, $g(\mathbf{r}) = \mathbf{1}$ as the pairing potential is at its maximum of Δ_0 . In the normal metal however, $g(\mathbf{r}) \ll \mathbf{1}$ typically, allowing for induced superconductivity to exist in the normal metal. It is important to note that the calculated fits for the superconducting gaps presented in Sec. 4 of this dissertation were done by solving the BdG equations to get the density of states $N(E)$ using the method proposed by Gallagher. [27]

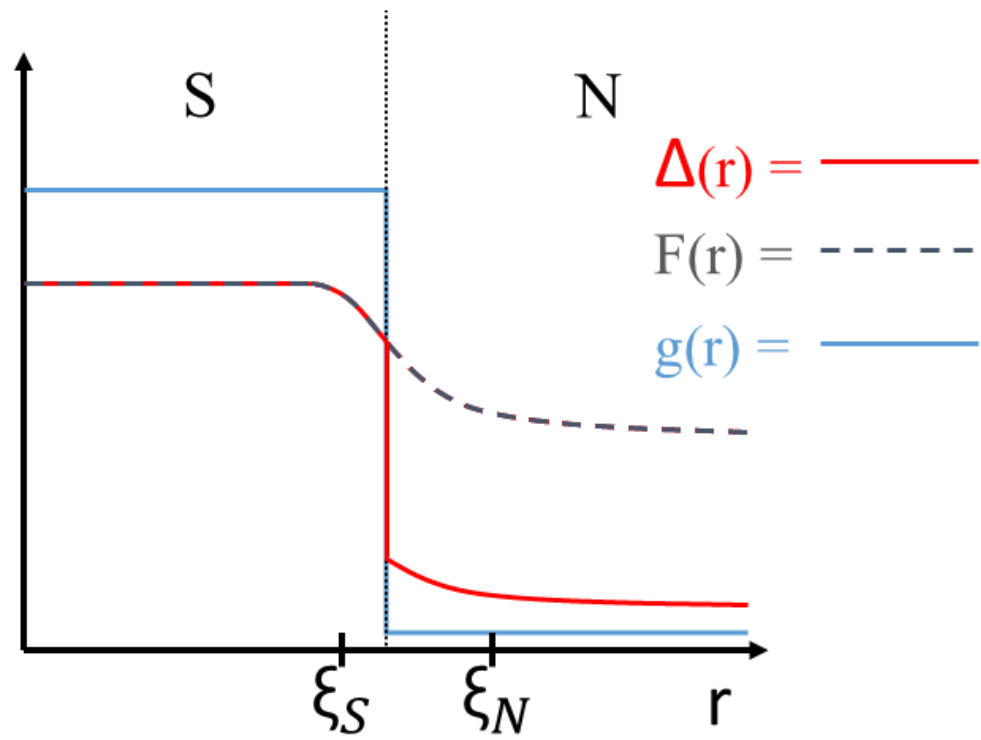


Figure 3.9: An image demonstrating the behavior of $\Delta(\mathbf{r})$ as a function of the pair correlation amplitude $F(\mathbf{r})$ and the interaction parameter $g(\mathbf{r})$.

Chapter 4

Probing Superconductor/TI Interfaces

4.1 Superconducting Proximity Effect of PbBi on Bi₂Se₃

4.1.1 Motivation

The initial objective of this experiment was to solely measure the superconducting coherence length induced in Bi₂Se₃ by proximity to an s-wave superconductor. This specific form of induced superconductivity is theoretically predicted to produce two-dimensional, TR-invariant p-wave superconductivity in the topological surface states. This form of p-wave superconductivity can harbor Majorana bound states, which have many interesting characteristics. A possible final goal was to detect a Majorana fermion in an “anti-dot” geometry, as shown in Fig. 4.1. Measuring the coherence length represents an important first step towards this proposed experiment.

As the measurement proceeded, we not only extracted the superconducting coherence length, but also observed two unexpected features in the LDOS: the oscillatory behavior in the LDOS outside of the superconducting gap near the S/TI interfaces and the inverse proximity effect of the TSS on the superconducting islands. It was with these observations that the focus of this work changed from trying to detect Majorana bound states to trying to fully understand the characteristics of these unexpected behaviors in these topological

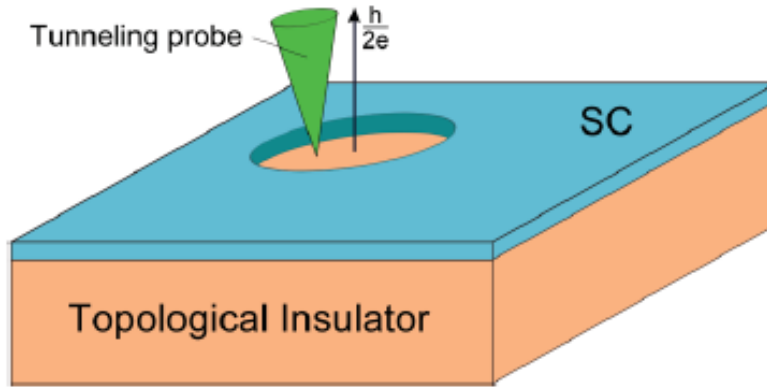


Figure 4.1: Proposed anti-dot geometry where a continuous superconducting film is deposited on the surface of a TI with anti-dots spaced evenly throughout the film, which would go all the way to the TI surface. By applying a magnetic field normal to the S/TI surface, Majorana bound states are theoretically predicted to form around the boundary of the anti-dot, which could be probed using STS. Figure adapted from the Hasan and Kane colloquium on topological insulators. [16]

insulator/superconductor systems. In collaboration with Dr. Levchenko and Dr. Sedlmayr, we were able to successfully model and describe these surprising behaviors. However, at this stage we are unable to conclusively decipher the specific superconducting pairing symmetry of the system.

To reiterate, the simplest theories predict that the induced superconductivity in the TSS should follow p-wave symmetry. In reality, the induced superconductivity is likely much more complicated. As the bulk of the topological insulator is not perfectly insulating (as will be discussed in Sec. 4.1.3), there will likely be conducting states which will also have induced superconducting states that do not obey the predicted p-wave behavior.[18] Similarly, angular-resolved photoemission spectroscopy (ARPES) measurements demonstrate the presence of trivial surface states caused by band bending in these materials. [28] Since STS is a local measurement and is sensitive to all of these effects, the LDOS measurements presented in this chapter are likely a combination of both s-wave and p-wave forms of induced

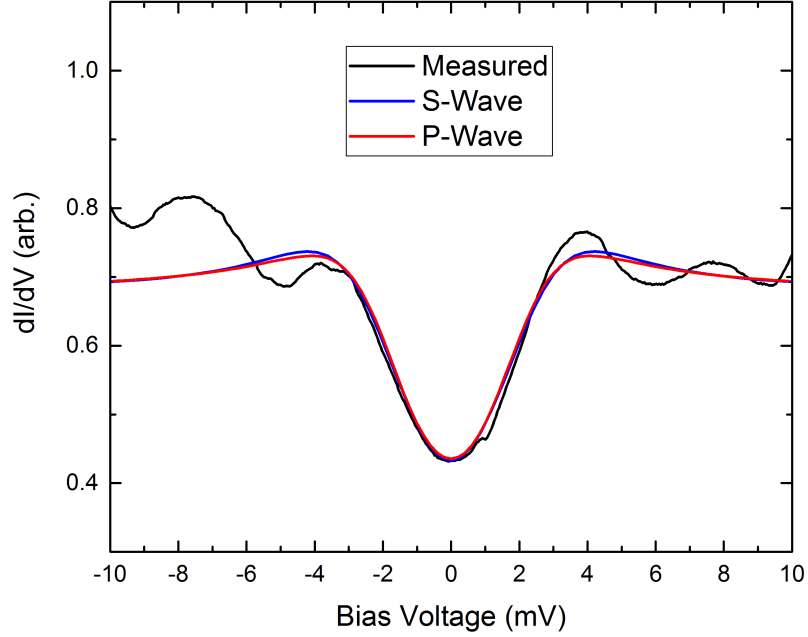


Figure 4.2: LDOS taken 40 nm from a superconducting island at 4.2 K with s-wave and p-wave DOS calculated curves. At this temperature, it is difficult to see much difference between the two calculated curves as broadening effects cause them to appear very similar. Fitting parameters are shown later in Table 4.0a.

superconductivity.

In an attempt to clarify what kind of induced superconductivity we were measuring, we fit the LDOS measurements with both s-wave and p-wave DOS calculations. An example of these attempted fits is shown in Fig. 4.2. In general, we find that it is difficult at 4.2 K to differentiate between the s-wave and p-wave DOS curves, as shown in the next section; we conclude that at present we cannot discern the superconducting pairing symmetry induced into the Bi_2Se_3 .

4.1.2 Introduction

Three-dimensional topological insulators (TI) [6], most notably Bi_2Se_3 , Bi_2Te_3 or $\text{Bi}_{1-x}\text{Sb}_x$, were once known primarily for their tendency to be great thermoelectric materials. In recent years, a more interesting characteristic of these materials was discovered; their ability to harbor a topologically protected electronic surface state. [29, 30, 31]. It is now understood that these topological surface states (TSS) stem from a combination of strong spin-orbit coupling and time reversal symmetry intrinsic to these materials. By studying the interplay of these symmetry-protected states with symmetry-breaking interfaces, such as magnetic or superconducting materials, we may be able to observe a plethora of new effects and provide new platforms for potential technological advances. A very direct approach to achieve this goal is to study a set of phenomena associated with the superconducting proximity effect in these exotic materials.

It has been predicted that when a topological insulator is brought into contact with a conventional *s*-wave superconductor (SC), the superconducting proximity effect induces superconducting correlations into the TSS that have unconventional *p*-wave symmetry, discussed earlier in 3.2.2 [32, 22]. This original result triggered a flood of further theoretical works, some representative examples include Refs. [33, 34, 35, 36, 37, 38], and a multitude of experimental efforts. The latter covers many various techniques, spanning from angle-resolved photoemission spectroscopy, scanning tunneling microscopy, point contact, and differential conductance measurements [39, 40, 41, 42, 43], to observations of supercurrents and unusual Josephson Fraunhofer patterns [44, 45, 46, 47, 48, 49, 50, 51, 52]; experiments on phase coherent transport including multiple Andreev reflections, Fabry-Perot interferometry and Aharonov-Bohm oscillations [53, 54, 55, 56].

On the technical side, proximity effects can be realized by growing thin layers of SC-TI heterostructures, an approach employed by most of the existing experiments. One could also study induced superconductivity in the TSS from the TI's bulk which becomes superconducting when Cu is intercalated into Bi_2Se_3 [57, 58]. While $\text{Cu}_x\text{Bi}_2\text{Se}_3$ retains the Dirac surface state, its superconducting volume fraction is relatively low which causes obvious challenges. Here we explore a complimentary but different route by inducing superconductivity into TSS locally by depositing a matrix of superconducting PbBi islands on the surface of Bi_2Se_3 . This approach was theorized earlier as a path to creating superconducting graphene [59]. It was also employed experimentally to create a tunable realization of two-dimensional superconductivity in mesoscopic superconductor-normal-superconductor (SNS) arrays [60].

Through the use of cryogenic scanning tunneling microscopy (STM), an experimental technique that is ideal for probing the superconducting proximity effect in inhomogeneous samples, we are able to measure the induced local electronic density of states in TI surface states, as discussed in 2.1.2. A schematic illustration of the experiment is shown in Fig. 4.3(b), where an STM probe is placed near the interface of a superconducting island and a TI, and spectra are taken while gradually moving the probe away from the island along the TI surface.

In this section, we present the observation of two main experimental results. First, the STM spectra reveal a clear superconducting gap induced into the TSS which decays as we move away from the superconducting island. From the spatially resolved probes and fits of the gap function, we estimate the superconducting coherence length to be of the order of ~ 540 nm along the direction parallel to the quintuple layers. In addition, at energies above the gap we observe oscillatory behavior of the density of states that resembles the Tomasch interference effect [63]. Second, while all the existing efforts were concentrated on revealing signatures of superconductivity induced into the TSS, much less attention was paid

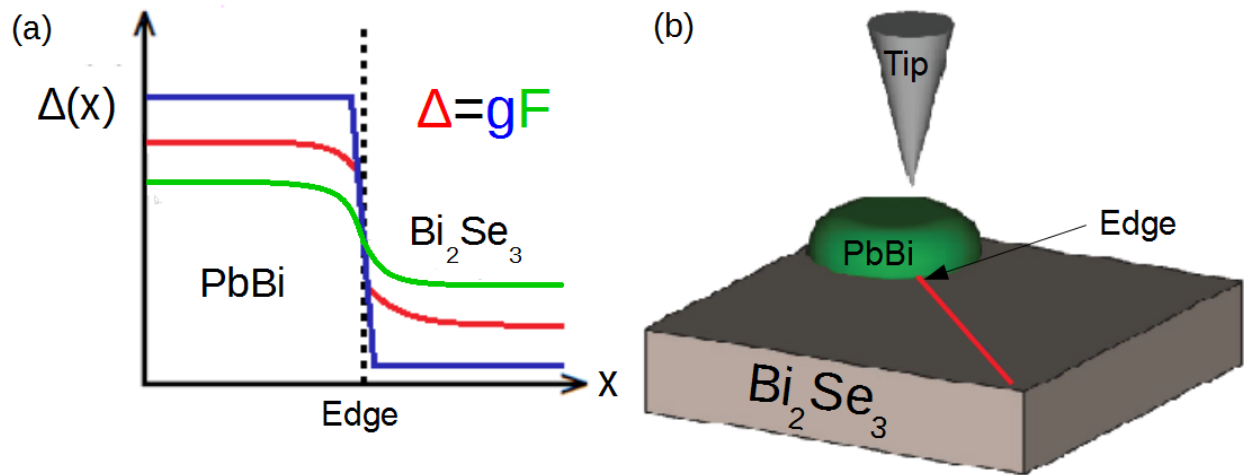


Figure 4.3: (a) A schematic of the standard proximity effect picture showing the induced superconducting energy gap [61], Δ , at an interface as a function of position x , where F is the superconducting condensate amplitude. The pairing interaction constant, g , is generally taken to have the form of a clear step function, but at small scales, the step actually has a finite slope due to electronic screening [62]. (b) A schematic illustration for the geometry of the STM probe scanning over the surface of TI Bi_2Se_3 in proximity to a PbBi island. In this experiment, we are interested in measuring the superconducting coherence length in the plane parallel to the TI surface, not in the normal direction to the surface as done in many other experiments.

to the corresponding inverse effect of the TSS on an adjacent superconductor. This intriguing question is addressed by taking careful STM density of states spectra on superconducting islands and uncovering traces of the Dirac cone that seemingly leaks from the TSS into the superconductor. This observation manifestly provides evidence for the possibility of an inverse topological proximity effect.

4.1.3 Experiment

The TI used in this experiment is bismuth doped $\text{Bi}_{2.04}\text{Se}_{2.96}$, grown by slowly cooling a stoichiometric mixture of Bi and Se from a temperature of 850 °C. Five atomic planes with atomic order Se1-Bi1-Se2-Bi1-Se1 form a quintuple layer (QL); the QLs are weakly bound to each other by the van der Waals force, making it possible to readily expose a pristine surface for study. The exposed QL supports the existence of the TSS, which features a single Dirac cone. While Bi_2Se_3 is typically *n* type, the bulk doping of Bi tends to shift the Fermi level back to the center of the band gap [18]. More recent measurements in the Tessmer lab demonstrate that the shift of the Dirac cone may stem more from the cleaving environment of the sample than from the doping levels.

$\text{Pb}_{0.3}\text{Bi}_{0.7}$ is used as the superconductor due to its favorable whetting properties on Bi_2Se_3 , its large gap width (3.65 meV), and its high transition temperature of 8.2 K [64]. Initial measurements using pure Pb as the superconductor are shown in Appendix A. Control measurements of the $\text{Pb}_{0.3}\text{Bi}_{0.7}$ film are shown in Fig. 4.4, where we measure the expected superconducting DOS on a thick film of $\text{Pb}_{0.3}\text{Bi}_{0.7}$ and measure a very reasonable transition temperature of 8.3 K using a four-probe measurement conducted by Dr. Reza Loloee. Further characterization measurements done with EDS were taken on our PbBi films which demonstrated that after thermal evaporation, the resulting alloy was 36 % Pb and 64%

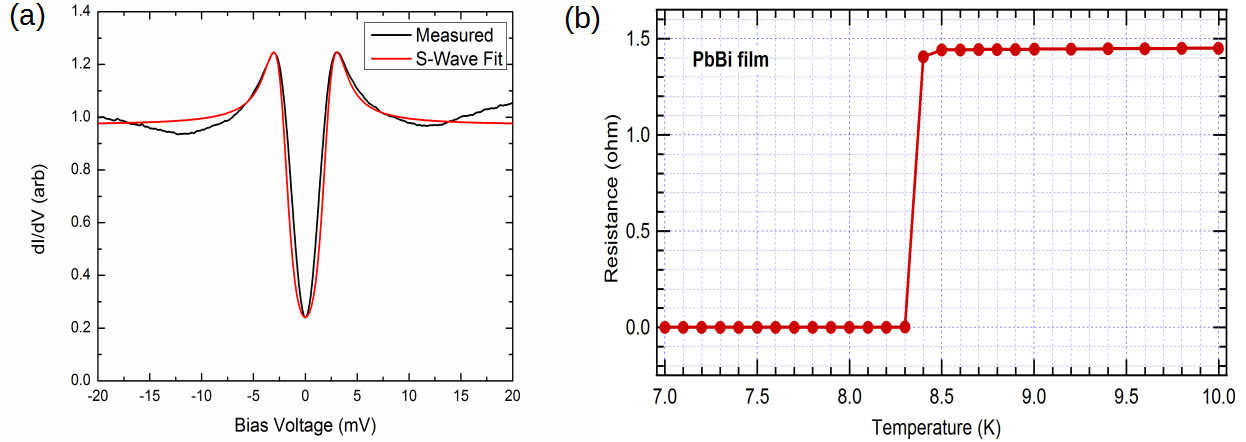


Figure 4.4: (a) STS taken on a 250 nm thick film of $\text{Pb}_{0.3}\text{Bi}_{0.7}$ deposited on Bi_2Se_3 and fit with a calculated s-wave DOS that has been appropriately broadened to account for thermal and scattering effects. (b) Four-probe measurement taken on a 400 nm thick film of $\text{Pb}_{0.3}\text{Bi}_{0.7}$ taken by Dr. Reza Loloee. The transition temperature of 8.3 K closely matches the nominal value of 8.2 K. [64] Both measurements taken at 4.2 K.

Bismuth, which when accounting for the uncertainties of the measurement method ($\pm 3\%$ from control data) as well as the differing evaporation temperature of Pb and Bi, demonstrates that our superconducting alloy is well within the expected ratio at the surface. An example of the EDS measurements taken on our thick control sample is shown in Fig. 4.5.

The TI is first cleaved in a nitrogen environment, where a TEM mask is fastened to the TI surface. The sample is then placed into a thermal evaporator that is also purged in nitrogen gas. Here, we deposit 10 nm of $\text{Pb}_{0.3}\text{Bi}_{0.7}$ onto the surface of the TI by evaporation through the TEM mask. This results in large array of superconducting islands with a diameter of $1.2 \mu\text{m}$, as shown in Fig. 4.6. From there, the sample is moved to our cryogenic Besocke design STM system for measurement, where the system is first pumped down to high vacuum and cooled to 4.2 K. It should be noted that all of the preparatory steps are done in either a nitrogen or vacuum environment in order to minimize air exposure and ensure that the sample surface remains clean. All STM topographs are taken with a bias voltage of 5 V and tunneling current of 500 pA, and all spectra are taken with a voltage divider placed on the

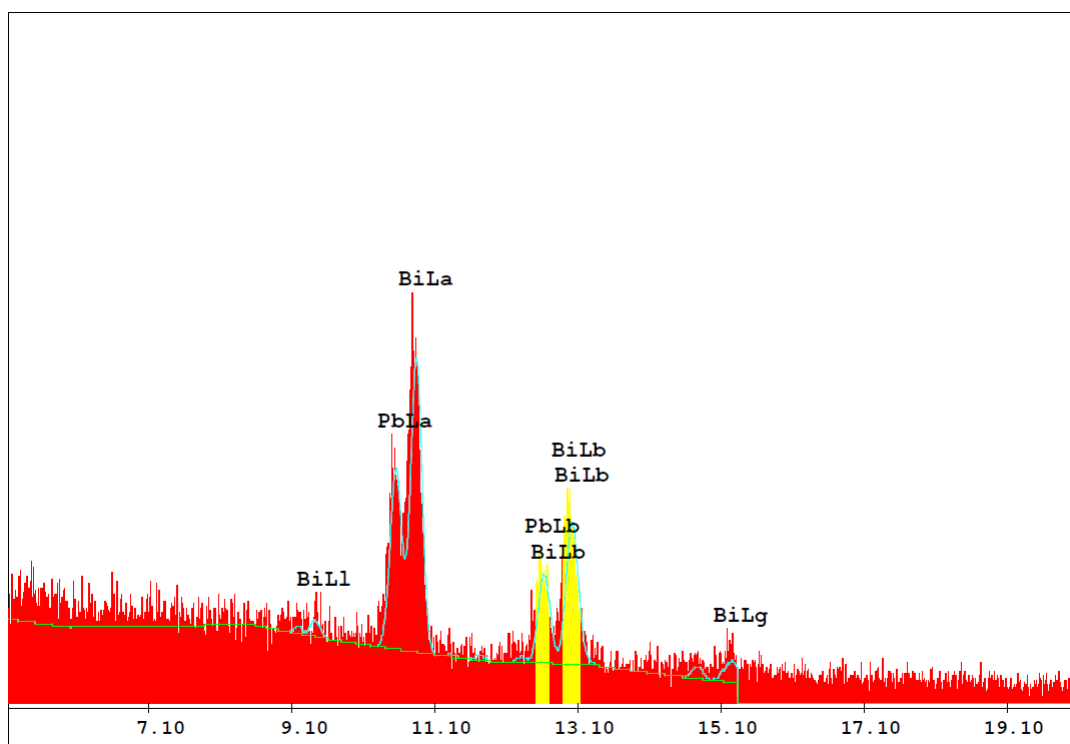


Figure 4.5: EDS measurements taken on our 250 nm thick PbBi film showing the actual atomic composition of our alloy. EDS showed that the actual film composition was 36% Pb and 64% Bi, which is well within the expected composition range for our superconducting islands.

bias voltage lead (to improve energy resolution) over a range of -45 meV to 45 meV and measured via a lock-in amplifier.

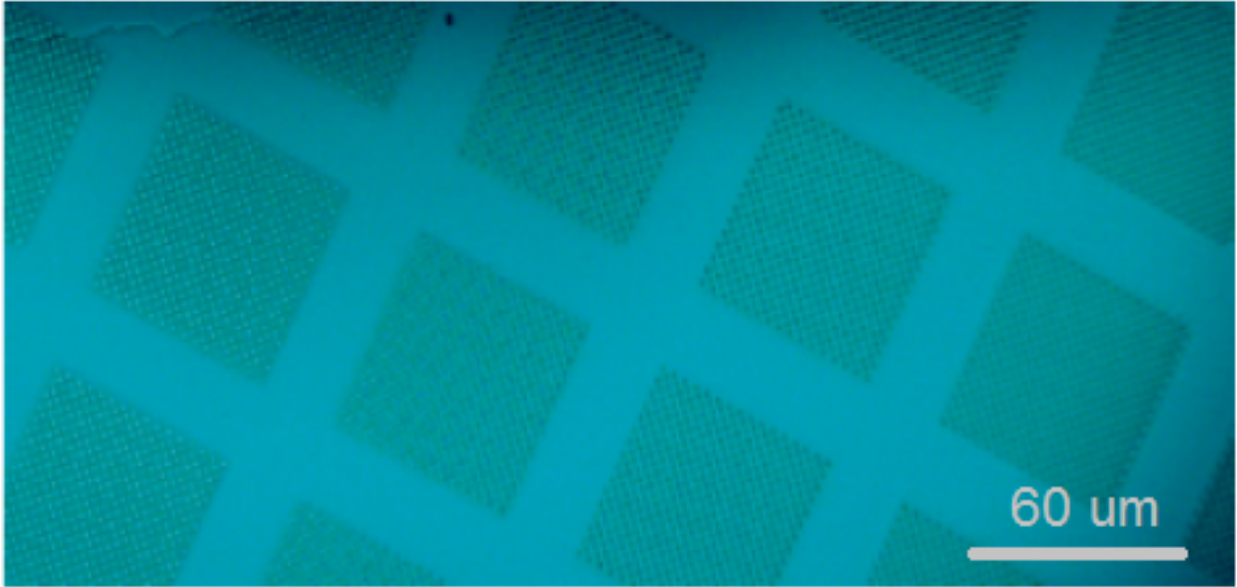


Figure 4.6: Image taken under optical microscope showing the superconducting array pattern after thermal evaporation. This sample was exposed to air and was therefore not measured under STM.

When doing a surface probe measurement, it is important to fully characterize the surface being measured. In this case, we are interested in the quality of deposition of the PbBi islands as well as how clean the interface is between the island edge and the TI surface. In Fig. 4.7, we show various atomic force microscopy (AFM) and STM topographs demonstrating the structure of these islands after thermal evaporation. The PbBi dots appear to be comprised of many 20-100 nm radius droplets grown on top of and around one another. This can clearly be seen in Fig. 4.7(a) and (b). Fig. 4.7(c) is an STM topograph showing the edge of one of such droplet formations, along with the respective height profile in Fig. 4.7(d). Here we can see that the interface between the PbBi and the TI surface is very abrupt, giving evidence of minimal leakage of the PbBi onto the TI surface. We should also note that the TI surface is very smooth, giving evidence that there was minimal air exposure or contamination of our

surface.

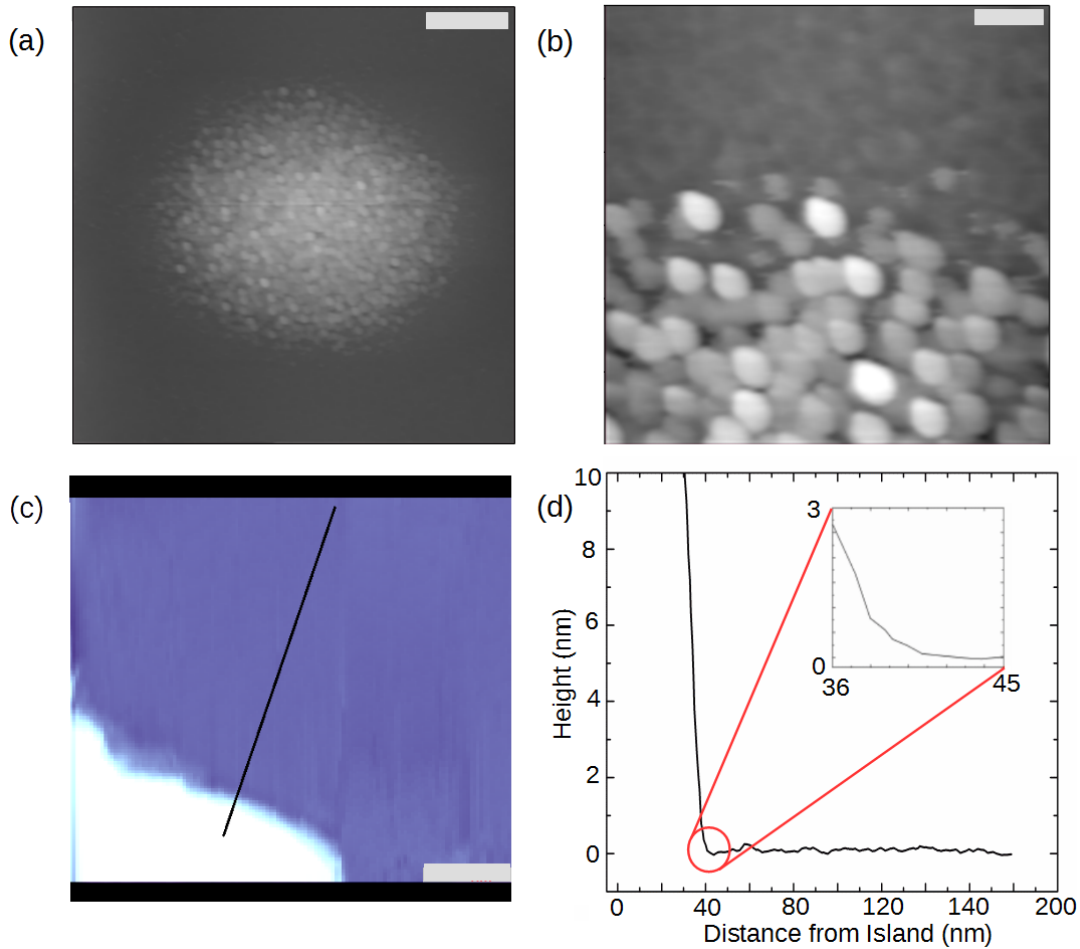


Figure 4.7: (a) and (b) Atomic force microscopy (AFM) topographs of a thermally deposited PbBi dot. We can clearly see a very grainy appearance to the overall dot, but upon closer inspection it is clear that the dot is comprised of many small superconducting droplets. (c) STM topograph of a PbBi droplet with its respective height profile trace shown in (d). The radius of curvature at the base of the droplet is an artifact due to the radius of the STM tip. The actual interface between the droplet and the TI is very sharp, which is ideal for our measurement. Scale bars: (a) 500 nm (b) 100 nm (c) 40 nm.

We present the local density of states (LDOS) measurements taken via cryogenic STM at a temperature of 4.2 K in Fig. 4.8. The left panel shows a series of differential conductance plots reflecting the LDOS of the TSS taken at various distances away from the superconducting island. At a distance of approximately 40 nm, the induced superconducting gap is roughly 20% smaller than the corresponding gap on an island, while at distance of order 200 nm the

gap falls to almost half of its value. At a distance of $> 5 \mu\text{m}$, the Dirac cone is the only dominating feature in the LDOS since the local region of the TI is no longer within the range of the superconducting proximity effect. The Dirac cone is not perfectly sharp as there is still a small amount of thermal energy at 4.2 K, which broadens the point of the cone. Again, it should be noted that the Dirac cone is “raised” and cannot go to 0 due to the ever present contribution of the bulk states from the TI. [18]

As mentioned in Sec. 4.1.1, the induced superconductivity is likely a combination of s-wave and the predicted p-wave pairing symmetries, but at 4.2 K we are unable to differentiate between the two. Fig. 4.9 shows the induced superconducting gap width Δ as a function of distance from the PbBi droplet. We fit the data with an exponential decay to extract a coherence length of $\sim 540 \pm 200 \text{ nm}$. The gap width is extracted from the raw data by taking linear extrapolations of the dI/dV curves around of the superconducting gap and subtracting the extrapolated lines from the full data. This enhances the coherence peaks on both sides of the Fermi level and allows us to extract the value of Δ . As a check, we also applied s-wave BCS curve (see Fig. 3.7) and approximate p-wave curve (see Fig. 3.8(b)) fits to the data; the best fits gave reasonable agreement with the linear extrapolation method. The fitting parameters for the s-wave and p-wave calculations are shown in Table 4.0a below. The p-wave DOS fits required less broadening than the s-wave fits, and as such, we interpreted these fits to be better than the conventional s-wave fits. We compare the calculated and extracted values of Δ in Table 4.0b below. That being said, these calculations do not conclusively demonstrate the specific pairing symmetry induced in the surface states of the topological insulator; rather, this serves to demonstrate how difficult it is to extract the specific pairing symmetries from LDOS measurements at 4.2 K. By cooling the sample to lower temperatures (such as 300 mK), it may be possible to gain a better understanding of these effects.

	On Island (s-wave)	40 nm (p-wave)	40 nm (s-wave)	160 nm (p-wave)	160 nm (s-wave)
Δ (meV)	4.0	3.0	2.1	1.9	1.3
Γ (meV)	1.30	0.75	1.60	1.40	1.42
L (nm)	795.32	1,378.56	646.19	738.51	728.11

Table 4.0a: Table presenting the calculated values of Δ and other fitting parameters for the best fit DOS curves at various distances from the superconducting island. The algorithm utilized both thermal and energetic smearing. Here Γ is the characteristic energy smearing of the material and L is the related mean free path, and the two values are related by the equation $L = hv_f/2\Gamma$. All calculations were done using a temperature of 4.2 K. The p-wave calculations were done via a sum of separate s-wave superconducting curves weighed accordingly by a p-wave orbital function.

	Best Fit Δ (meV)	Extracted Δ (meV)	Difference (meV)
On Island	4.0	4.0	0.00
40 nm	3.0	3.25	0.25
160 nm	1.9	2.55	0.65

Table 4.0b: A comparison of the gap widths taken from the best fit DOS curves with the widths extracted using our linear-subtraction method.

We also observed oscillatory behavior in the LDOS near the S/TI interface. On the data set taken at 40 nm away from the island one sees oscillatory features occurring with the period of roughly 5 mV. Interestingly, similar features are present on the LDOS plots taken on the different islands, which are shown on the right panel of Fig. 4.8. While pure Pb is known for having phonon modes outside of the superconducting gap, it should be noted that the specific PbBi alloy that we use does not exhibit this same behavior. [64] Furthermore, in addition to oscillations at energies above the gap, traces of the Dirac cone are also revealed. We attribute this phenomenon to the inverse topological proximity effect where LDOS properties of topological surface states penetrate into the superconducting island. In what follows, this behavior is illustrated using an elegant theoretical model developed by Dr. Alex Levchenko and Dr. Nicholas Sedlmayr.

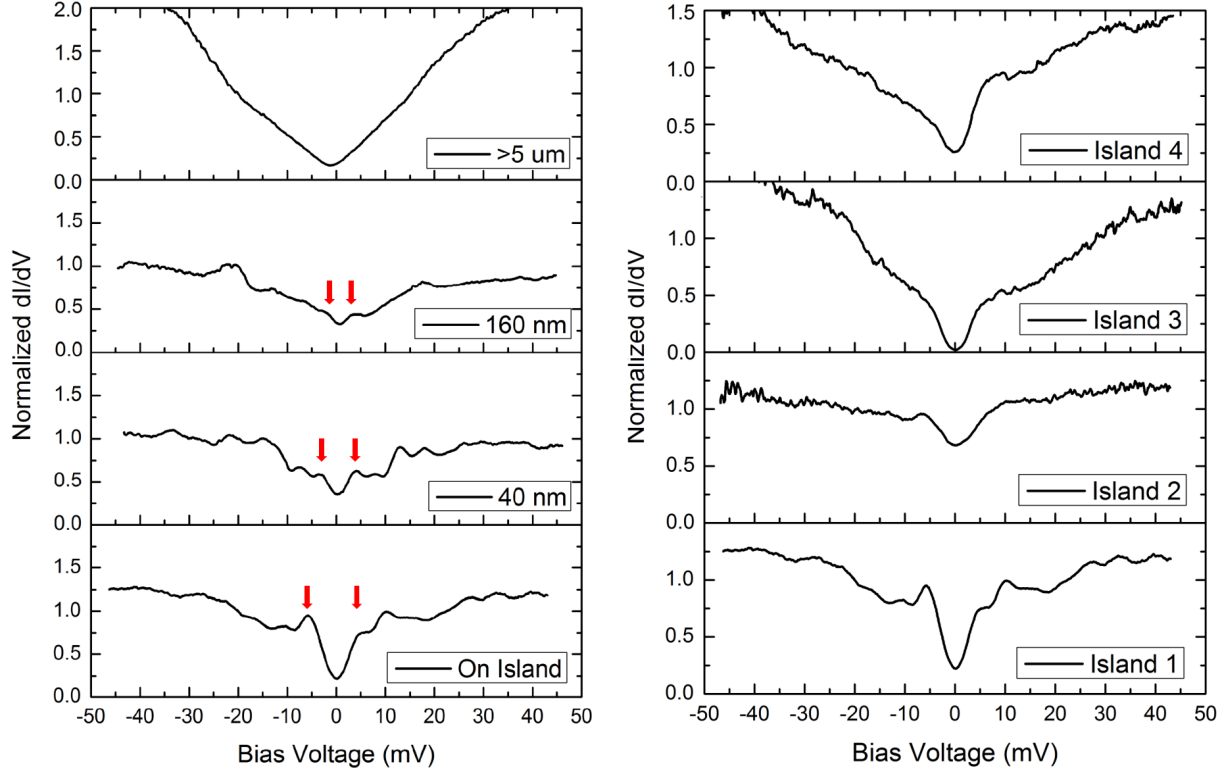


Figure 4.8: The left panel represents dI/dV curves measured at 4.2 K taken at various distances from a PbBi island. The LDOS displays clear signature of the induced superconducting gap, with the arrows denoting the location of the coherence peaks. The only feature at distances far from the superconducting island is the Dirac cone. Another notable feature of the presented data is visible oscillations outside of the superconducting gap. The right panel represents dI/dV curves measured on different islands at nominally the same conditions. The data shown here demonstrates an increasing DOS for both positive and negative voltages outside of the gap, as opposed to the flat DOS predicted by BCS. This is indicative of Dirac cone states in the superconductor. All data are normalized so that $dI/dV|_{-20\text{mV}} = 1$.

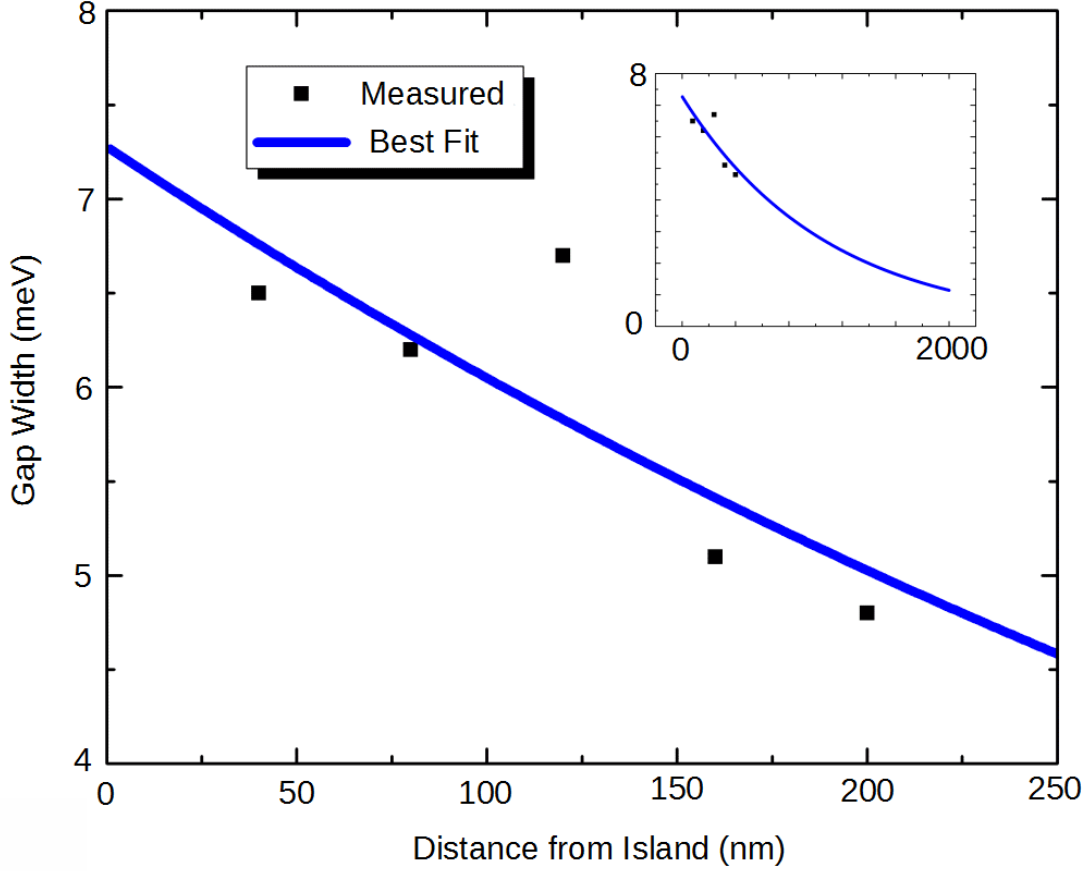


Figure 4.9: Total energy gap width measured by STM at 4.2 K with the expected exponential decay fit, described by the function $\text{Gap Width} = 2\Delta_0 e^{-x/\xi}$, demonstrating that as the probe moves further from the PbBi droplet, the superconducting gap decreases in width. Here the best fit gives a pairing potential of $\Delta_0 = 3.64 \pm 0.40$ meV and a coherence length of $\xi = 540 \pm 200$ nm. In order to extract Δ for each data point, we first took linear fits from -6 – -1 mV and 1 – 6 mV of the dI/dV curve and subtracted them from the full data in order to enhance the coherence peaks on both sides of the Fermi level. The inset shows the data and fitting curve over an expanded distance range.

4.1.4 Theory and Calculations

It has been emphasized in previous chapters that crystals of Bi_2Se_3 possess topological surface states, as well as intra-gap trivial conducting states in the bulk originating from unintentional doping, and importantly also at the surface due to the band bending effect [28]. This coexistence of topological and trivial surface states leads to certain complications in the context of the proximity effect. In particular, phase coherent transport measurements [47, 55, 56] suggest that the superconducting proximity effect of trivial states is in the diffusion dominated transport regime, whereas topological states display transport effects that are specific to the ballistic domain.

In order to gain some theoretical insight into the system, the experimental set-up is modeled in two limits. As a first approach we have considered the diffusive limit that should be relevant to a part of the proximity effect governed by the trivial surface states stemming from the conducting bulk as well as the trivial surface state from band bending. In complete analogy to previously studied mesoscopic superconductor-normal proximity junctions [65, 66] we solved the standard Usadel equation for a circular geometry describing a superconducting island of radius R surrounded by an infinite normal system. Within this formalism the proximity effect is described by the semiclassical Green's function $G(x, \omega) = \cos[\theta(x, \omega)]$ of position and energy that in the normal region obeys the nonlinear equation

$$\frac{\partial^2 \theta}{\partial x^2} + \frac{1}{x} \frac{\partial \theta}{\partial x} + \frac{i\omega}{E_{\text{Th}}} \sin \theta = 0 \quad (4.1)$$

where $x = r/R$ is the dimensionless position coordinate and $E_{\text{Th}} = \hbar v_F l / 2R^2$ is the Thouless energy defined by the Fermi momentum v_F and mean free path l . The LDOS is obtained

from the real part of the Green's function

$$\nu(x, \omega) = \nu_0 \operatorname{Re} \cos[\theta(x, \omega)], \quad (4.2)$$

where ν_0 is the normal density of states without the proximity effect. In a linearized regime, applicable at distances away from the boundary where the proximity effect is weak, an analytical result for Eq. (4.1) is possible,

$$\theta(x, \omega) = \theta_0(\omega) \frac{K_0(x\sqrt{i\omega/E_{\text{Th}}})}{K_0(\sqrt{i\omega/E_{\text{Th}}})}, \quad (4.3)$$

elsewhere the problem must be solved numerically. In Eq. (4.3) $K_0(z)$ is the modified Bessel function and $\theta_0 = \cos^{-1}(\nu_{\text{BCS}}/\nu_0)$ and ν_{BCS} is the BCS density of states on the island. This analysis predicts a reasonable *s*-wave like proximity induced gap E_g in the normal region, see Fig. 4.10(a), albeit with a scale set by the Thouless energy, $E_g \sim E_{\text{Th}}$, rather than a superconducting gap Δ . However it contains no specific information about the microscopic surface state structure of the material, which is neglected in the semiclassical disordered limit. For the typical known values of $v_F \simeq 5 \times 10^5$ m/s and $l \simeq 80$ nm which are specific to Bi_2Se_3 surface states, and $R \simeq 500$ nm, one estimates a proximity induced Thouless gap $E_g \lesssim 1$ meV to be in a proper parameter regime when compared with Δ . [67] Based on this modeling the expected superconducting coherence length for disordered surface states is in the range of $\xi = \sqrt{v_F l / \Delta} \sim 200$ nm. However, in order to fit the actual spatial profile of the decay of the gap function $\Delta(x)$ in the Bi_2Se_3 found in the experiment [see inset in Fig. 4.10(b)] it is necessary to use a fitting parameter of the Thouless scale which is different from what is estimated above. The oscillatory features can also not be reproduced in this

limit as, although in principle the resulting LDOS in Eq. (4.2) is oscillating, it follows from Eq. (4.3) that the oscillation and decay scale of the Bessel function are controlled by the same parameter.

In order to describe the topologically nontrivial surface states and the oscillatory behavior observed in our measurements, we then considered the ballistic limit of the proximity effect. This was done by solving the Gor'kov equations in a planar geometry with a two-dimensional plane consisting of topological surface states with s-wave pairing imposed on one half of the plane, for $x < 0$. The results of these calculations can be described by Bessel functions, which give a very good description of the oscillations seen in the experimental results. In the superconducting side of this model, the theoretical results demonstrate a LDOS with an oscillatory, Tomasch-like nature. On the normal side of the model, the calculations demonstrate a LDOS with oscillatory, Friedel-like nature. Even though this modeling was done for a different geometry than that of our system, we believe that these oscillations are generic. Additional analysis shows that for the spherical symmetry, the Gor'kov equations lead to a LDOS of a more complicated form, resulting in Bessel functions with different harmonics. Regardless, the essence of the effect remains the same.

4.1.5 Conclusions

By depositing superconducting islands on the surface of a topological insulator, we were able to measure induced superconductivity in the surface states of the TI through the superconducting proximity effect through the use of cryogenic STM. We measured the size of the superconducting gap as a function of distance from the superconducting island, and could not only see the superconducting gap shrink as we moved further from the island, but were also able to obtain an estimated coherence length on the order of 500 nm. We

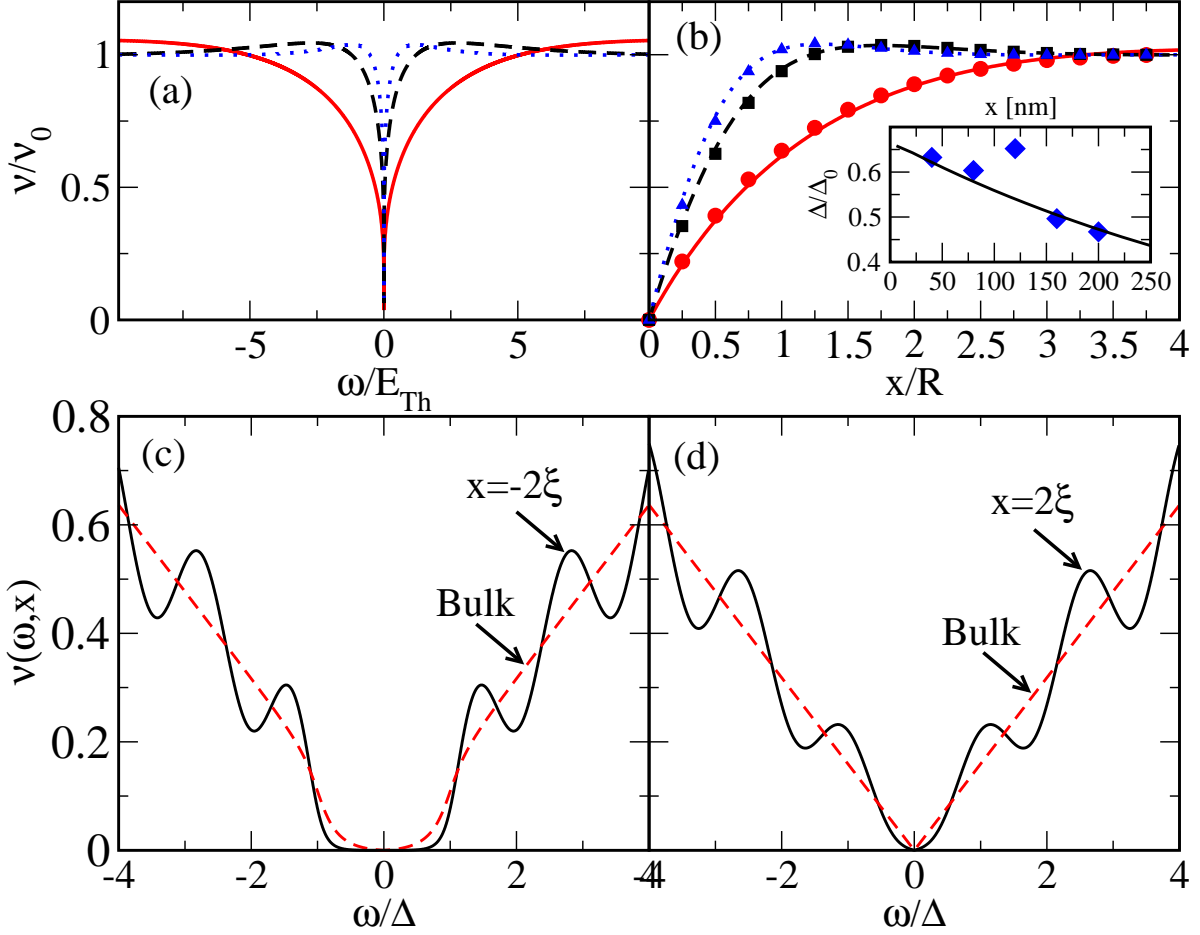


Figure 4.10: (a,b) The local density of states in the diffusive limit as a function of energy (a) at different distances from the boundary of $0.5R$, $1R$, $1.5R$, shown by the red, black, and blue curves respectively, and as a function of position (b) at energies $0.1E_{Th}$, $0.8E_{Th}$, $1.5E_{Th}$, once again shown by the red, black, and blue curves respectively, with lines representing the linearized analytical result, and symbols the numerical result of full nonlinear Eq. (4.1). The inset show a comparison between the gap found experimentally (blue diamonds) and the analytical result (solid line). (c) The local density of states as a function of energy for the topological insulator surface states to the left of the TI/S boundary at 0, which is treated as bulk superconductor. (d) The local density of states as a function of energy for the topological insulator surface states to the right of the TI/S boundary at 0, which is treated as bare topological insulator. A phenomenological damping has been included, and the bulk density of states are included as a comparison.

were also able to observe oscillatory behavior near the superconductor/TI interface, which theoretical modeling predicts is caused by Friedel/Tomasch-like oscillations. Furthermore, we saw evidence of the Dirac cone induced on the superconducting islands, indicating that there exists an inverse proximity effect in which the superconductor is also influenced by the topological surface state.

4.2 Superconducting Proximity Effect of Pure Nb on Bi_2Se_3

4.2.1 Introduction

This section presents further evidence of the superconducting proximity effect, which followed from a collaboration with the Van Harlingen group at the University of Illinois in Urbana-Champaign, IL. The main objective of this collaboration is to utilize their mastery of S-TI-S Josephson junction fabrication in order to image the superconducting TSS inside of a Josephson junction using both STM and SCAI. A great deal of effort has gone into fabricating the ideal samples for imaging under STM, and the final sample fabrication method utilizes their ability to mill trenches deep into the TI substrate and thermally evaporate Nb in patterns with a thickness larger than the coherence length for Nb. This ensures that the Nb will be fully superconducting and that we will get the best results in these measurements.

For the initial study, we decided to take measurements around the edges of the arrays where the tip could be positioned far from the Nb. This allows us to reproduce the experiment with PbBi islands now using Nb as the superconductor. The goal is to measure the induced superconductivity in the Bi_2Se_3 in order to gain further knowledge of the inverse proximity

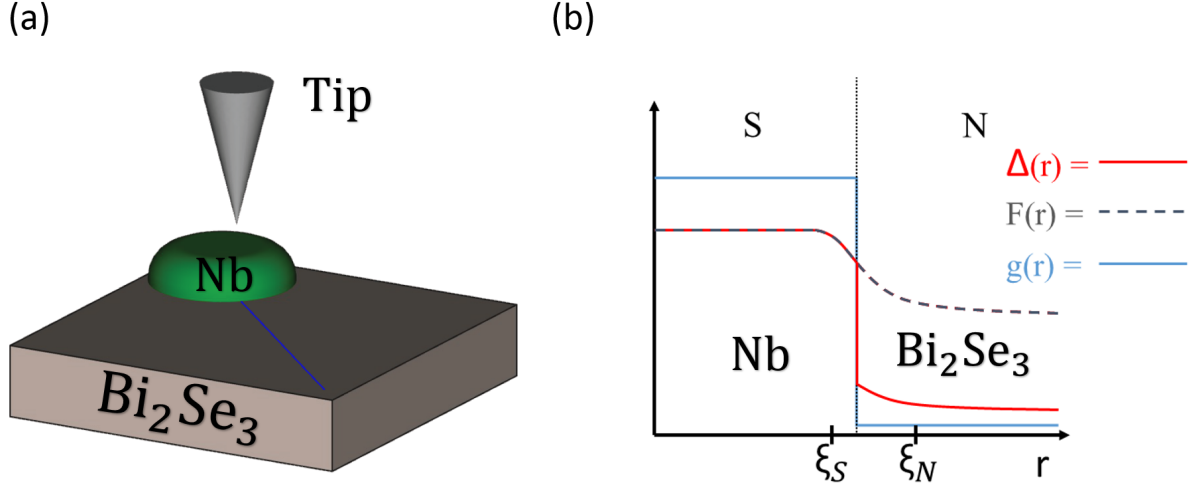


Figure 4.11: (a) A schematic illustration for the geometry of the STM probe scanning over the surface of TI Bi₂Se₃ in proximity to a Nb island. (b) A schematic of the standard proximity effect picture showing the induced superconducting energy gap^[61], Δ , at an interface as a function of position x , where F is the superconducting condensate amplitude. The pairing interaction constant, g , is generally taken to have the form of a clear step function, but at small scales, the step actually has a finite slope due to electronic screening ^[62].

effect and oscillations seen in Sec. 4.1. A schematic illustrating the experiment is shown in Fig. 4.11, with a large scale SEM scan of the sample shown in Fig. 4.12 and an AFM topograph of one of the superconducting arrays shown in Fig. 4.13. An important difference to note between these two experiments is that in Sec. 4.1, we used a cleaved Bi₂Se₃ crystal, whereas for this experiment, the Bi₂Se₃ substrate is epitaxially grown on sapphire. In this section, we will show the results we were able to obtain when the sample was cooled below the superconducting transition temperature.

4.2.2 Results

It is very important that we first establish that there is a high quality Dirac cone in the Bi₂Se₃ before measuring the superconducting proximity effect. We did this by walking the sample far from the Nb arrays and taking spectra over a clean Bi₂Se₃ region. In Fig. 4.14 we

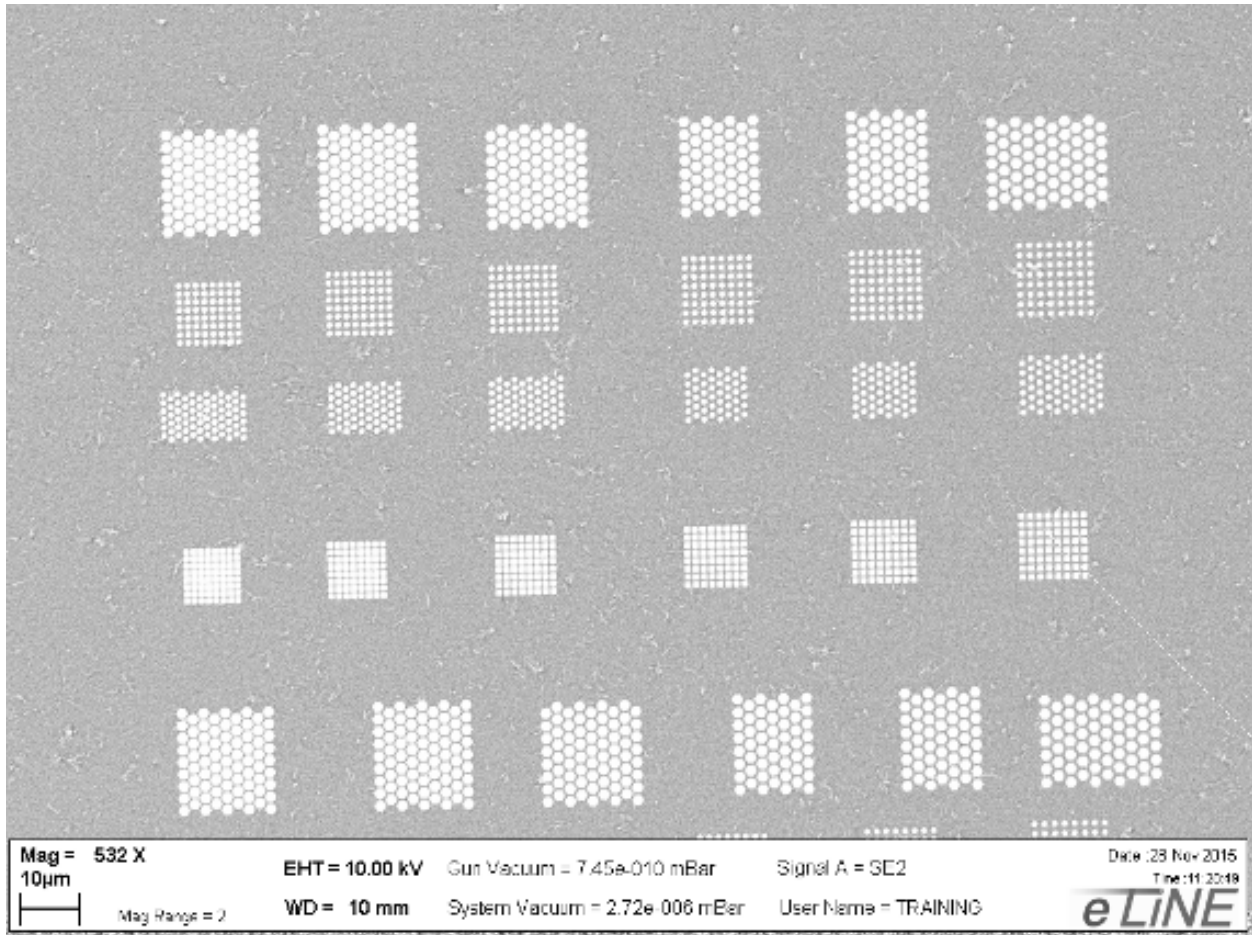


Figure 4.12: SEM image taken by collaborator Can Zhang showing a region of Nb arrays. In this sample we are primarily given square and hexagonal arrays with differing distance in between islands. The sample also contains anti-square arrays, circular arrays (like those used previously in our PbBi and Pb measurements), tri-junctions, and loops junctions. The loop junctions would allow us to thread a magnetic field through a superconducting loop and measure the result from the induced phase difference in the Nb junction. The arrays are necessary in order to eliminate the needle in the haystack problem inherent in STM measurements.

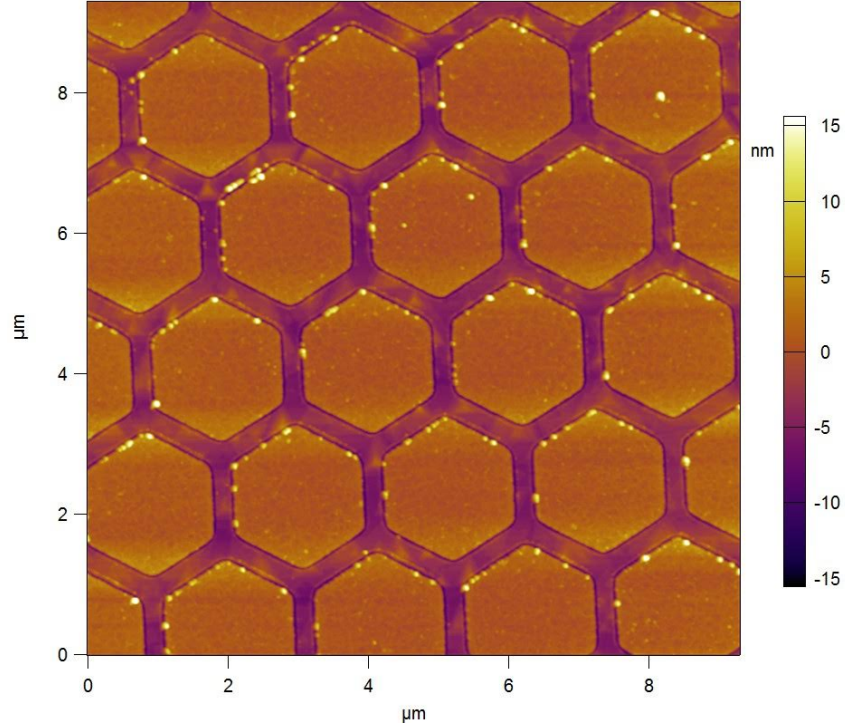


Figure 4.13: AFM topograph taken by collaborator Can Zhang showing an array of hexagonal Nb islands. This demonstrates smooth Nb islands with a clean TI substrate.

can see a clean, sharp Dirac cone that comes close to zero around the Fermi level, which so happens to be at approximately 0 mV. This is indicative that the TI is behaving as predicted far from the Nb arrays and that any induced superconductivity should be happening within the band gap of the TI, and therefore in the topological surface states (as well as in the trivial surface states).

We were also able to acquire a few proximity effect measurements as a function of distance from the superconducting arrays. In Fig. 4.15 we show a measurement showing the gap decrease in size as we move further from the array, but then beginning to increase again as the tip gets closer to another array. As we can often times see in regions near superconducting islands with induced superconductivity, we also saw multiple instances of very clear Tomasch/Friedel-like oscillations. In Fig. 4.16 we show 2 examples where

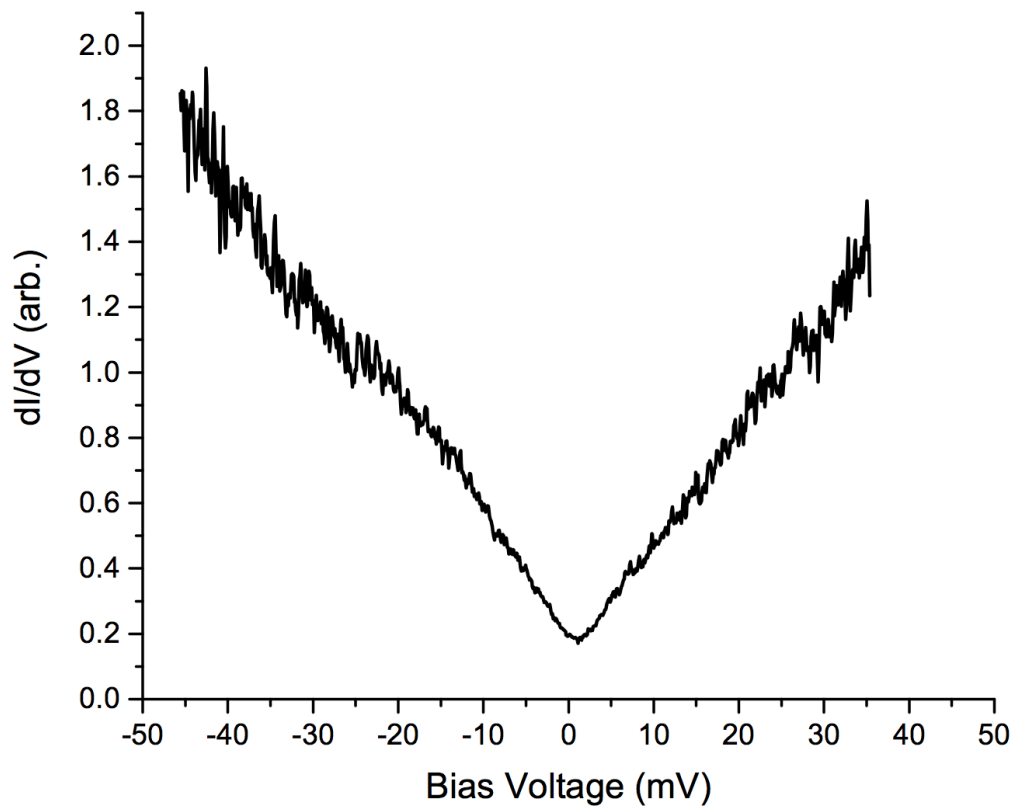


Figure 4.14: Measurement of the Dirac cone taken far from the Nb arrays. This spectrum was taken at 1.78 K. We believe that the cone is not perfectly sharp due to the small amount of thermal broadening at this temperature.

oscillations are very prevalent outside of the superconducting gap. Unfortunately, due to problems with tip stability, we were unable to identify the distance from the superconductor for these spectra. Interestingly, the top curve of Fig. 4.16 looks very nearly like a Dirac cone with the oscillations imposed on the linear DOS. This could stem from being near a Nb island with weak superconductivity, as superconductivity must be present in order for these effects to be observed.

Finally, and possibly the most interesting data thus far from these samples, we observed stronger evidence of the inverse proximity effect on the Nb islands. That is to say, we see clear evidence of the Dirac cone when taking spectra on the Nb as well as on the bare TI surface. This demonstrates that this phenomenon is not just seen in PbBi superconducting islands and that the measurements presented in Sec. 4.1 likely do not stem from the intrinsic spin-orbit coupling found in bismuth.[67] Fig. 4.17 shows five separate measurements of this phenomenon where the Dirac cone can be seen outside of the superconducting gap. What is also surprising is the lack of the clear coherence peaks expected to exist in a pure s-wave superconductor at such low temperatures ($< 2\text{K}$). We have fit a few of the curves with calculated s-wave gaps that have been thermally broadened and with scattering. Since some of the superconducting gaps are much weaker than others taken on Nb, it is possible that BCS alone is not sufficient for describing this phenomenon. Furthermore, we have also taken measurements at room temperature. As shown in Fig. 4.18, the TSS appears to leak into the now normal Nb islands, indicating that the inverse proximity effect does not require superconductivity in order for it to occur.

Dr. Nicholas Sedlmayr has completed some very compelling calculations that demonstrate our interpretation of this data. We believe that there is some hybridization of the TSS with the normal metallic states of the Nb, which is further reinforced by the calculated LDOS

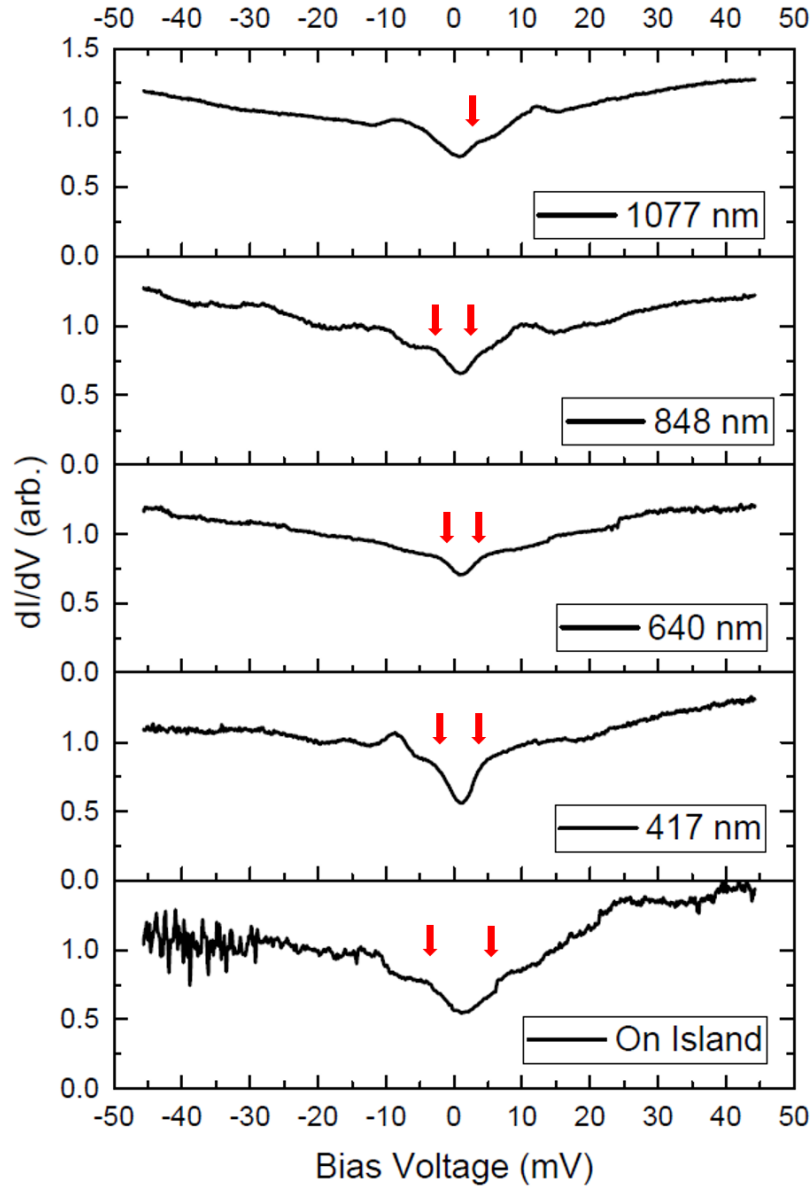


Figure 4.15: Proximity effect measurement taken near $1 \mu\text{m}$ of a Nb array; the distances from the edge of a Nb island are indicated in the plot, where the red arrows note the location of the coherence peaks. We can clearly see the gap decrease in width as we move away from the island, then begin to increase again as we are most likely getting closer to another array. Measurement taken at 1.6 K.

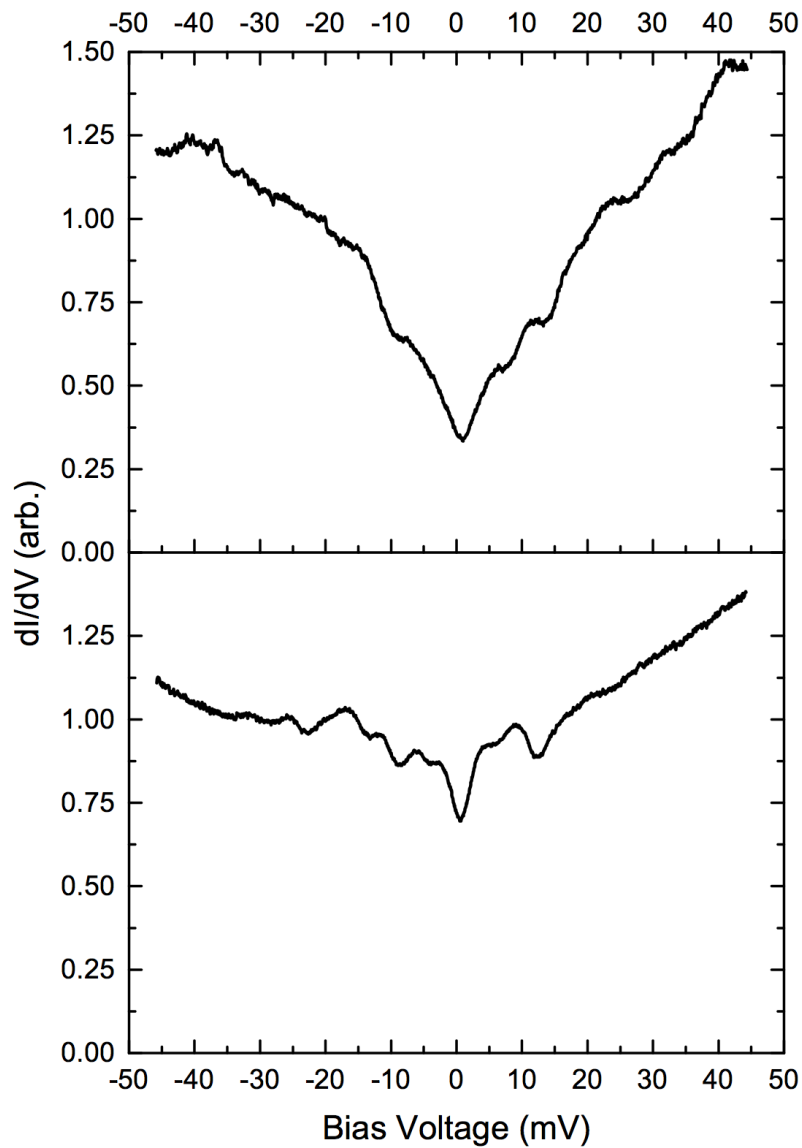


Figure 4.16: Two spectra taken at different points demonstrating Tomasch/Friedel-like oscillations outside of the superconducting gap. Interestingly, the top curve looks like the oscillations are simply superposed on a normal Dirac cone, but since superconductivity must be present in order for the effects to be observed, it is possible that this measurement was taken near a weak Nb island. Measurements were taken at 1.6 K.

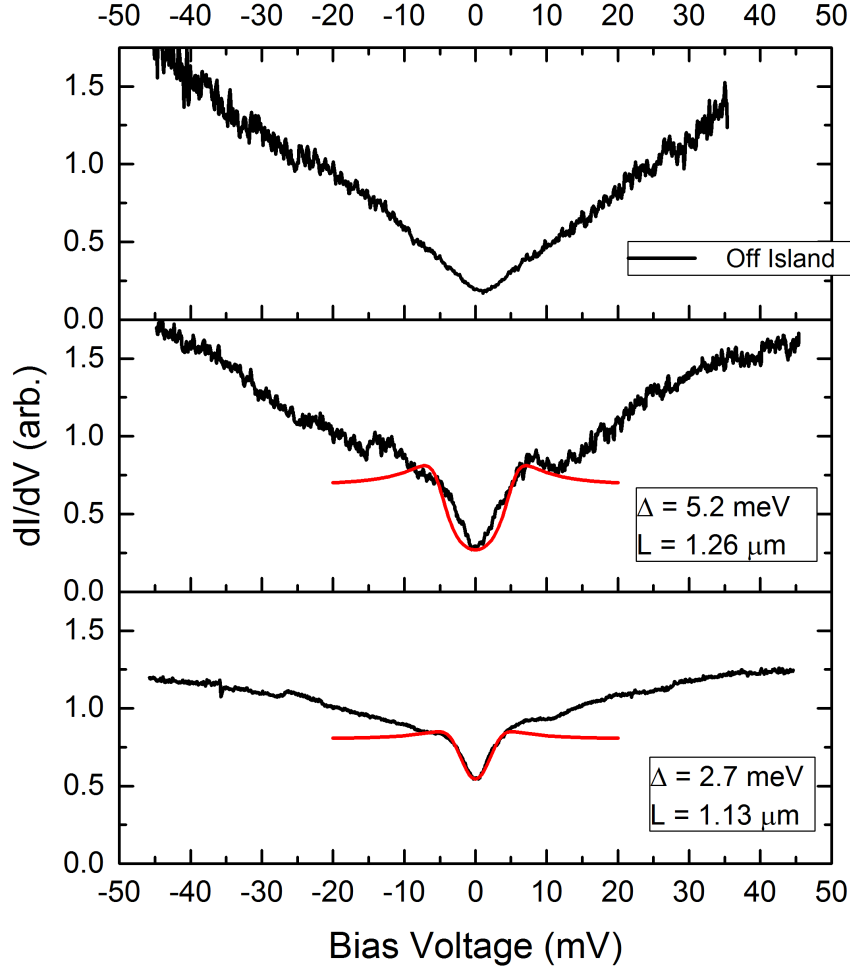


Figure 4.17: Various spectra taken on different Nb islands demonstrating the inverse proximity effect of the TSS on the superconductor. In two curves, we applied fits using calculated s-wave DOS curves that been thermally broadened and had scattering effects applied, where the values of these fitting parameters are shown in the plot. The calculated curves had a temperature of 1.6 K, a coherence length of 38 nm, and a thickness of 60 nm. Surprisingly, we cannot see clear coherence peaks in the superconducting gaps potentially due to the induced TSS forming p-wave superconductivity in the Nb islands. All measurements were taken at temperatures between 1.5-1.8 K, where the superconducting gap is expected to be both very deep and to have sharp coherence peaks. The top curve is a Dirac cone measured in a region of the sample where no Nb islands had been deposited.

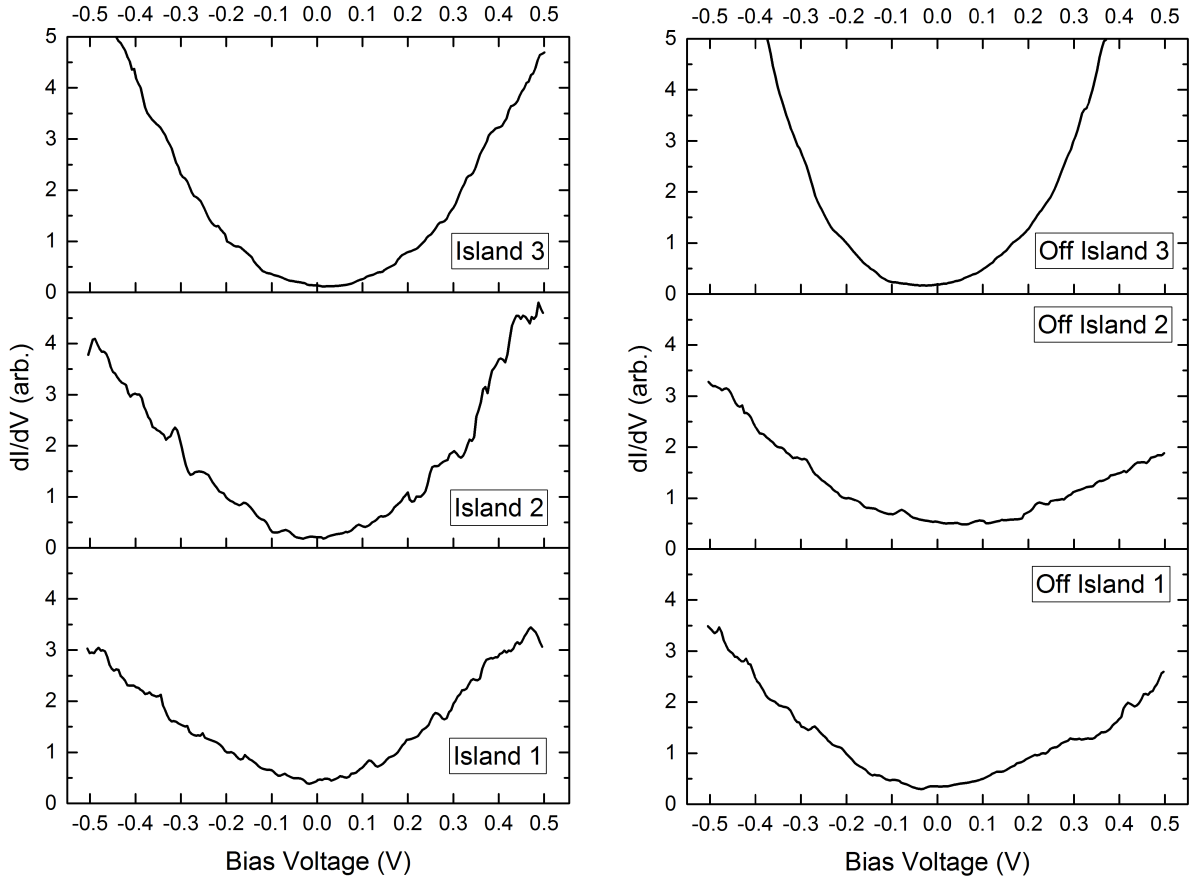


Figure 4.18: Room-temperature spectra taken on and off Nb islands. The 3 curves on the left were taken on Nb islands found in the same array while the curves on the right were taken at 3 separate locations on bare Bi_2Se_3 . We believe that this is the signature of the Dirac cone on Nb at room temperature, which indicates that this inverse proximity effect is likely not dependent on the superconducting state of the Nb and therefore must stem from some other mechanism.

curves shown in Fig. 4.19. Our model demonstrates the there is an intricate interplay of the TSS, the normal metallic states, and BCS pairing. Outside of the superconducting gap (and of course above T_C), the Nb states behave as a normal metal and allow for the TSS to “leak” into the Nb. The calculations presented below come from an exact analytical solution of the system Hamiltonian and a numerical solution for the energy dispersion.

The system Hamiltonian can be described by

$$H = H_M + H_\Delta + H_{TSS} + H_c \quad (4.4)$$

where H_M is the Hamiltonian for a simple, clean 2D metal, H_Δ represents the s-wave pairing of those metallic states, H_{TSS} represents the topological surface states which have leaked into the superconducting islands, and H_c is a local coupling term between the topological surface states and the native metallic states. Specifically for the Nb-Bi₂Se₃ system, $H_{M,\Delta} = \int d^2\mathbf{r} \Psi_r^\dagger \mathcal{H}_{M,\Delta} \Psi_r$, where \mathbf{r} is the spacial coordinate (x, y) in two dimensions, $\mathcal{H}_M + \mathcal{H}_\Delta = \hat{\xi} \tau^z + \Delta \tau^x$ in the Nambu basis, $\Psi_i^\dagger = \{c_{r\uparrow}^\dagger, c_{r\downarrow}^\dagger, c_{r\uparrow}, -c_{r\downarrow}\}$ and a corresponding wave-function ψ_r^T written in terms of the Bogoliubov-coherence factors: $\{u_{r\uparrow}, u_{r\downarrow}, v_{r\uparrow}, v_{r\downarrow}\}$. The operator $c_{r\sigma}^\dagger$ creates a particle of spin σ at position \mathbf{r} . Here, we use $\vec{\tau}$ as the Pauli matrices acting in the particle-hole subspace and $\vec{\sigma}$ as the Pauli matrices in the spin subspace. The quasi-particle dispersion is assumed to be quadratic for low moment $\hat{\xi} = -\nabla^2/2m - \mu$ where μ is the chemical potential. $H_{M,\Delta}$ is completely diagonal in spin. The Hamiltonian describing the topological surface states can be described by $H_{TSS} = \int d^2\mathbf{r} \chi_r^\dagger \mathcal{H}_{TSS} \chi_r$, where $\mathcal{H}_{TSS} = (iv_F \nabla \cdot \vec{\sigma} - \mu_{TSS}) \tau^z$ is acting on $\chi_r^\dagger = \{a_{r\uparrow}^\dagger, a_{r\downarrow}^\dagger, a_{r\uparrow}, -a_{r\downarrow}\}$. The operator $a_{r\sigma}^\dagger$ creates a particle with spin σ at position \mathbf{r} . Finally, the coupling Hamiltonian H_c can be described by $H_c = \gamma \int d^r \mathbf{r} [\chi_r^\dagger \tau^z \Psi_r + h.c.]$, which represents a local spin-independent

hybridization described by the parameter γ .

The numerical solution to the energy dispersion is described by the equation

$$\epsilon_k^{\alpha\beta\delta} = \frac{\alpha}{\sqrt{2}} \sqrt{2\gamma^2 + \Delta^2 + \xi_k^2 + \zeta_{k\delta}^2 + \beta \sqrt{[\Delta^2 + \xi_k^2 - \zeta_{k\delta}^2]^2 + 4\gamma^2[\Delta^2 + (\xi_k + \zeta_{k\delta})^2]}} \quad (4.5)$$

where α physically accounts for the particle-hole symmetry of the energy, δ accounts for the different spin bands, β accounts for the mixing of the TI/S electron species, Δ is the superconducting pairing potential, γ is the tunable pairing strength between the TSS and normal metal states, ξ_k is the dispersion of the metallic states, and $\zeta_{k\delta} = kv_F - \delta\mu_{TSS}$, where v_F is the Fermi velocity for the TSS and μ_{TSS} is the chemical potential for the TSS. Mathematically, $\alpha, \beta, \delta = \pm 1$ to account for all 8 possible energy bands. When $\gamma \rightarrow 0$, the dispersion relation recovers the BCS and TISS dispersions. The DOS can be calculated from this energy dispersion by numerically solving the equation

$$\nu(\epsilon) = \int_0^\infty \frac{d\mathbf{k}}{2\pi} e^{\frac{-(\epsilon - \epsilon_k)^2}{\Gamma^2}} \frac{1}{\sqrt{\pi}\Gamma} \quad (4.6)$$

where Γ is a broadening energy.

Interestingly enough, the best fit data in these calculations occurs when superconductivity is induced in both the “native” electron states as well as the leaking TSS in the superconductor via the coupling term γ . As shown in Fig. 4.20, very good fits using the model can be generated. Fig. 4.20(a-c) all utilize v_F , γ , and a broadening term Γ as free parameters, while Fig. 4.20(d-f) utilize v_F , γ , Γ , and Δ as free parameters. By carefully tuning Δ , we acquire better fits as the proximity of the superconductor to the TI as well as the leaking surface states will of course affect the value of Δ in the superconducting material. An important

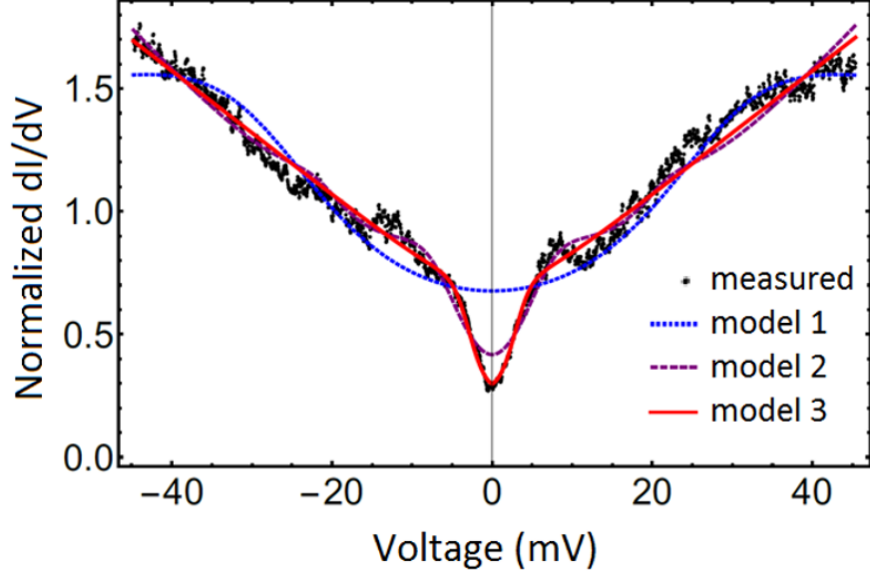


Figure 4.19: LDOS data with theoretical curves based on a model that includes native metallic states and proximity coupled TI surface states. Model 1 (blue) has no BCS pairing. Model 2 (purple) has BCS pairing in the native metallic states only. Model 3 (red) has pairing in both the native and the proximity-coupled TI states.

finding to note is that these fits utilize a v_F on the order of ~ 100 m/s. This is greatly reduced from the expected v_F of Bi_2Se_3 , which is $v_F = 5 \times 10^5$ m/s.[31] We believe this can be attributed to the fact that the TSS in the superconductor is spreading perpendicular to the direction of electron “flow”, thus dramatically decreasing the Fermi velocity v_F . This can be thought of as the quantum analog of a fluid expanding from a small reservoir into a larger reservoir.

4.2.3 Conclusion

This experiment has been successful in that we were able to measure induced superconductivity in the Bi_2Se_3 TSS as well as an induced Dirac cone in the Nb superconductor. Not only do we find more convincing evidence of the inverse proximity effect of a TI on a superconductor, we also assembled a model which can nicely describe this phenomenon. By tuning various parameters in the theoretical calculation, we see very accurate fits to the data, which help to

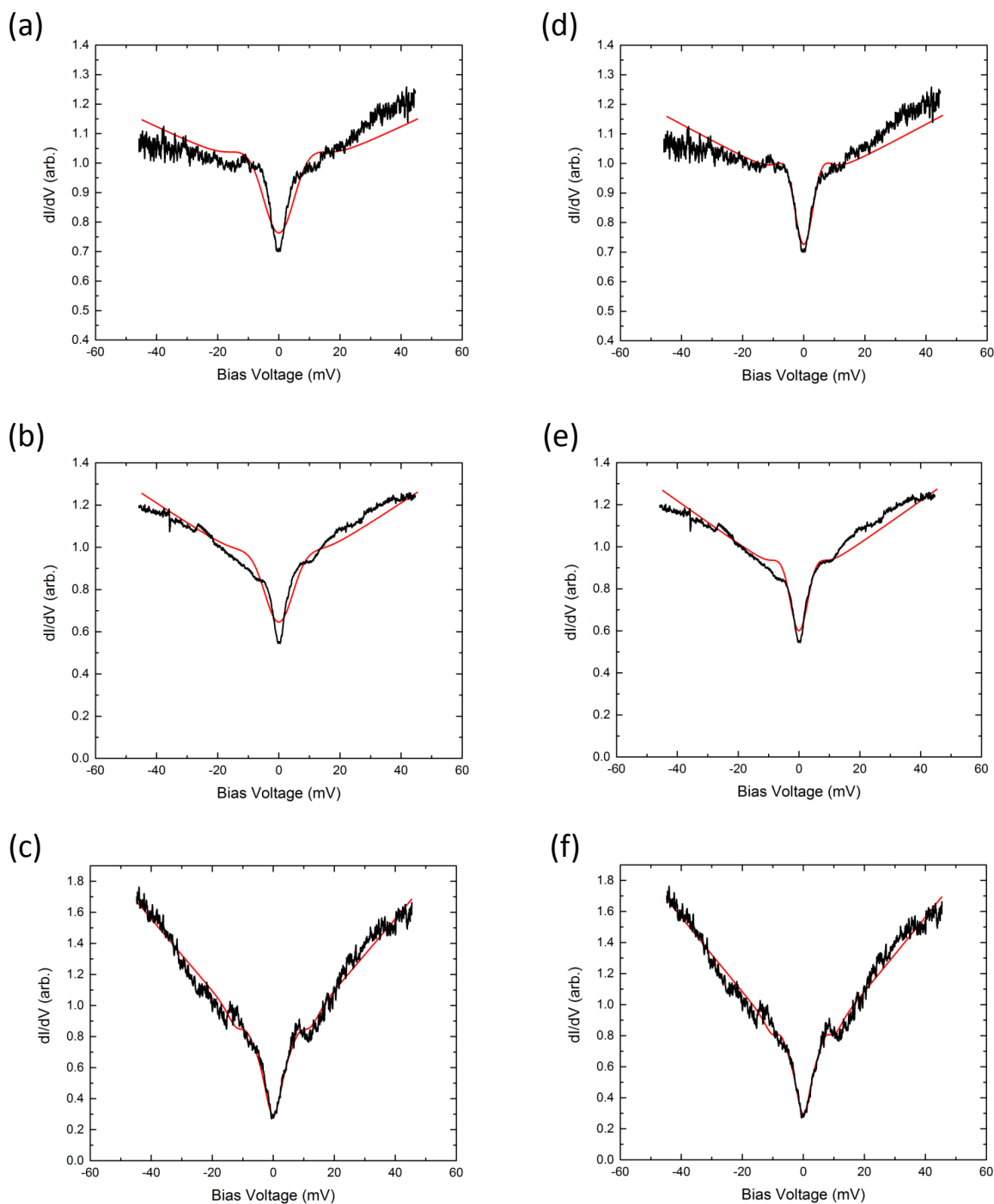


Figure 4.20: Experimental data of the DOS taken on 3 separate islands with calculated fits demonstrating the leakage of the TSS into the superconducting Nb islands. (a-c) all utilize v_F , γ , and a broadening term Γ as free parameters while (d-f) allow Δ to be a free parameter in the calculation as well. In general, (d-f) have better fits as it is expected that Δ will be influenced by both the proximity to the TI material as well as the TSS states leaking into the superconductor.

verify our current interpretation of this inverse proximity effect.

Chapter 5

Conclusions

5.1 Summary of Results

The primary scope of this work was to utilize scanning tunneling microscopy and subsurface charge accumulation imaging to measure the various proximity induced effects that superconductors and conventional insulators have on topological insulators. In terms of superconducting/topological insulator interfaces, we successfully measured the superconducting coherence length as well as observed multiple unexpected behaviors, both in the density of states of the topological insulator as well as the superconductor. We observed oscillatory behavior near the interface of these two materials, which we believe to be Friedel/Tomasch-like states enhance by Andreev reflection at the boundary. We also observed the rather surprising inverse proximity effect of a topological insulator on a superconductor, both in the normal and superconducting phases. The fact that the Dirac cone can leak into the normal conducting states of a superconductor can lead to a multitude of interesting and unexpected results in the future.

5.2 Future Goals

Our TI-superconductor proximity effect measurements show clear evidence of the Dirac-cone-like states that appear in the superconductor, which we call the inverse proximity effect. An

important question raised by these observations is the degree to which these states retain their topological character. In other words, is there an effective “topological coherence length on the superconducting side of the interface that sets the distance over which momentum and spin will be locked? To explore this question, in the near future we plan a series of STM measurements on continuous Nb films of varying thicknesses grown on Bi_2Se_3 . We will characterize the degree to which Dirac cone states appear in the DOS and resolve spatial patterns in the defect scattering, similar to the STM measurements performed by the Yazdani group on TI surfaces.[68]

The Tessmer group is also in the process of moving towards another exciting experiment which will probe the landscape of the critical current in S/TI/S junctions. This project will come from continued collaboration with the Van Harlingen group and will utilize all of the methods presented in this dissertation. A schematic of the proposed experiment is shown in Fig. 5.1. We will use the SCAI measurement method and the topological insulator proximity effect discussed in Appendix B in these S/TI/S junctions to tune the location of the super current and to observe the path of the Josephson current in the x-y plane, as well as the vertical positions of the charge carriers.

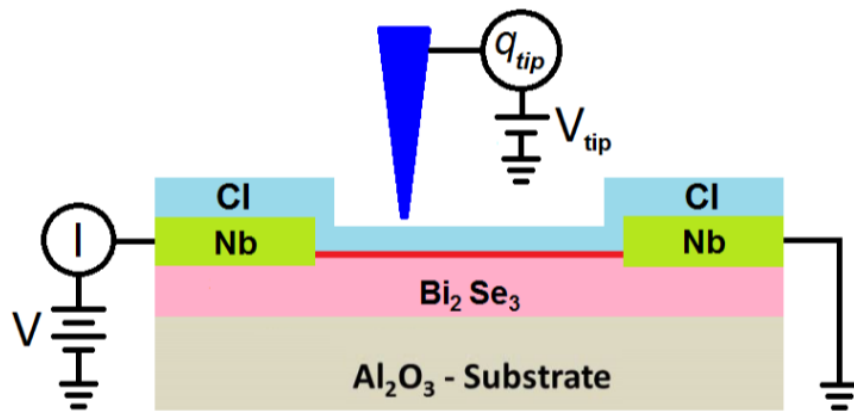


Figure 5.1: Schematics of the proposed measurement which will utilize SCAI measurements to measure the path of the Josephson current in a biased S/TI/S junction.

APPENDICES

Appendix A

Superconducting Proximity Effect of Pb on Bi_2Se_3

Introduction

Prior to our experiments utilizing a PbBi alloy for our superconducting material, we did extensive measurements using pure Pb as the superconductor as well. While this work did not directly make it into a publication, it is important to note our results from these data sets as well and to understand why we finally moved to the alloyed superconductor PbBi. It is during these measurements that we were able to solidify our sample preparation methods as well as establish some of the important preliminary results and measurement techniques used to get the data presented in Sec. 4.1.

Experiment

In our preliminary experiment, we still utilized $\text{Bi}_{2.04}\text{Se}_{2.96}$ as the TI substrate. The preparation methods are identical to those from Sec. 4.1 with the important note that we used Pb instead of a PbBi alloy for the superconductor. We initially thought this to be an ideal material as it also has a reasonably high transition temperature of 7.25 K and an energy gap of 2.61 mV. [64]. A control measurement of a 400 nm thick Pb layer deposited on the

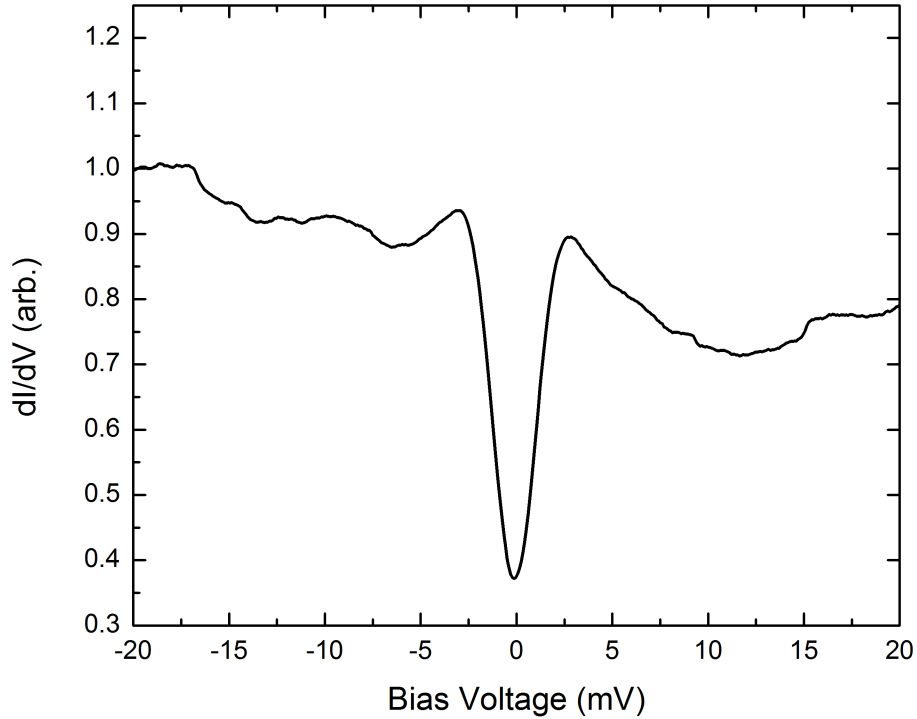


Figure A.1: STS taken on a 400 nm thick layer of Pb deposited on the surface of Bi_2Se_3 . Here we can see a very clear superconducting gap as well as signatures of phonon oscillation modes outside of the superconducting gap. This measurement was taken at 4.2 K.

surface of Bi_2Se_3 is shown in Fig. A.1, where we can see a very clear superconducting gap with a width of around 2.8 mV, which when accounting for broadening effects, is around the expected value of 2.61 mV.

Of course, we also conducted some baseline measurements in terms of Pb deposition quality. Fig. A.2 shows an AFM topograph of a Pb island array. We can once again see that, like the PbBi islands, the Pb islands also comprise of smaller droplets. When doing measurements in the STM system however, the surface was much more unstable possibly due to the rapid oxidation of pure Pb or the general jaggedness of the evaporated Pb surface. It better suited our work to move to a PbBi alloy as it generally formed much smoother films

on the TI surface. This made it much easier to create more stable surfaces for STM as a small amount of air exposure would not affect the sample so dramatically.

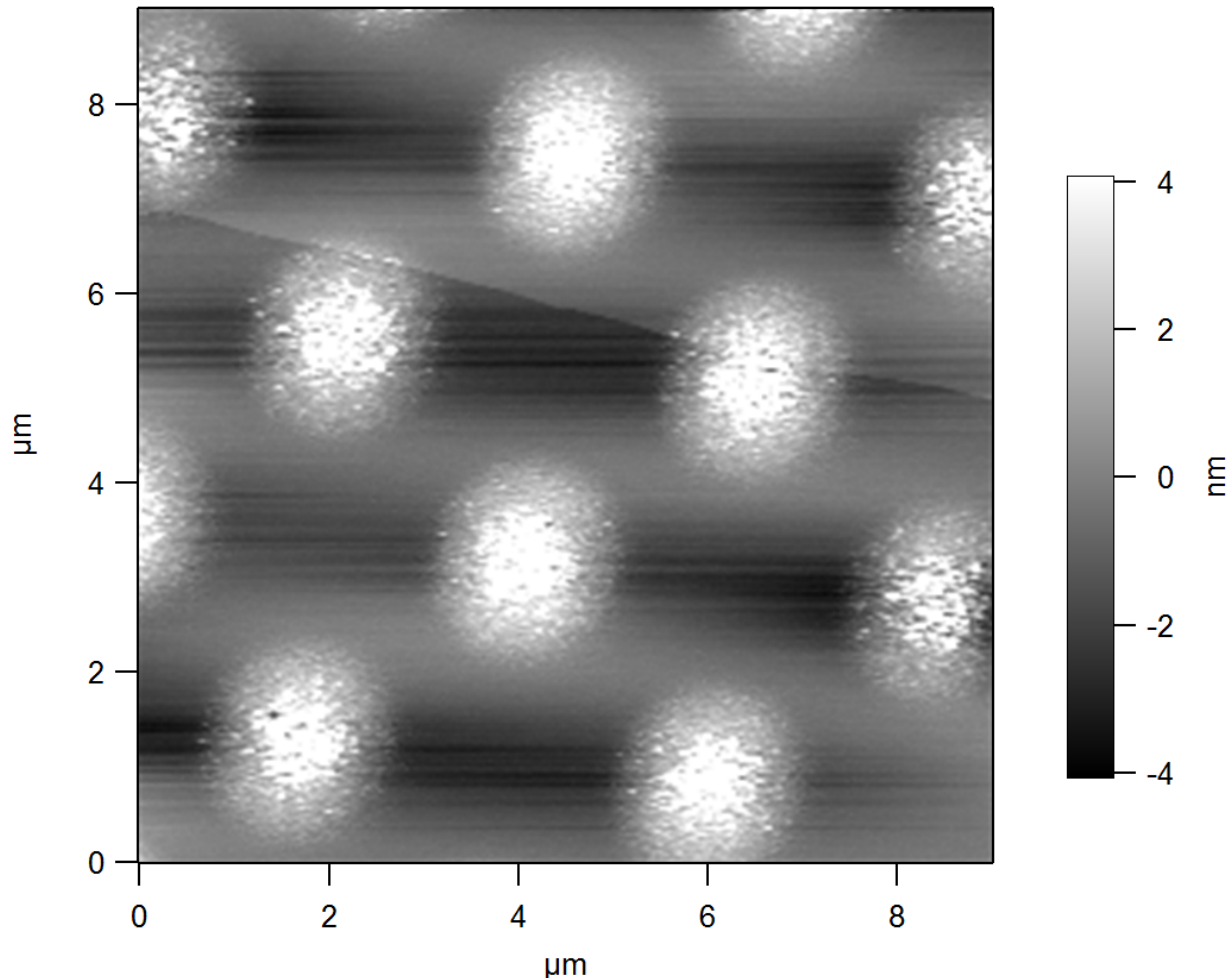


Figure A.2: AFM topograph of Pb islands deposited on the surface of Bi_2Se_3 . The islands are grainy, much like the PbBi samples, but also are heavily oxidized due to the intrinsic nature of Pb exposed to air.

As such, we put a great deal of effort into trying to measure the superconducting proximity effect using these samples. The best measurement from this specific geometry is shown in Fig. A.3. This data is a clear demonstration of gap-like density of states measurements appearing near Pb islands, but the induced gap is far too wide to be induced by superconductivity. We believe that these DOS curves could stem from charge density waves caused by lattice

misalignment from the sample preparation steps. Regardless, it was very difficult to get high quality STM measurements on or around the Pb islands due to high mechanical instability of the STM tip caused by unstable Pb structures.

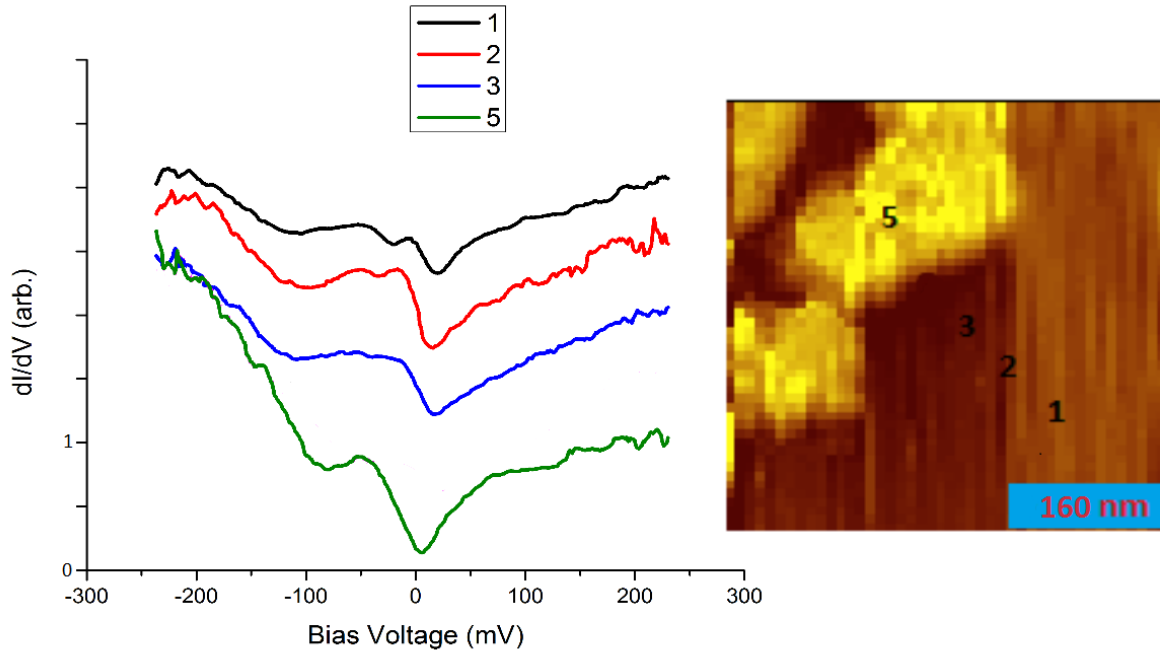


Figure A.3: STM data taken on a sample made with Pb/Bi₂Se₃. While we can see a pretty clean interface, the STS data show induced gaps that are far too wide to be superconducting. We believe that these gaps stem from charge density waves caused by lattice misalignment of the TI crystal. We exclude data from position 4 in the image due to very high mechanical instability at the interface.

This stage of our experiment may not have been fruitful in terms of measuring the induced superconductivity in Bi₂Se₃, but it was crucial in that it taught us how to make the samples consistently as well as what material to use to get the high quality data shown in Chap. 4.1.3.

Appendix B

Topological Insulator/Conventional Insulator “Dual” Proximity Effect

We have already demonstrated that placing a TI in contact with a normal metal or superconductor creates a multitude of fascinating phenomenon, but what would happen if we put the TI in contact with a conventional insulator (CI)? According to the original TI theory, placing a TI in contact with a CI would harbor no interesting physics since we stated in Sec. 3.1 that the TSS exists at the boundary between the bulk of a TI and a trivial insulator (usually vacuum). As it turns out, this is not entirely correct and depends on the specific conventional insulator that we put at the interface. In this chapter I will discuss the theoretical predictions as well as some of our preliminary experimental results on this matter.

Theory and Motivation

When placing a TI in contact with a CI, which has a Chern invariant $\nu = 0$, the theory present in Sec. 3.1 predicts that the topological surface state will exist at the interface. As it turns out, more subtle behavior is possible. In 2013, Wu et. al. published density functional theory (DFT) calculations demonstrating that the topological surface state location can actually be tuned depending on what material is placed on the surface. [2] In the case of these calculations, Wu used Zn based insulators, each of which harbors different predicted

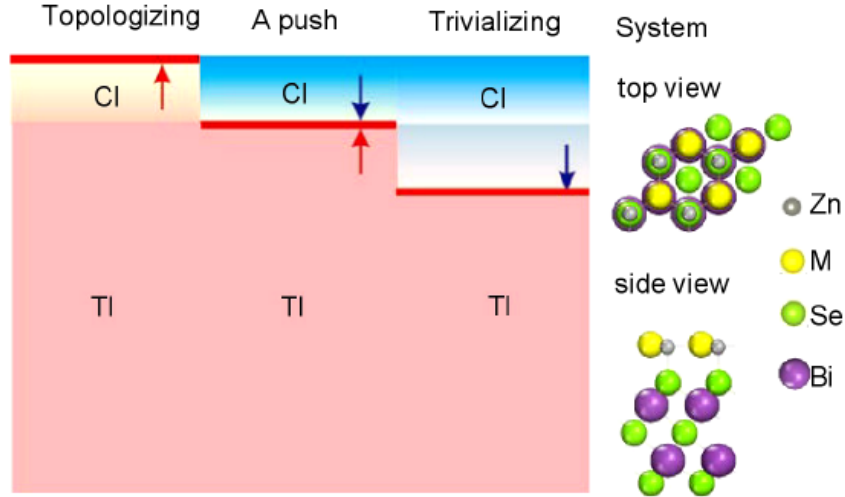


Figure B.1: Figure taken from Wu et. al. demonstrating the possible behavior of the TSS when a CI is put in contact with a TI. The TI will either “topologize” the CI, causing the TSS to float to the surface, become trivialized by the CI, pushing the TSS down one QL, or the materials will not affect one another in any meaningful way, leaving the TSS at the interface.[2]

behaviors. In Fig. B.1, we can see the three possible behaviors; the TSS floats to the top of the CI, the TSS remains at the interface with the CI, or the TSS is pushed down one quintuple layer (QL) into the TI. This behavior is known as the “dual” proximity effect, and it depends not only on the material of the CI, but also upon the choice of TI used in the experiment. In this case, the two possible TI’s are either Bi_2Se_3 or Bi_2Te_3 , while the CI’s could be ZnS , ZnSe , or ZnTe . The ability to tune the location of the TSS could be very useful in that we would be able to possibly push the TSS down one quintuple layer into the TI, isolating it from surface defects and allowing for a more pure TSS. Likewise, we could also pull the TSS further from the bulk of the TI and potentially improve the thermoelectric properties of the TI material.

The DFT calculations done by Wu et. al. by using a 6 QL thick TI with a specific CI deposited on the surface. An example of the calculated results can be seen in Fig. B.2. In this case, the top curves show the interaction of $\text{ZnS}/\text{Bi}_2\text{Se}_3$ and the bottom curves show the

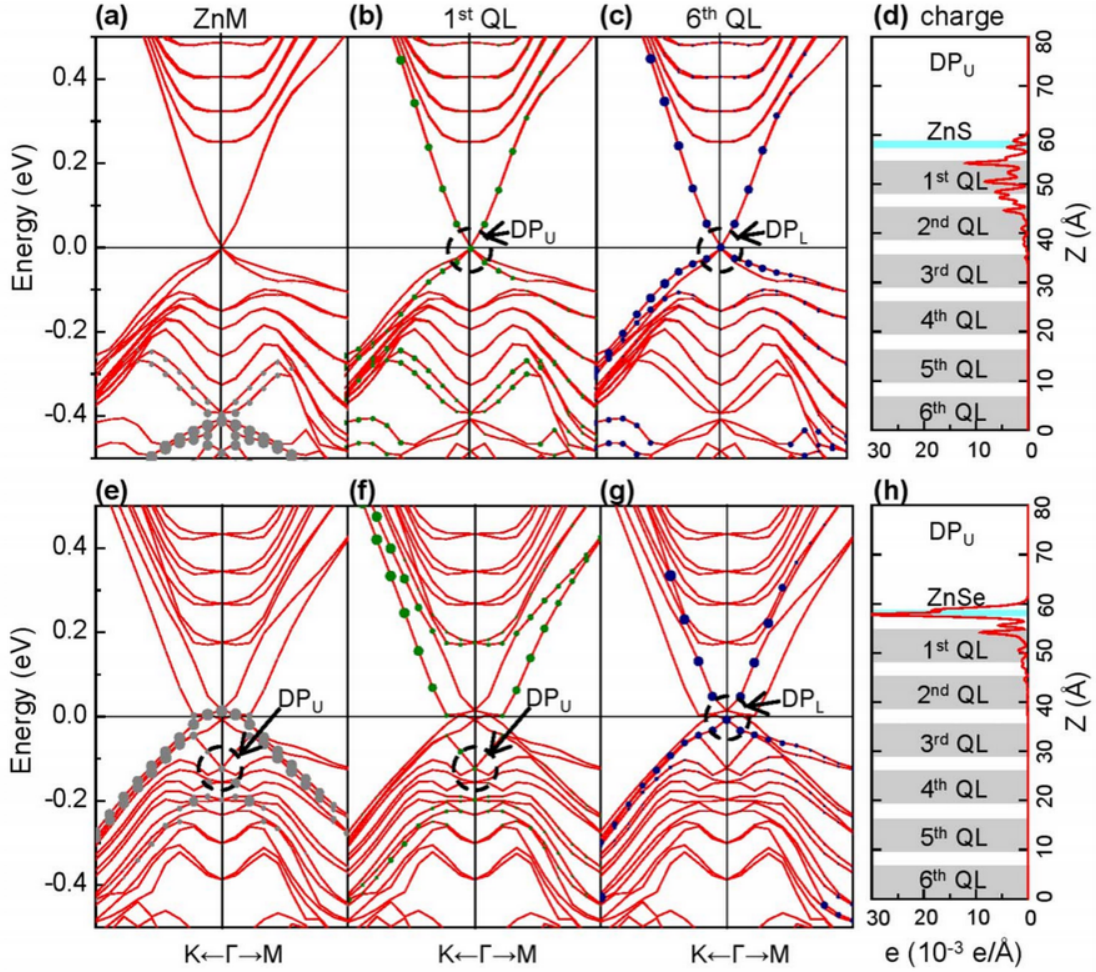


Figure B.2: DFT calculation taken from Wu et. al. showing the band structures of differing TI/CI interfaces, specifically ZnS/Bi₂Se₃(a-d) and ZnSe/Bi₂Se₃(e-h). The dots indicate the spectral weights and contributions from differing atoms, denoted by the size and color respectively. DP_U and DP_L denote the Dirac points of the upper and lower surfaces respectively.[2]

interaction ZnSe/Bi₂Se₃. As expected in both cases, the TSS continues to exist at the bottom of the TI (the 6th QL), but interestingly, it changes location based on the CI material. In the case of ZnSe on Bi₂Se₃, the CI is essentially made into another layer of the TI (“topologized”) and the TSS leaks onto the surface of the ZnSe. Whereas in the case of ZnS on Bi₂Se₃, the TSS remains in the first QL at the interface between the materials. This can be seen clearly in Fig.B.2(d) and (h), where the charge density is mapped for each layer.

To completely summarize the results of the paper, we can look to Table B.1. Here we can

System (Substrate)	V_g (eV)	Φ (eV)	a (Å)	Δa	E_b (eV)	Z
ZnS (Bi ₂ Se ₃)	1.82 (0.40)	6.10 (5.55)	3.82 (4.14)	+8.4%	0.06	Interface
ZnSe (Bi ₂ Se ₃)	1.58 (0.40)	5.77 (5.55)	4.00 (4.14)	+3.5%	0.09	Top
ZnTe (Bi ₂ Se ₃)	1.85 (0.40)	3.98 (5.55)	4.31 (4.14)	-3.9%	0.29	Inside
ZnTe (Bi ₂ Te ₃)	1.39 (0.39)	4.93 (5.00)	4.31 (4.38)	+1.6%	0.19	Top

Table B.1: Table summarizing the results of the Wu et. al. paper and labeling the characteristic properties of the materials used in the calculations. V_g is the band gap width, Φ is the work function, a is the bulk lattice constant, Δa is the lattice mismatch, E_b is the binding energy between the CI and TI layers, and Z is the location of the TSS for the specific geometry calculated.[2]

see that the most interesting results occur when the CI is ZnSe or ZnTe on Bi₂Se₃ or ZnTe on Bi₂Te₃. In this experiment, we attempt to investigate the location of the TSS when ZnSe is deposited onto the surface of Bi₂Te₃, which does not have a calculated prediction for the behavior of the TSS.

Experiment

Sample Preparation

Our samples, grown by the Sou group at the Hong Kong University of Science and Technology, consist of 10 nm of bulk TI Bi₂Te₃ with 1-2 nm of CI ZnSe grown on the surface of the TI. This is all grown on top of n-doped GaAs and is shipped to us with a 20 nm Te capping layer to protect the surface of interest. Because the Te cap layer cannot be removed in-situ, we have developed a sample preparation method in which the Te cap layer is removed and the sample remains in nitrogen gas or vacuum for the duration of the experiment.

In order to handle the sample easier, we first attach it to a larger piece of undoped GaAs via In solder. This is done by heavily scratching the bottom of the n-doped GaAs chip in order to remove the oxide layer and allow the In to establish good electrical contact with the

sample. We then place the large undoped GaAs chip on a hot plate with a large amount of In solder on the surface, where we then sandwich the In between the sample and the GaAs chip. After this is cooled, we then load the sample into an oven and bake it at 315 °C for 20 minutes in a nitrogen gas environment. In order to demonstrate that the Te cap layer was successfully removed, we did AFM and STM on a baked and unbaked sample, as shown in Fig. B.3. Here we can see two clearly defined regions which we believe to be the ZnSe terraces and the bare Bi₂Te₃ surface. We also did energy-dispersive X-ray spectroscopy (EDS) to classify the materials exposed on the surface before and after baking, which demonstrated that the Te cap layer was completely removed by the baking process. After baking, the sample is then removed from the oven and silver painted on the metal sample disc for measurement. A silver paint bridge is also made from the In solder to the sample disc in order to ensure good electrical contact. In this case, the resistance between the sample surface and the sample disc is approximately 5 kΩ at room temperature, which is indicative of good conductivity for the purposes of STM. A diagram showing the final result can be seen in Fig. B.4. After the sample is prepared, it is loaded into the microscope and cooled to 77 K.

Measurement System

The system we use to conduct STM and SCA imaging on our samples is the house built system shown and discussed in Chapter 2. By utilizing our HEMT circuit, we are able to freely change between STM and SCA with ease, allowing us to get many measurements and maximize our ability to characterize the physics we see during this measurement.

The geometry of the experiment is demonstrated in Fig. B.5. We have various terraces on ZnSe on the surface, which we will situate the scanning probe over and sweep the bias voltage. When the TSS changes location, we will see a change in capacitance, which will

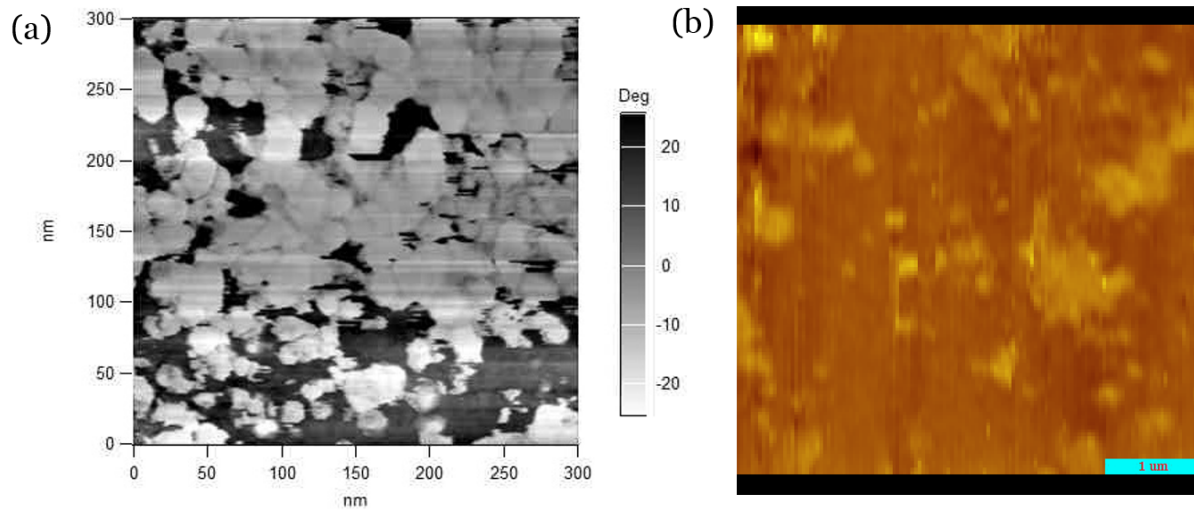


Figure B.3: (a) AFM phase retrace demonstrating different materials on the surface of a baked sample. (b) STM topograph of the sample, demonstrating the same features seen in the AFM scan shown in (a).

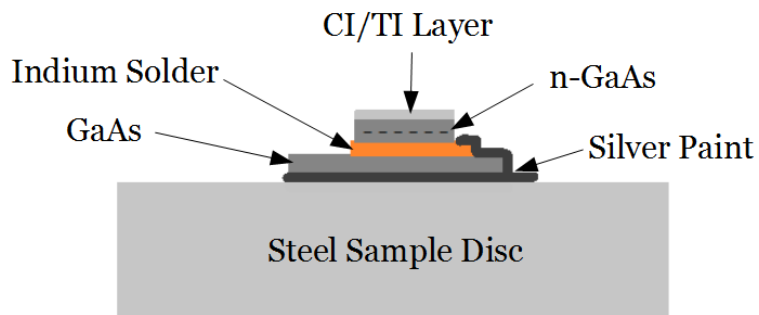


Figure B.4: Diagram showing sample after baking and assembly. The sample itself is usually around 3 mm in size in order to allow for a large area to scan using our surface probes.

translate to a step in the compressibility measurement.

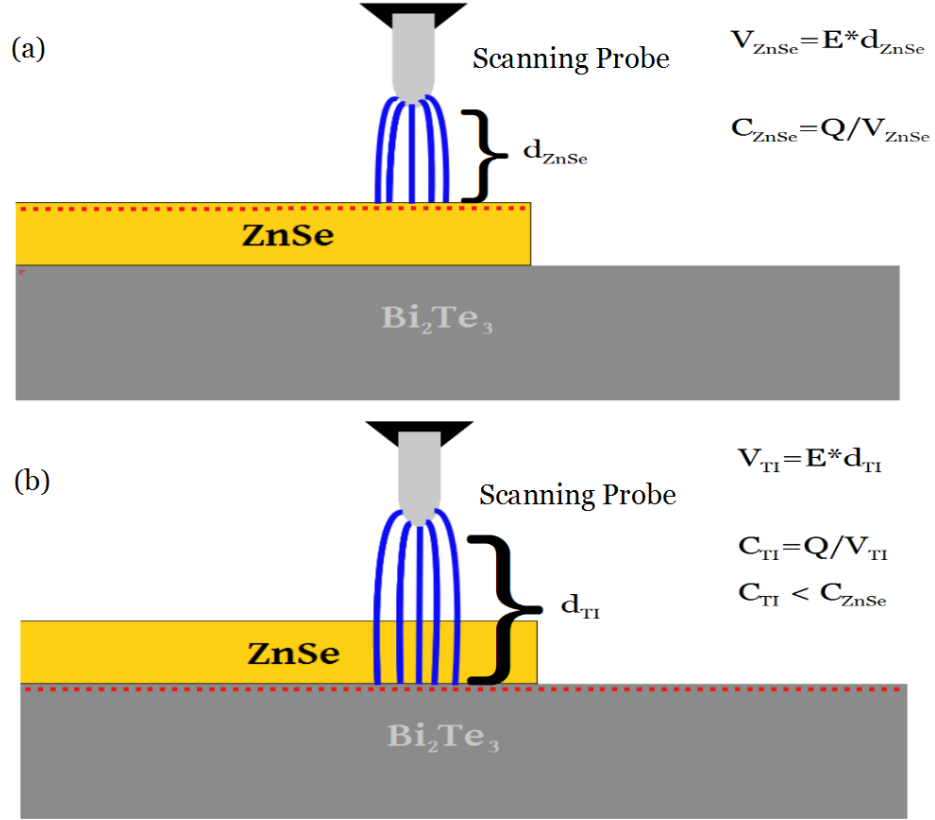


Figure B.5: (a) The electric field between the tip and the TSS in the ZnSe terrace has a set capacitance C_{ZnSe} . (b) The electric field between the tip and the TSS in the Bi_2Te_3 layer with a capacitance of $C_{\text{Bi}_2\text{Te}_3}$. Here we would see a smaller capacitance because of the larger distance between the two capacitive “plates”.

To reiterate the most important equation for SCA measurements, SCA is sensitive to two very important physical phenomena when measuring compressibility; the geometric capacitance (C_{geo}) and the thermodynamic density of states ($dN/d\mu$). These are related to the measured capacitance (C_m) by the equation

$$\frac{A}{C_m} = \frac{A}{C_{\text{geo}}} + \frac{1}{e^2 \frac{dN}{d\mu}} \quad (\text{B.1})$$

When the geometric capacitance remains constant, C_m becomes sensitive to the thermodynamic density of states. [4]

Results

So far we have been able to get many results using SCA at 77 K both on and off ZnSe terraces. We do this by first locating an ideal spot on the sample using STM, then switching to SCA to measure the compressibility at the designated location. For measurements taken over bare Bi_2Te_3 , which are shown in Fig. B.6, we see what we believe to be the Dirac cone in the range of 1–1.5 V. This is indicative of the topological surface state strongly existing in the surface of the TI layer, as is expected. The potential at the surface state is less than the potential applied by the tip. This effect is often referred to as the lever arm, which we estimate to be approximately a factor of 10. It should also be noted that in compressibility measurements we will not see a full Dirac cone due to the way the DOS contributes to the capacitance. SCA is sensitive to the DOS only when the DOS term in Eq. B.1 becomes small compared to the geometric capacitance term. This means that we may only be able to see a dip in the compressibility where the Dirac cone DOS is at its smallest.

In Fig. B.7 we show compressibility measurements taken on various ZnSe terraces. While there are hints of Dirac cone behavior and capacitance steps, we have not been able to resolve such features reproducibly. The signal of these features is too small compared to the noise. These results indicate that the TSS is either remaining at the interface between the CI and the TI or that the TSS is moving deeper into the sample and the signal is being screened by other electronic states higher up in the sample surface. We have taken tens of thousands of measurements on these locations, but thus far have been unable to see signs of a floating TSS or a step from the top surface of the CI down to the CI/TI interface.

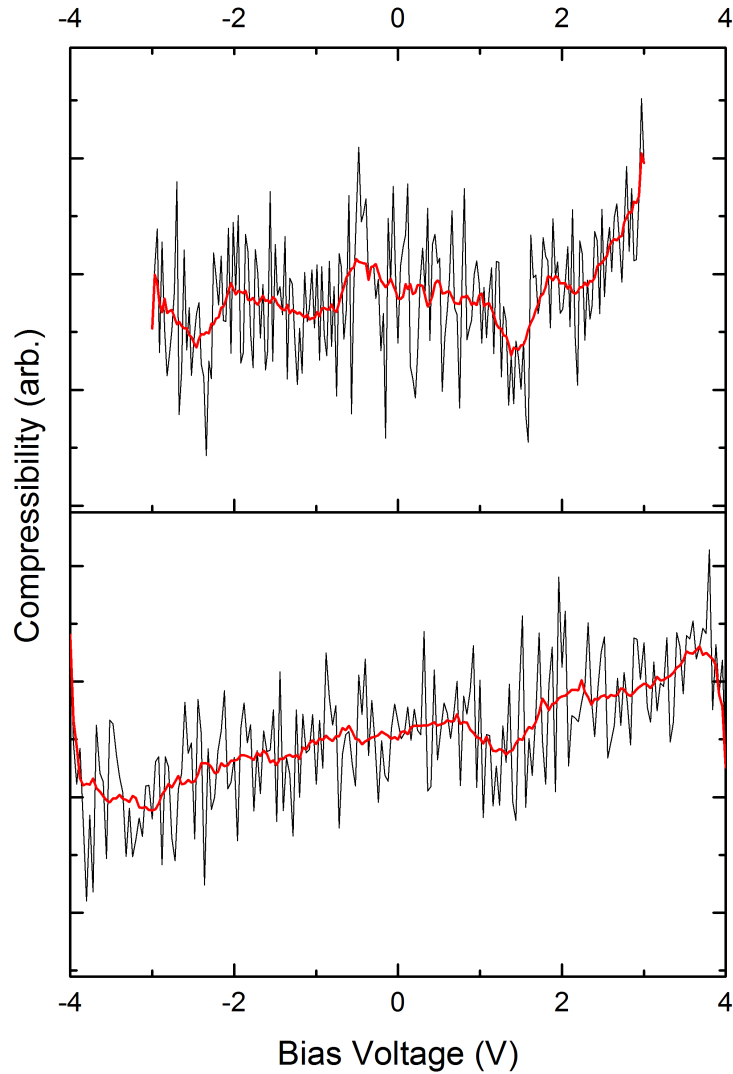


Figure B.6: Compressibility measurement taken over various bare Bi_2Te_3 at 77 K. While there is a notable slope present in these measurements, we see what we believe to be the Dirac cone near 1–1.5 V in these curves. This would be the key signature of the topological surface state and is expected when over a bare TI. All curves shown are averages of thousands of individual curves in order to suppress noise and enhance the signal. The black curves are the raw data while the red curves are the results of smoothing the raw data.

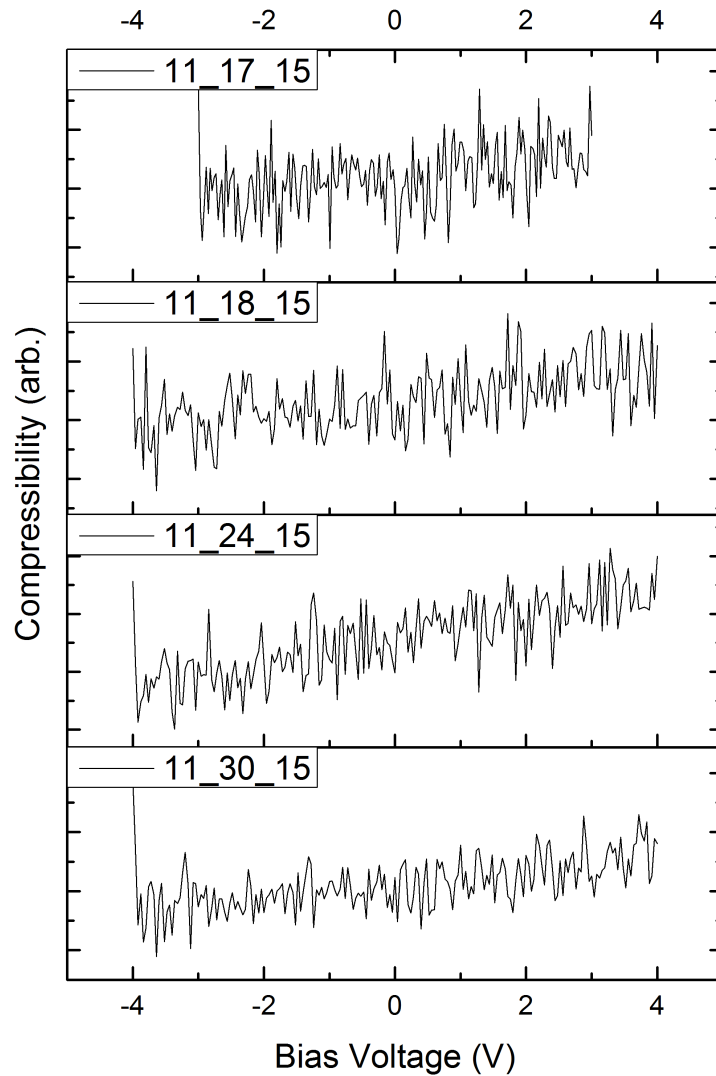


Figure B.7: Compressibility measurement taken over various ZnSe terraces at 77 K. Aside from the apparent slope, there are no notable features in these measurements. The lack of a step in the capacitance or appearance of the Dirac cone indicates that there is no induced topological surface state in this specific interface. All curves shown are averages of thousands of individual curves in order to suppress noise and enhance the signal.

Of course, we also utilized our ability to do STM and STS while using our SCAI circuit. At 77K, STS is very difficult to do due to the poor conductivity of the GaAs substrate. However at room temperature, we were able to acquire some spectroscopy on the bare Bi_2Te_3 .

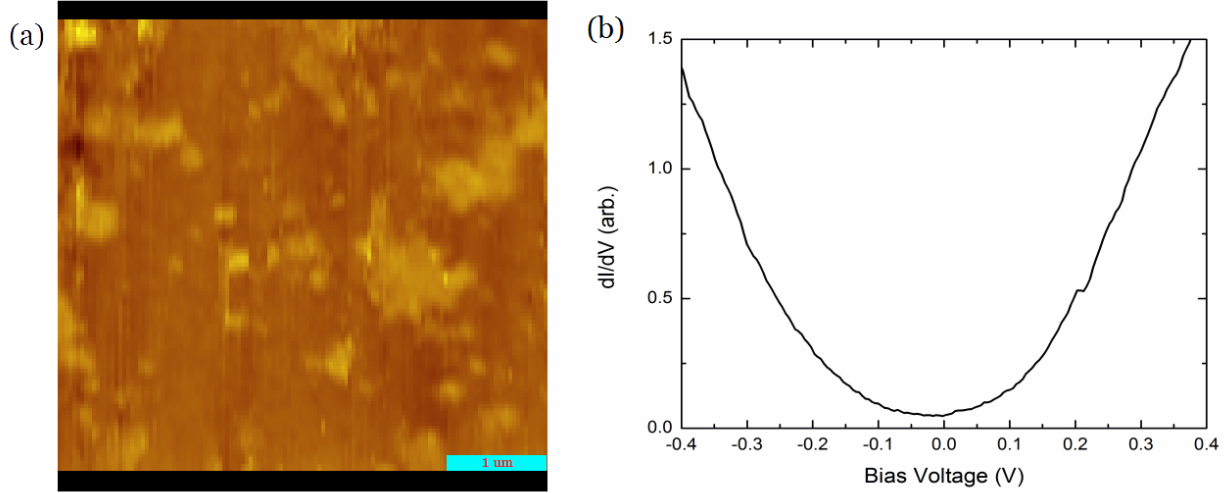


Figure B.8: (a) STM topograph showing the clear different regions of ZnSe and Bi_2Te_3 . (b) STM spectroscopy measurement taken on bare Bi_2Te_3 showing the usual density of states for a Dirac cone at room temperature.

In an even further attempt to characterize what we see in these samples, we also conducted multiple Kelvin probe measurements in order to see if the surface potential of the material had any effect on the compressibility. Please refer to Appendix C for a discussion on the methodology used in our Kelvin probe measurements. Fig. B.9 shows both a Kelvin probe topograph (a) and the corresponding nulling voltage measurements taken in the bright and dark regions (b,c). The resulting V_N in the dark region was -1.035 V and in the light region was -1.132 V. It would have been highly instructive as to the nature of these measurements to take STM spectra in these regions. However, at 77 K, it was impossible to take high quality tunneling spectroscopy due to poor the poor conductance of the samples at low temperatures.

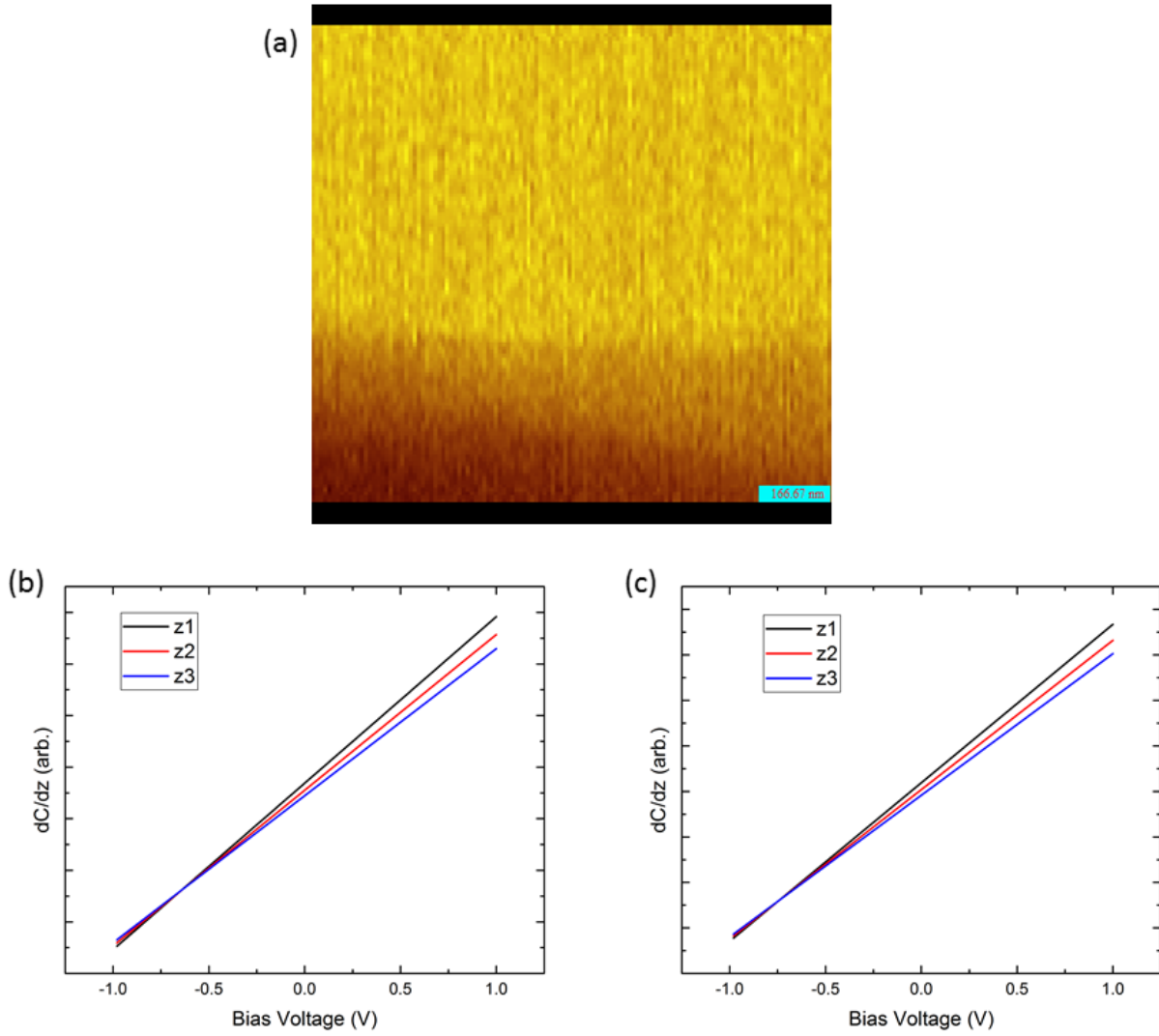


Figure B.9: (a) Kelvin probe topograph showing regions with differing surface potentials. Please refer to Appendix C for a discussion on how the nulling voltage V_N is acquired. (b) Kelvin probe spectrum taken in the dark region at the bottom of (a). The resulting nulling voltage V_N is -1.035 V. (c) Kelvin probe spectrum taken in the bright region of (a). Here, V_N is -1.132 V. While it would have been interesting to take STM spectroscopy in these regions to see if the Dirac cone shifted, it was not possible with this sample due to poor conductivity at 77 K.

Conclusions

We have successfully found a way to prepare the samples and load them into the microscope. There is no doubt that our preparation procedures do exactly what we anticipated due to the fact that we see the expected structure on the surface and are able to measure the Dirac cone using STM. When measuring compressibility, unfortunately we do not resolve any noticeable features or see any steps in capacitance, indicating that the combination of ZnSe and Bi₂Te₃ results in a stationary TSS at the interface between these two materials or at least a step down into the sample which we cannot resolve due to electronic screening effects. However, we believe that we are seeing the Dirac cone states when measuring the compressibility over bare Bi₂Te₃, which implies that we should also see the Dirac cone on the ZnSe terraces if it were indeed floating in this geometry. Due to Ohmic contact issues, we are unable to conduct STS scans at low temperature, but are able to at least do spectroscopy at room temperature, meaning that thermal excitations are needed to reach optimal voltages at the sample surface.

We have set the ground work for further studies of the dual proximity effect of conventional insulator/topological insulator interfaces. While the work presented here is highly preliminary in terms of measuring a tunable location for the topological surface state, we believe that other sample material combinations could lead to the predicted results of the TSS changing location. We observed repeatable cone-like features over bare Bi₂Te₃ which we believe to be the signatures of the Dirac cone, whereas on the ZnSe terraces, we saw no sign of this cone feature as well as no step in the capacitance. This leads us to conclude that the topological surface state remains at the interface between these materials. If the theoretical predictions are later revealed to be correct, the implications of a tunable surface state location could lead to highly refined devices in which the TSS will be protected from disorder.

Appendix C

Kelvin Probe

Stemming from our strong capabilities to measure charge accumulation at the tip apex, our scanning probe systems can also perform a measurement known as Kelvin probe. Kelvin probe is related to our SCAI measurements through the use of the same HEMT circuit mentioned in section 2.2, where the primary difference between the two measurements is that the tip oscillates above the sample instead of the bias voltage oscillating; in this case we use a purely DC bias. Here, the circuit is once again sensitive to the electric field between the tip and the sample, but the measurement is no longer investigating subsurface charges. Kelvin probe is used primarily to measure the surface potential, or work function, of the sample. For ease of discussion, we will call this potential the nulling voltage (V_{Null}) in the following paragraphs.

In Kelvin probe, the measured charge is directly sensitive to the distance between the tip and the sample. This measurement utilizes two primary distances, the mean distance, z_0 , which is the distance of the tip from the sample surface without any oscillatory behavior, and the oscillation distance, Δz , which is the amplitude of the oscillatory distance between the tip and the sample. The lock-in amplifier is used to measure the charge accumulated on the tip, ΔC , as a function of DC bias voltage V . When the tip is closer to the sample, the lock-in amplifier will detect a larger signal due to a higher concentration of electric field terminations on the tip as opposed to when the tip is further away. Thus we can utilize the

well known equation $Q = CV$ to explain the physics of this measurement. In the specific case for this measurement, we have

$$\Delta Q = C(V - V_{Null}) + \Delta Q_0 \quad (\text{C.1})$$

where C is the capacitance between the tip and the sample and ΔQ_0 is some constant "charge" stemming from the scanning probe electronics, which functions as some arbitrary offset of no importance to the measurement. We can further describe the capacitance by utilizing a parallel plate capacitor approximation, which gives us the equation

$$\Delta Q = \frac{A\epsilon_0}{z_0 + \Delta z}(V - V_{Null}) + \Delta Q_0 \quad (\text{C.2})$$

where A is the effective area of the tip and ϵ_0 is the permittivity of free space. The lock-in amplifier is only sensitive to the oscillatory behavior of the measurement, so equation C.2 simplifies down to

$$\Delta Q_{Lock-In} = \frac{A\epsilon_0\Delta z}{z_0^2}(V - V_{Null}) + \Delta Q_0 \quad (\text{C.3})$$

From here, we can clearly see that V_{Null} can be measured by finding the point at which $\Delta Q_{Lock-In} = \Delta Q_0$. However, this is impossible to do using only one curve. The measurement is directly sensitive to the mean distance z_0 , but regardless of what distance exists between the tip and the sample, the point at which $\Delta Q_{Lock-In} = \Delta Q_0$ will occur at the same voltage V . This means that by taking three measurements at differing values of z_0 , we can measure V_{Null} without actually needing to know the value of ΔQ_0 . Where the three separate measurements intersect on a plot of $\Delta Q_{Lock-In}$ vs. V , we will have the value for V_{Null} . A plot demonstrating this can be seen in Fig. C.1.

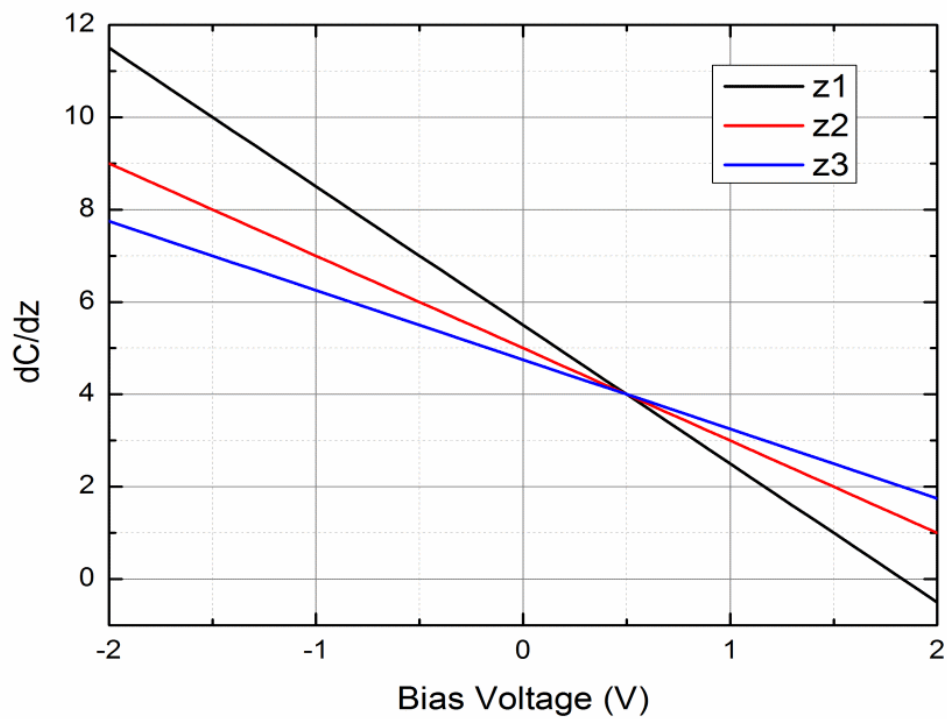


Figure C.1: A plot simulating three dC/dz measurements taken at the same point at different values of z_0 . Here we can see the crossing point occurs at a voltage of .5 V and at a measured value of 4 for dC/dz . This tells us that the nulling voltage would then be .5 V and the arbitrary offset from the measurement electronics has a value of 4.

Of course, during the actual experiment, the HEMT and tip have a separate applied voltage, V_{tip} , which is crucial for tuning the HEMT during the measurement. This adjusts our results by the relation $V = V_{Null} - V_{tip}$. In order to get the V_{Null} , we simply need to add V_{tip} to V extracted from the dC/dz vs. V plot previously mentioned. The value of V_{Tip} is typically around -0.4 V, but it is important to record the exact value when taking the measurements in order to have the best accuracy possible.

BIBLIOGRAPHY

BIBLIOGRAPHY

- [1] J. Bardeen, L. N. Cooper, and J. R. Schrieffer, *Phys Rev.* **108**, 1175 (1957).
- [2] G. Wu, H. Chen, Y. Sun, X. Li, P. Cui, C. Franchini, J. Wang, X.-Q. Chen, and Z. Zhang, *Sci. Rep.* **3**, 1233 (2013).
- [3] K. Besocke, *Surface Science*, **181**, 145 (1987).
- [4] S. H. Tessmer, P. I. Glicofridis, R. C. Ashoori, L. S. Levitov, and M. R. Melloch, *Nature* **395**, 6703 (1998).
- [5] K. Walsh, M. Romanowich, M. Gasseller, I. Kuljanishvili, R. Ashoori, and S. H. Tessmer, *J Vis Exp.* **77**, 50676 (2013).
- [6] M. Z. Hasan and C. L. Kane, *Rev. Mod. Phys.* **82**, 3045 (2010).
- [7] D. Thouless, M. Kohmoto, M. Nightingale, and M. Denny, *Physical Review Letters* **49**, 6,405 (1982).
- [8] R.E. Prange and S.M. Girvin, *The Quantum Hall Effect*. New York, NY:Springer-Verlag, 1990.
- [9] K. v. Klitzing, G. Dorda, and M. Pepper, *Physical Review Letters* **45**, 494 (1980).
- [10] C. Kane and E. Mele, *Physical Review Letters* **95**, 146802 (2005).
- [11] B. A. Bernevig and S.-C. Zhang, *Physical Review Letters* **96**, 106802, (2006).
- [12] C. L. Kane and E. J. Mele, *Physical Review Letters* **95**, 22, 226801 (2005).
- [13] L. Fu, C. Kane, and E. Mele, *Physical Review Letters* **98**, 106803 (2007).
- [14] J. E. Moore and L. Balents, *Physical Review B* **75**, 12, 121306 (2007).
- [15] H.-J. Zhang, C.-X. Liu, X.-L. Qi, X.-Y. Deng, X. Dai, S.-C. Zhang, and Z. Fang, *Physical Review B* **80**, 085307 (2009).

- [16] M. Z. Hasan and C. L. Kane, *Reviews of Modern Physics* **82**, 3045 (2010).
- [17] X.-L. Qi and S.-C. Zhang, *Rev. Mod. Phys.* **83**, 1057 (2011).
- [18] M. Romanowich, M.-S. Lee, D.-Y. Chung, S. D. Mahanti, M. G. Kanatzidis, and S. H. Tessmer, *Phys. Rev. B* **87**, 085310 (2013).
- [19] P. Roushan, J. Seo, C. V. Parker, Y. S. Hor, D. Hsieh, D. Qian, A. Richardella, M. Z. Hasan, R. J. Cava, and A. Yazdani, *Nature* **460**, 1106 (2009).
- [20] M. Tinkham, *Introduction to Superconductivity*. New York: Dover Books, 2004.
- [21] S. Tessmer, Quasiparticle Bound States in Normal Metal/Superconductor Structures Probed by Scanning Tunneling Microscopy. PhD thesis, University of Illinois at Urbana-Champaign, 1995.
- [22] J. Alicea, *Rep. Prog. Phys.* **75**, 076501 (2012).
- [23] L. Fu and C. L. Kane, *Phys. Rev. Lett.* **100**, 096407 (2008).
- [24] N. Read and D. Green, *Phys. Rev. B* **61**, 10267 (2000).
- [25] V.P. Mineev and K. Samokhin, *Introduction to Unconventional Superconductivity*. Amsterdam: Gordon and Breach Science Publishers, 1998.
- [26] P. G. de Gennes, *Superconductivity of Metal and Alloys* (Benjamin, New York, 1966).
- [27] W.J. Gallagher, *Phys. Rev. B* **22**,1233 (1979).
- [28] M. Bianchi, D. Guan, S. Bao, J. Mi, B. Brummerstedt Iversen, P. D.C. King, and P. Hofmann, *Nat. Commun.* **1**, 128 (2010).
- [29] D. Hsieh, D. Qian, L. Wray, Y. Xia, Y. S. Hor, R. J. Cava, and M. Z. Hasan, 2008, *Nature (London)* **452**, 970.
- [30] Y. Xia, D. Qian, D. Hsieh, L. Wray, A. Pal, H. Lin, A. Bansil, D. Grauer, Y. S. Hor, R. J. Cava, and M. Z. Hasan, *Nat. Phys.* **5**, 398 (2009).
- [31] H. Zhang, C.-X. Liu, X.-L. Qi, X. Dai, Z. Fang, and S.-C. Zhang, *Nat. Phys.* **5**, 438 (2009).

- [32] L. Fu and C. L. Kane, Phys. Rev. Lett. **100**, 096407 (2008).
- [33] J. Linder, Y. Tanaka, T. Yokoyama, A. Sudbo, and N. Nagaosa, Phys. Rev. Lett. **104**, 067001 (2010).
- [34] A. C. Potter and P. A. Lee, Phys. Rev. B **83**, 184520 (2011).
- [35] M. Lababidi and E. Zhao, Phys. Rev. B **83**, 184511 (2011).
- [36] P. A. Ioselevich, P. M. Ostrovsky, and M. V. Feigel'man, Phys. Rev. B **86**, 035441 (2012).
- [37] G. Tkachov, Phys. Rev. B **87**, 245422 (2013).
- [38] C. R. Reeg and D. L. Maslov, Phys. Rev. B **92**, 134512 (2015).
- [39] S. Sasaki, M. Kriener, K. Segawa, K. Yada, Y. Tanaka, M. Sato, and Y. Ando, Phys. Rev. Lett. **107**, 217001 (2011).
- [40] M.-X. Wang, C. Liu, J.-P. Xu, F. Yang, L. Miao, M.-Y. Yao, C. L. Gao, C. Shen, X. Ma, X. Chen, Z.-A. Xu, Y. Liu, S.-C. Zhang, D. Qian, J.-F. Jia, Q.-K. Xue, Science **336**, 52 (2012).
- [41] E. Wang, H. Ding, A.V. Fedorov, W. Yao, Z. Li, Y.-F. Lv, K. Zhao, L.-G. Zhang, Z. Xu, J. Schneeloch, R. Zhong, S.-H. Ji, L. Wang, K. He, X. Ma, G. Gu, H. Yao, Q.-K. Xue, X. Chen, and S. Zhou, Nat. Phys. **9**, 621 (2013).
- [42] G. Koren, T. Kirzhner, Y. Kalcheim, and O. Millo, Europhys. Lett. **103**, 67010 (2013).
- [43] J.-P. Xu, C. Liu, M.-X. Wang, J. Ge, Z.-L. Liu, X. Yang, Y. Chen, Y. Liu, Z.-A. Xu, C.-L. Gao, D. Qian, F.-C. Zhang, and J.-F. Jia, Phys. Rev. Lett. **112**, 217001 (2014).
- [44] B. Sacepe, J. B. Oostinga, J. Li, A. Ubaldini, N. J. G. Couto, E. Giannini, and A. F. Morpurgo, Nat. Commun. **2**, 575 (2011).
- [45] M. Veldhorst, M. Snelder, M. Hoek, T. Gang, V. K. Guduru, X. L. Wang, U. Zeitler, W. G. Van der wiel, A. A. Golubov, H. Hilgenkamp, and A. Bririkman, Nat. Mater. **11**, 417 (2012).
- [46] F. M. Qu, F. Yang, J. Shen, Y. Ding, J. Chen, Z. Q. Ji, G. G. Liu, J. Fan, X. N. Jing, C. L. Yang, and L. Lu, Sci. Rep. **2**, 339 (2012).

- [47] J. R. Williams, A. J. Bestwick, P. Gallagher, Seung Sae Hong, Y. Cui, Andrew S. Bleich, J. G. Analytis, I. R. Fisher, and D. Goldhaber-Gordon, *Phys. Rev. Lett.* **109**, 056803 (2012).
- [48] S. Cho, B. Dellabetta, A. Yang, J. Schneeloch, Z. Xu, T. Valla, G. Gu, M. J. Gilbert, and N. Mason, *Nat. Commun.* **4**, 1689 (2013).
- [49] C. Kurter, A. D. K. Finck, P. Ghaemi, Y. S. Hor, and D. J. Van Harlingen, *Phys. Rev. B* **90**, 014501 (2014).
- [50] C. Kurter, A. D. K. Finck, Y. S. Hor, D. J. Van Harlingen, *Nat. Commun.* **6**, 7130 (2015).
- [51] I. Sochnikov, L. Maier, C. A. Watson, J. R. Kirtley, C. Gould, G. Tkachov, E. M. Hankiewicz, C. Brüne, H. Buhmann, L. W. Molenkamp, and K. A. Moler, *Phys. Rev. Lett.* **114**, 066801 (2015).
- [52] M. P. Stehno, V. Orlyanchik, C. D. Nugroho, P. Ghaemi, M. Brahlek, N. Koirala, S. Oh, and D. J. Van Harlingen, *Phys. Rev. B* **93**, 035307 (2016)
- [53] D. Zhang, J. Wang, A. M. DaSilva, J. S. Lee, H. R. Gutierrez, M. H. W. Chan, J. Jain, and N. Samarth, *Phys. Rev. B* **84**, 165120 (2011).
- [54] P. Zareapour, A. Hayat, S. Y. Zhao, M. Kreshchuk, A. Jain, D. C. Kwok, N. Lee, S. W. Cheong, Z. J. Xu, A. Yang, G. D. Gu, S. Jia, R. J. Cave, and K. S. Burch, *Nat. Commun.* **3**, 1056 (2012).
- [55] A.D.K. Finck, C. Kurter, Y.S. Hor, D.J. Van Harlingen, *Phys. Rev. X* **4**, 041022 (2014).
- [56] A.D.K. Finck, C. Kurter, E.D. Huemiller, Y.S. Hor, D.J. Van Harlingen, preprint arXiv:1503.06898.
- [57] L. A. Wray, S.-Y. Xu, Y. Xia, Y. S. Hor, D. Qian, A. V. Fedorov, H. Lin, A. Bansil, R. J. Cava, and M. Zahid Hasan, *Nat. Phys.* **6**, 855 (2010).
- [58] Y. S. Hor, A. J. Williams, J. G. Checkelsky, P. Roushan, J. Seo, Q. Xu, H. W. Zandbergen, A. Yazdani, N. P. Ong, and R. J. Cava, *Phys. Rev. Lett.* **104**, 057001 (2010).
- [59] M. V. Feigel'man, M. A. Skvortsov, K. S. Tikhonov, *JETP Lett.* **88**, 862 (2008).
- [60] S. Eley, S. Gopalakrishnan, P. M. Goldbart, N. Mason, *Nat. Phys.* **8**, 59 (2012).

- [61] P. G. Gennes, in *Superconductivity Of Metals And Alloys*, (Westview Press, 1999).
- [62] G. Deutscher and P. G. Gennes, in *Superconductivity*, edited by R. D. Parks (Dekker, NY, 1969).
- [63] T. Wolfram, *Phys. Rev.* **170**, 481 (1968).
- [64] J. G. Adler and S. C. Ng, *Can. J. of Phys.* **43**, 594 (1965).
- [65] N. Moussy, H. Courtois and B. Pannetier, *Europhys. Lett.*, **55** (6), 861 (2001).
- [66] A. Levchenko, *Phys. Rev. B* **77**, 180503(R) (2008).
- [67] I. M. Dayton, N. Sedlmayr, V. Ramirez, T. Chasapis, R. Loloee, M. Kanatzidis, A. Levchenko, and S. H. Tessmer, *Phys. Rev. B* **93**, 220506(R) (2016).
- [68] H. Beidenkopf, P. Roushan, J. Seo, L. Gorman, I. Drozdov, Y. S. Hor, R. J. Cava, and A. Yazdani, *Nature Physics* **7**, 939 (2011).